UNIVERSITY OF OKLAHOMA

GRADUATE COLLEGE

IMPROVEMENTS IN SCANNING INFRARED THERMOGRAPHY

A DISSERTATION

SUBMITTED TO THE GRADUATE FACULTY

in partial fulfillment of the requirements for the

Degree of

DOCTOR OF PHILOSOPHY

By

CHRISTOPHER RYAN DALTON
Norman, Oklahoma
2010

IMPROVEMENTS IN SCANNING INFRARED THERMOGRAPHY

A DISSERTATION APPROVED FOR THE
SCHOOL OF AEROSPACE AND MECHANICAL ENGINEERING

BY

_____
Feng C. Lai

_____
M. Cengiz Altan

_____
S.R. Gollahalli

_____
Wilson Merchan-Merchan

_____
Dimitrios Papavassiliou

ACKNOWLEDGEMENTS

There are numerous people I wish to thank for their assistance during my dissertation work. First and foremost, I wish to thank my advisor Dr. Feng C. Lai, for his advice and support during my graduate career. In addition to being my dissertation advisor, Dr. Lai served as both a committee member on my Master's thesis, my advisor for my Honor's thesis, and he was one of my favorite engineering instructors. Over the last seven years, Dr. Lai has been a constant supporter of me and my work, as well as a great advisor. Most importantly, he agreed to take over as committee chair and allowed me to complete my current project even though it wasn't in his research area. I am incredibly indebted to him and very thankful for all he has done for my academic career.

I also wish to thank the rest of my committee members, Dr. M. Cengiz Altan, Dr. S.R. Gollahalli, Dr. Wilson Merchan-Merchan, and Dr. Dimitrios Papavassiliou. They have all contributed to the success of this project and helped me to become the best student researcher I could be. I would also like to thank my former advisor Dr. Brandon Olson. We began this project together 6 years ago, and while he has moved on to another position, I still feel his impact while working on this project.

I would also like to take this opportunity to thank the entire faculty and staff of the School of Aerospace and Mechanical Engineering. Over the last ten years there have been few times where I couldn't find assistance with a project, paperwork, or any other issue I was having. The faculty have taught me a great deal over that period of time (after all, I have now finished three degrees here), and they have always been willing to not only improve my knowledge base, but to also prepare me for the world of academia. The staff of the school has also been incredibly helpful, in particular with helping me

with my teaching responsibilities and all the paperwork that is associated. When I do eventually move on to another institution, it will be difficult to match the kindness and assistance that I have received while at OU.

There are many students that have also contributed to this project over the last few years. While there are too many to mention by name, I would like to particularly address my two undergraduate assistants of the last two years: Mr. Gerardo "JR" Conanan and Mr. Mitchell Greer. Both of them proved to be mature beyond their years as they tackled aspects of a very challenging project. They were always prepared to handle any responsibility I delegated to them, and they both produced work that has been incorporated into this dissertation. I would also like to thank Mr. Orhan Ozcelik and Dr. Levent Aktas, who assisted in producing some of the samples that were tested for this dissertation.

My gratitude also goes to Mr. Billy Mays and Mr. Greg Williams, the supervisors of the OU AME machine shop. They were integral in helping build portions of the system that is currently being used, and without their assistance the system would not be what it is today. They have also been willing to supply me with materials and fabrication expertise whenever they were needed.

Finally, I would like to thank my family and friends for their constant support. Their unceasing encouragement over the last 3 years gave me the confidence to believe I could finish this dissertation and do the other things I have achieved during my doctoral career. My last acknowledgement is to pass this message along to all of them:

Yes, I'm done with school now – you can stop asking.

TABLE OF CONTENTS

LIST OF TABLES

LIST OF FIGURES

ABSTRACT

Non-destructive evaluation techniques are important for many industries. Scanning infrared thermography systems have the potential to analyze materials and parts, quickly, accurately, and at a reduced cost compared to other systems. Scanning infrared thermography uses Fourier's law of conductive heat transfer to detect both material and geometric anomalies in a particular sample. The current system has been developed to create an easy to operate physical system and an interface utilizing commercial software packages. New hardware components have been designed to work in concert with specially developed analytical models to treat surfaces with changing emissivity and uniformly finished surfaces like those used in traditional infrared scanning systems.

A newly developed LabView program has simplified the data collection process by combining all data analysis into a single program. The program uses radiative heat transfer theory and incorporates temperature data from several sources to calculate the true surface temperature of the sample which is crucial for defect detection. An improved camera shroud has also improved the ability to handle variable emissivity surfaces.

Several computational models have been developed to determine the defect detection resolution of a variety of defects using this system. Results obtained from the models showed that the system is capable of detecting crack defects as small as 0.5 cm in lateral length. Void defects and other 3-dimensional defects were shown to be marginally detectable as well. Radiative heat transfer analysis was performed on the camera shroud

and it was determined that the camera shroud has little effect on the radiation received by the camera.

The system has been successful at detecting defects on coated surfaces where cracks were oriented parallel to the heating element and at sub-optimal angles. In addition, new experimentation has shown the new camera shroud and LabView program to be successful at removing reflected radiation from variable emissivity, diffuse surfaces. However, the system has only been marginally successful at removing artifacts of reflected radiation from thermographic images of surfaces that show a high degree of specularity, making temperature correction and crack detection difficult.

The system has also been used to test non-metallic samples to determine whether it would be a viable choice for applications in this area. A set of composite samples was tested to verify whether defects in this type of material could be successfully detected. Testing showed that sub-surface changes in thermal-conductivity could be detected using the current system. However, due to the extremely low thermal conductivities of some of the materials, testing proved to be much more time consuming and less successful than it is with metal samples. For thin sheets, delaminations and other sub-surface defects may prove difficult to detect.

CHAPTER ONE

INTRODUCTION

1.1 Non-Destructive Evaluation

Non-Destructive Evaluation (NDE) is a method where materials or parts can be evaluated without damaging the part such that it can be reused [1]. This saves time and money by allowing data to be collected on a specific device, part or material instead of using general data from published references. In addition, the first signs of failures can be seen before harmful damage is made, thus avoiding the dangerous consequences a failure can bring. NDE is used frequently in situations where systems undergo cyclic or repeated stresses. These stresses are below the ultimate failure limits, but over time these smaller stresses can eventually build to fracture. Therefore, it is imperative to scan systems, parts and materials for these early defects that can ultimately lead to costly failures.

1.1.1 Scanning Infrared Thermography

Scanning infrared thermography is a relatively new alternative in the world of NDE. As seen in Fig. 1.1, the systems primarily consist of a heat source of some type that creates a heat flux in the material or sample being tested, and an infrared camera or sensor focused on the sample. Infrared scanning systems are not new; they have been used in numerous applications in biology, astronomy, and even the military. Even in basic infrared evaluation, surface temperature is the valued information that is used to infer characteristics of the given item. However, infrared scanning systems can add a new dimension to their capabilities when principles of heat transfer are considered, particularly Fourier's law of heat conduction. Fourier's law states that the amount of heat

transfer through a material is determined by three factors: temperature gradient, cross-sectional area, and thermal conductivity. Therefore, if the amount of heat transfer is held constant, changes in the thermal conductivity or cross-sectional area directly affect the temperature gradient within the material. As a heat flux passes through a pure substance, it will create a smooth temperature gradient based on the material's thermal conductivity and cross-sectional area. However, if either of the properties varies through a particular part or piece, the temperature gradient will veer from the expected distribution and display anomalies. While these anomalies might be difficult to detect using physical contact temperature measurement devices, they become very easy to see when using an infrared scanning device [2, 3]. From this point, one only has to identify the locations of the temperature anomalies and perform closer examinations to determine the cause for the shift.

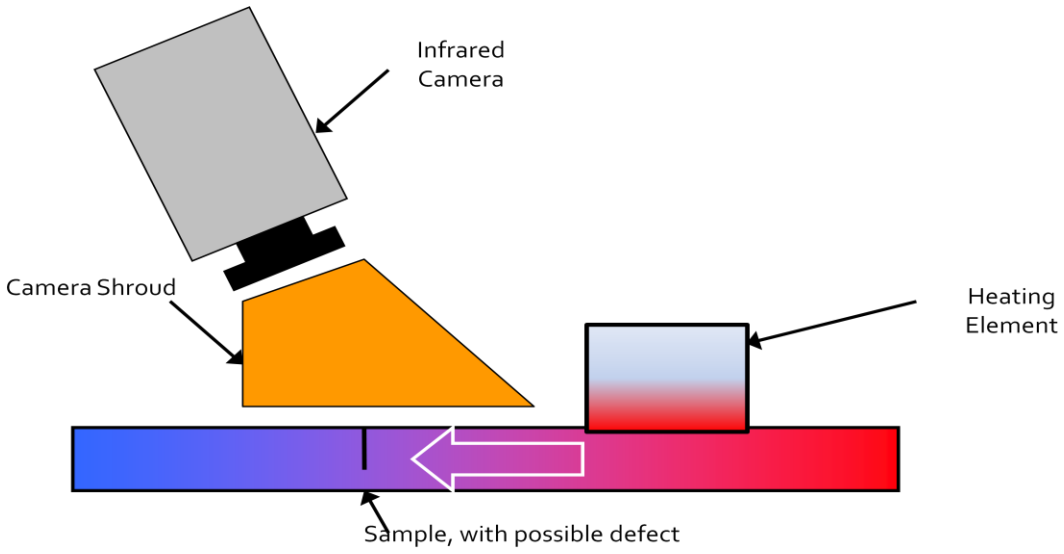

Fig. 1.1 Schematic of Infrared Scanning System.

There are several advantages to scanning infrared thermography. Compared to other types of non-destructive evaluation, scanning infrared thermography is considerably quicker in operation as well as fairly portable. Most systems are also non-contact, meaning that no part of the equipment comes into contact with the materials being tested, which provides no opportunity for the samples to be inadvertently damaged. In terms of scanning large areas, very few systems can match its potential ease and speed. Additionally, infrared systems continue to drop in price and complexity as IR technology improves. Finally, the principles of heat transfer that guide scanning infrared thermography in its analysis are very well known and understood, and are thus more inclined toward improvement.

1.1.2 Alternative Methods of NDE

There are numerous non-destructive methods currently available for detecting defects in parts or materials, such as X-ray imaging, eddy current testing, and acoustic methods that are available in both ultrasonic and subsonic frequencies. One of the most popular methods is eddy current testing (shown in Fig. 1.2), where alternating current is passed through an electric coil to generate a magnetic field near the surface of the material. This magnetic field generates eddy currents within the material that penetrate and eventually weaken. The eddy currents within the material create a secondary magnetic field that opposes the original, and this can be detected from the electric test coil. Cracks, or other defects, block the flow of the eddy currents, which in turn reduces the secondary field, and is thus detected by the coil.

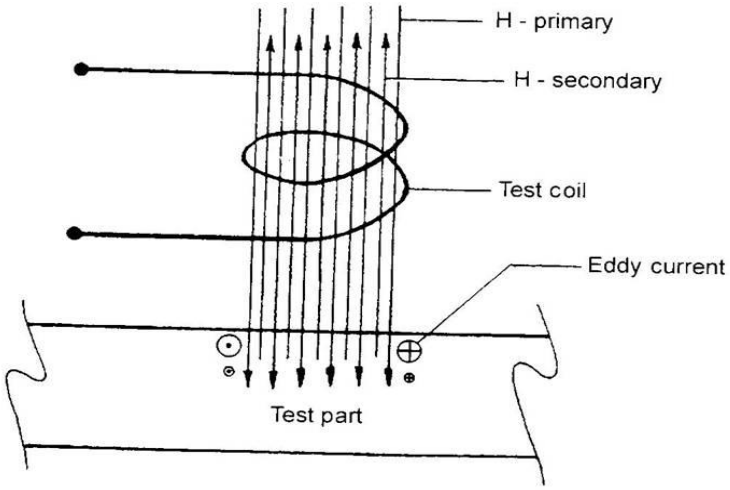

Fig. 1.2 Schematic of Eddy Current System [1].

Another popular method used for non-destructive evaluation is ultrasonic testing. As shown in Fig. 1.3, this method uses high frequency sound waves to penetrate the material, and if anomalies are present, the resulting echoes are changed and can be recorded. One drawback for many ultrasonic systems is that there must be a coupling agent (water or grease as examples) to counter acoustic impedance, although newer systems have been able to avoid this necessity. Also still used in some cases is traditional X-Ray radiography where X-Rays penetrate the material and the remaining signal is captured on a film. While all of these methods are quite good at detection in various environments, with resolutions on par with scanning infrared thermography, many of them are quite expensive as well as difficult to operate. Both ultrasonic and magnetic eddy current testing require a very skilled technician to properly condition and correctly interpret the signal. Also restrictive is the size of many of these devices, some of which require unusual amounts of space for the associated hardware.

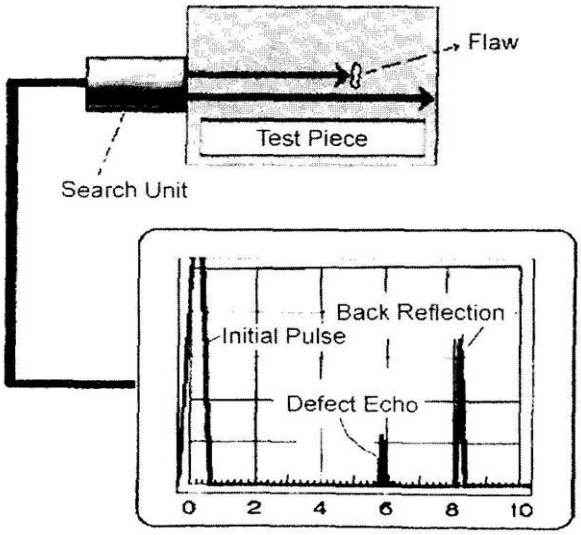

Fig. 1.3 Schematic of Ultrasonic Testing System [1].

Additional thermography methods are also available besides scanning, the most popular of which is flash thermography, which has seen widespread scientific and commercial use. This method involves short bursts, or "flashes" of infrared radiation aimed at a surface, and then taking time-lapse images to record the effects. The energy received by the sample passes through the depth of the material, and if anomalies are encountered, an echo returns to the surface, which can be read by the infrared camera. Flash thermography has been proved advantageous in situations where the desired testing is to search for defects well below the surface of thicker materials. However, it has been shown that scanning thermography is more accurate when analyzing flaws near or at the surface of materials [2]. In addition, due to the nature of flash thermography, defects oriented normal to the surface being analyzed have the potential to be undetected.

While each of these techniques has merit and is successful in certain cases, there are situations where the best technique is still visual hand inspection, where trained personnel carefully scan parts and materials for potential issues. Unsurprisingly, this can

take an extraordinary amount of time, and so there are searches underway to find a system or method that allows for high defect resolution as well as faster analysis. Infrared scanning is one promising method that could potentially meet these requirements.

1.2 Literature Review

1.2.1 Early Infrared Sensing

The use of infrared radiation as a means of temperature measurement has been available for more than 100 years, even though infrared radiation itself was still a somewhat mystical phenomenon in the earliest times. In the beginning, the technique was successful at qualitatively detecting a change in temperature, but continued research and experimentation eventually led to the development of the first commercially available infrared cameras in the 1960s when they were used primarily for passive thermographic techniques, such as monitoring the operating temperature of a piece of machinery [3].

Infrared cameras (as well as other infrared sensors) are able to operate because of the well known relationship between radiation and temperature known as the Stefan-Boltzmann Law [4],

$$M_b = \sigma T^4 \tag{1.1}$$

where the total radiation of a blackbody (M_b) is directly related to the temperature (T) of the surface and σ is the Stefan-Boltzmann constant. Equation (1.2) illustrates how the emissivity (ε) can reduce the amount of radiative energy emitted (J) when the reflected radiation is ignored [4],

$$J = \varepsilon \sigma T^4 \tag{1.2}$$

1.2.2 Active Infrared Thermography

The use of active infrared thermography in non-destructive testing, where external heat is introduced to the sample or item being captured, has only been well documented in the last 10 or 20 years. Advancements in digital photography and sensor development have made infrared cameras much simpler and easier to use, as well as more accurate and responsive. Methods like flash thermography and scanning thermography have employed infrared cameras with excellent results.

Active thermography techniques for non-destructive evaluation use Fourier's law of heat conduction as the principle of operation [4],

$$Q = k_x A_x \frac{\partial T}{\partial x} + k_y A_y \frac{\partial T}{\partial y} \tag{1.3}$$

The heat conducted through a given material is determined by the material's ability to conduct heat (k), the cross-sectional area perpendicular to the direction of transfer (A) and the temperature gradient across the material. As shown in Fig. 1.4, if the amount of heat transfer is kept constant, any deviation in the temperature gradient in the material is caused by a material anomaly, either in geometry or composition.

Scanning infrared thermography is the use of an infrared camera to spot anomalies in a material or part through the use of a spatially controlled heat source. The heat source is scanned across the material to be studied, with the infrared camera recording the corresponding surface temperature. With prior knowledge of the heat

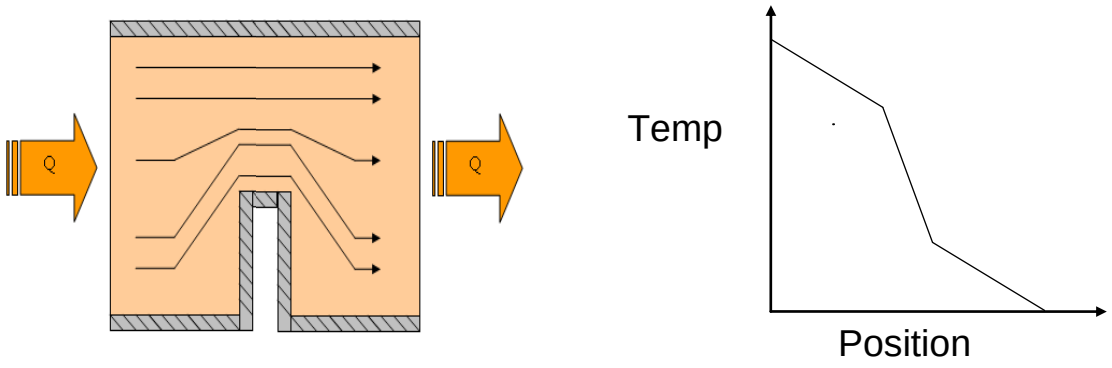

Fig. 1.4 Demonstration of Temperature Variation due to Cross-sectional Area Reduction.

source's effects on a particular material, a trained person can identify unexpected changes in the heat signature due to local changes in heat transfer. This method can be altered to suit various defect situations. Scanning infrared thermography has proven successful at not only detecting lateral defects at or near the surface, but also deeper subsurface anomalies in thicker materials [5].

The earliest studies, using this technique, appeared in the early 90's and were generally intended as a proof-of-concept which yielded qualitative results in the form of images [5]. The bulk of the research was devoted to handling the large amount of data produced by the camera, and processing it to produce meaningful results [6].

One of the largest research groups using this technology are located at NASA's Langley Research Center and is led by K.E. Cramer. They have produced nearly a dozen reports over the last 15 years detailing the success of IR scanning in various environments. Using a quartz lamp heat source in series with the infrared camera, they produced thermographic images of a variety of defect situations, including cracks, delaminations, corrosion and others. Cramer et al. have proven successful in using this method for detecting fatigue cracks in thin metal sheeting [7], exposing disbonds and

corrosion in aircraft lap joints [8], as well as material loss in boiler water-wall tubing [9] in addition to other situations [10, 11].

1.2.3 Composite Materials Testing

Due to the explosion in composites research and applications, it has become important to the NDE community to evaluate traditional NDE techniques, including infrared thermography technique, as an adequate method for defect detection for these new materials. While composites have proven to have many advantages in a wide variety of applications, they have also proven more susceptible to many defects than traditional metals, such as defects produced by fasteners, rapid delaminations during use, and production defects such as voids and poor laminations. Therefore, traditional NDE techniques must be reconfigured to properly analyze for not only material differences, but also the potential for different modes of failure.

At this point, flash thermography has been used to analyze a sampling of common composites at use today. Testing has been focused on carbon fiber reinforced composites and has shown to be successful at detecting a variety of damage modes due to improperly installed fasteners and delaminations due to low-velocity impacts [12]. In an application proving both its portability and its energy efficiency, a passive thermography system was used successfully in Earth orbit to analyze portions of the Space Shuttle's thermal protection system (TPS), which is composed of reinforced carbon-carbon (RCC) panels [13].

1.2.4 Areas for Improvement

While some attempts have been made to apply this technology to real-world industrial applications, there are still practical difficulties that need to be resolved. While

there have been tremendous strides in creating a simple interface to analyze data [14], a system that seamlessly combines data acquisition and image processing with an easy-to-use real-time interface must be developed. This interface should provide users a reasonable array of options in terms of data collection, image processing, image display, and data storage. Another major impediment to practical use of this technique is the treatment of low and variable emissivity surfaces. Since IR cameras measure incident radiation, they inherently interpret changes in radiant energy as changes in temperature. Equation (1.2) illustrates that the amount of radiation emitted from a surface is directly dependent on the surface's emissivity; thus, changes in surface emissivity are incorrectly interpreted as temperature changes by the IR camera. Prior knowledge of surface emissivity is, therefore, a prerequisite of accurate surface temperature measurement.

1.2.5 Noise Analysis

Preliminary research has been conducted in an effort to analyze the type (or distribution) of noise that is present in thermal images [15], and to determine whether the magnitude of the noise within the thermographic images was affected by the average temperature of the surface. If the amount of noise increases or decreases with change in temperature, additional programming would be required to ascertain surface temperatures before filtering occurred. Images of surfaces heated to a range of temperatures were analyzed to determine the scatter of the noise in each image. This was accomplished by extracting a single line of data within the image and examining how it fluctuated about a running average. Results of this experiment indicate that the local variation of temperature does not change dramatically with increases in average surface temperature. The local variation in temperature was observed to follow a Gaussian distribution with an

absolute magnitude that was less than 0.5 °C regardless of the surface temperature. Figure 1.5 shows an example of two histograms of noise variation from the average temperature, where Fig. 1.5(a) shows the variation of noise at 25 °C, and Fig. 1.5(b) shows the variation at 50 °C. While there is a slight difference in the shape of the error distributions, this is to be expected given the relative size of the sample population. Given this insensitivity of the noise to the temperature magnitude, the noise reduction software can be set to neglect the effects of the average temperature when the smoothing and noise reduction filtering is executed. In addition to the simplified error filtering, these results imply that larger temperature gradients can be used for crack detection without any cost in terms of additional noise.

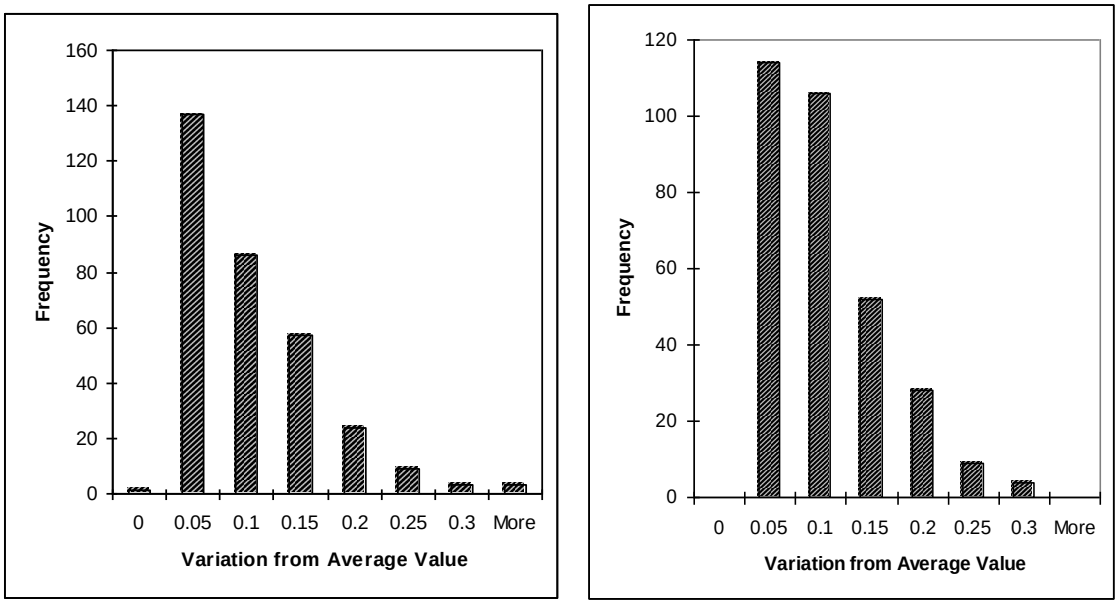

(a) (b)

Fig. 1.5 Histograms of Thermal Noise [15]: (a) from the average temperature of 25 °C, (b) from the average temperature value of 50 °C.

1.3 Prior System Development

The previous incarnation of this system was developed in the attempt to address many of the issues presented in Section 1.2.4. The system included all the major elements listed in Fig. 1.1 with some minor alterations [16].

1.3.1 Experimental Apparatus and Procedure

In the previous version of this system, the heating element was a commercial halogen light bulb with a metal reflector, which can be seen in Fig. 1.6. Surface heating was due to the radiative heat emitted by the light source, and the intensity of the light was controlled by a commercial dimmer switch. As shown in Fig. 1.7, the camera shroud was constructed out of aluminum sheet and heated by attaching resistance heating wire and embedding the wire in epoxy. The camera, shroud, and heating element were mounted on a shelf could be shifted laterally to move to different sections of the sample being studied. The procedure for data collection was similar to the method described later in this report, however all data analysis was done separately after data collection instead of during testing. Analysis was performed using a set of Matlab graphical user interfaces.

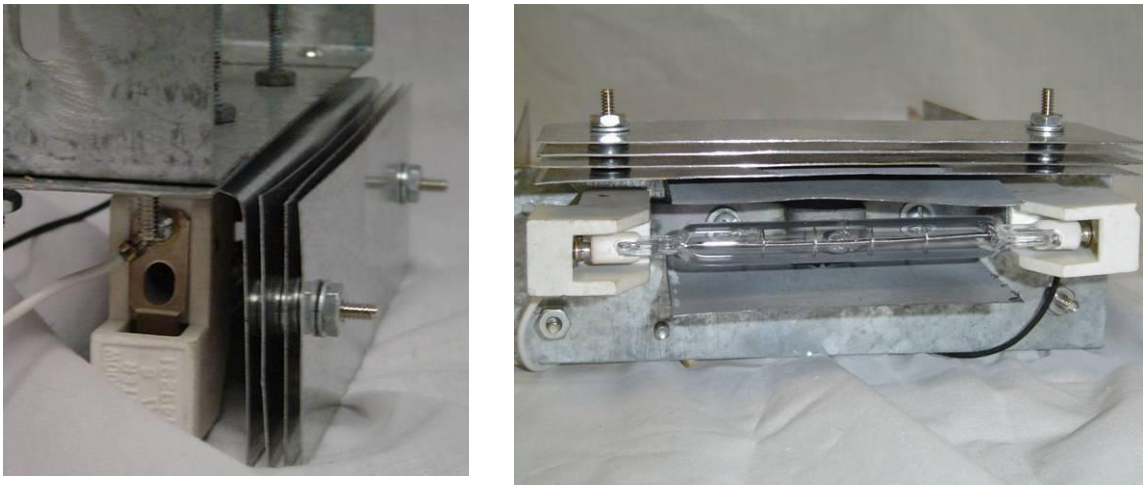

(a) (b)

Fig. 1.6 Heating Element and Radiation Shielding, (a) Side View, (b) Bottom View.

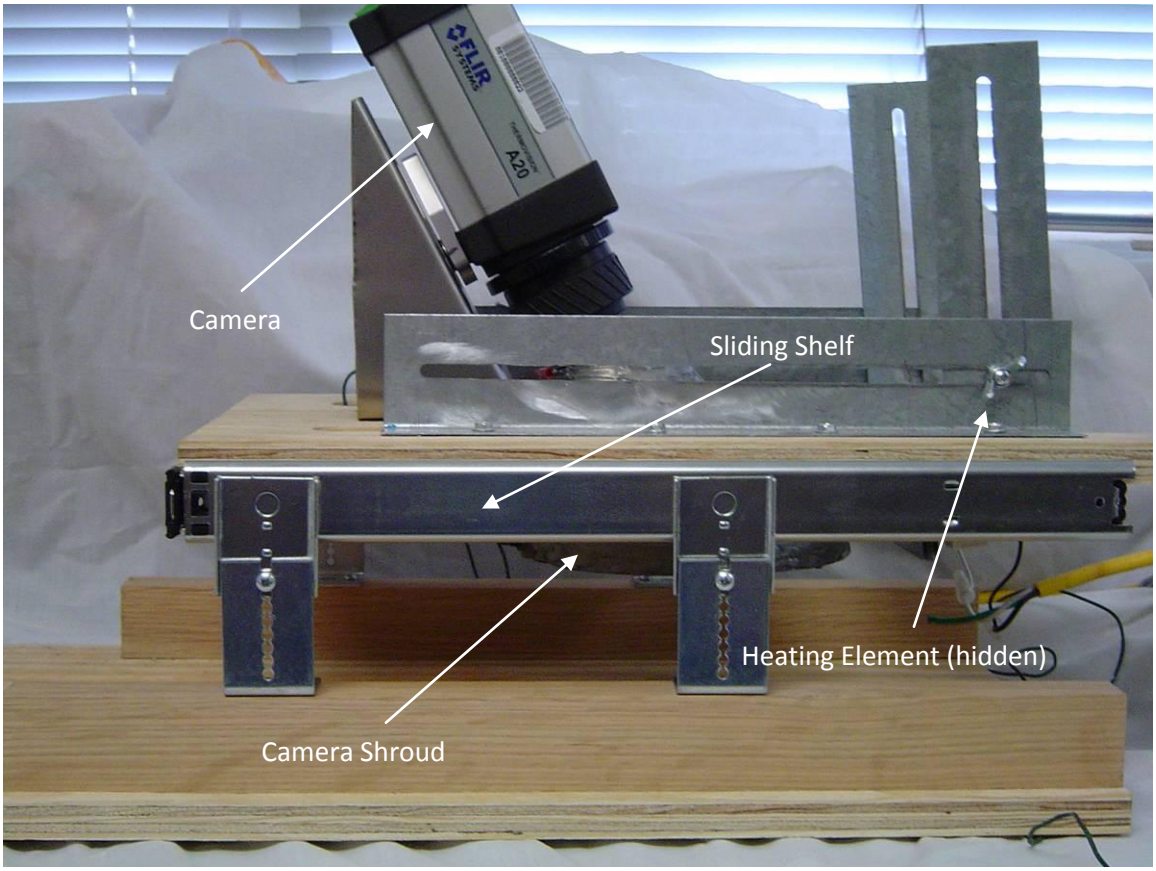

Fig. 1.7 Scanning Infrared Thermographic System (Early Version).

1.3.2 Results

The previous incarnation of the system proved extremely successful at locating crack defects in thin sheet metals with a uniform high emissivity. However, when the system was used to analyze materials with variable emissivity, the system had difficulties differentiating between material defects and emissivity anomalies. It was shown that the camera shroud was unable to maintain a uniform temperature within an acceptable range for our analysis and that most likely led to flaws in our analysis technique. In addition, it proved difficult to isolate the halogen bulb heating element so that it only emitted heat to the sample surface, not the camera shroud. While the Matlab analysis programs developed proved successful in analysis, transferring data from one program to another was determined to be time-consuming and inefficient.

1.4 Objectives of the Present Study

The newest version of the system presented within has proven successful at locating crack defects in sheet metal with a uniform high emissivity. In addition, the system has also been developed with a much simpler user interface that will allow for varying levels of analysis complexity that can be contoured to the changing skill level of the user. Another innovation is its ability to scan materials and parts regardless of surface coating, as well as the ability to analyze parts or materials with low or variable emissivity [17]. With these promising results already presented, the scope of the present study can be focused in certain areas to improve the versatility, accuracy, and ease of use of the system. Since infrared camera systems continue to become less expensive than other scanning options, it is our hope that this can be developed into a simple, quick, and above

all inexpensive method to carry out non-destructive evaluation and assist in preventative maintenance.

Therefore, the objectives of this study can be summarized as follows:

1. To improve the current iteration of the infrared scanning system, with accompanying software, that allows for quick, simple analysis of thermal images.
2. To expand the capability of the system to handle composite materials and successfully locate a variety of defects within them.
3. To improve the ability of the system to handle surfaces with variable or low emissivity through the use of radiative heat transfer analysis.
4. To evaluate a series of coatings based on their ease of application and removal, cost, and emissivity improvement.
5. To develop a series of computer models to verify the results of our testing.
6. To develop the initial programming and theory required to automate the system.

CHAPTER TWO

HEAT TRANSFER THEORY

Scanning infrared thermography systems use both conductive and radiative heat transfer modes to detect defects in materials. Although convection is present in the system, it is assumed that the amount of heat lost due to convection is negligible since the system is under natural convection and the temperature difference between the sample and the ambient air is relatively small. This can be demonstrated using the Biot number (Bi), which is the ratio of convective heat transfer to conductive heat transfer.

2.1 Conductive Heat Transfer

For this system, the materials under testing are typically thin sheets approximately 10-50 cm in width and length with a relatively small thickness (typically no more than 5% of the width or length). Because the thickness of the material is typically so small, it is assumed that the temperature gradient through the thickness is uniform and any analysis involving that direction can be eliminated. Figure 2.1 shows a schematic of a typical sample. One edge of the sample ($x = 0$) is raised to a fixed elevated temperature and heat is allowed to conduct through the rest of the material. The right boundary is considered a convective boundary with ambient temperature (T_∞) and convective heat transfer coefficient (h) specified. The sample is initially at a constant temperature (T_i) that is lower than the temperature at the left boundary. While some heat leaves the sample through convection, it is a relatively small amount compared to the amount of heat provided through conduction and eventually the entire sample reaches the elevated temperature of the edge of the sample.

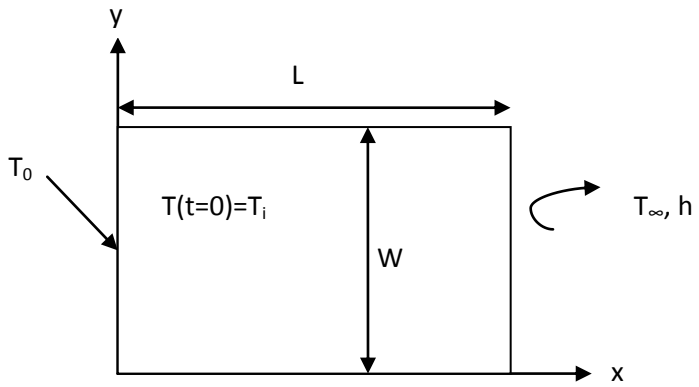

Fig 2.1 Schematic of a typical sample.

2.1.1 One-Dimensional Stationary Transient Conduction

Before discussing the effects of motion on the system's capability in detecting defects, one needs first to understand the important implications from the stationary conduction analysis. The heat flux is initiated along the entire width of the sample, so it is expected that in a uniform material the temperature distribution will be constant in the y-direction. It is therefore assumed that heat transfer will take place only in one dimension (x-position) and time dependence for a uniform sample with no defects present. Accordingly, the boundary conditions are also limited to only x-position and time dependence. With these assumptions, one can predict the temperature distribution along the x-axis of the sample by using a one-dimensional transient conduction equation,

$$\frac{\partial^2 T(x,t)}{\partial x^2} = \frac{1}{\alpha}\frac{\partial T(x,t)}{\partial t}. \tag{2.1}$$

Temperature (T) is a function of distance (x), time (t), and the thermal diffusivity of the material (α). First, it is assumed that the solution consists of two parts: a steady-state solution (T_s) only dependent on distance, and a transient solution (T_t) dependent on both distance and time. This alters the governing equation thusly,

$$\frac{d^2T_s}{dx^2}+\frac{\partial^2T_t}{\partial x^2}=\frac{1}{\alpha}\frac{\partial T_t}{\partial T}. \tag{2.2}$$

This equation can be split into two solvable differential equations,

$$\frac{d^2T_s}{dx^2}=0, \tag{2.3}$$

$$\frac{\partial^2T_t}{\partial x^2}=\frac{1}{\alpha}\frac{\partial T_t}{\partial T}. \tag{2.4}$$

The boundary conditions are also altered with the governing equation.

At the left boundary (x = 0),

$$T(0,t)=T_s(0)+T_t(0,t)=T_0 \Rightarrow \begin{bmatrix} T_s(0)=T_0, \\ T_t(0,t)=0. \end{bmatrix} \tag{2.5}$$

And the right boundary (x = L),

$$-k\frac{\partial T}{\partial x}=h\left[T(L,t)-T_\infty\right]. \tag{2.6}$$

$$-k\left[\frac{dT_s}{dx}+\frac{\partial T_t}{\partial x}\right]_{x=L}=h\left[T_s(L)+T_t(L,t)-T_\infty\right], \tag{2.7}$$

$$\Rightarrow \begin{bmatrix} -k\left.\dfrac{dT_s}{dx}\right|_{x=L}=h\left[T_s(L)-T_\infty\right], \\ -k\left.\dfrac{\partial T_t}{\partial x}\right|_{x=L}=hT_t(L,t). \end{bmatrix} \tag{2.8}$$

The final condition, which is based on the initial temperature distribution, can be adjusted in a similar method to give,

$$T(x,0)=T_s(x)+T_t(x,0)=T_i \;\Rightarrow\; T_t(x,0)=T_i-T_s(x). \tag{2.9}$$

The steady state solution (Eq. (2.3)) can be obtained using simple integration,

$$T_s(x)=c_0+c_1x. \tag{2.10}$$

The integration constants c_0 and c_1 can be determined using the boundary conditions in Eqs. (2.5) and (2.8), which produce the following result,

$$T_s(x) = T_0 + \frac{hx/k\,(T_0 - T_\infty)}{hL/k + 1}. \tag{2.11}$$

The partial differential equation of the transient solution in Eq. (2.4) can be solved using separation of variables and the solution has been shown in many sources [18]. The general solution is shown below.

$$T_t(x,t) = e^{-\alpha\lambda^2 t}\left(A\sin\lambda x + B\cos\lambda x\right), \tag{2.12}$$

where λ is the eigenvalue to be determined later, and A and B are integration constants. Applying the boundary condition in Eq. (2.5) results in the following equation,

$$T_t(0,t) = e^{-\alpha\lambda^2 t}\left(A\sin(0) + B\cos(0)\right) = 0. \tag{2.13}$$

Evaluating both the sine and cosine functions eliminates the sine function (along with constant A). Considering that the exponential function cannot reach zero, one is safe to assume that B is zero, which allows for elimination of the cosine term from the equation. The next boundary condition to be evaluated is the convective boundary condition at the right side of the sample,

$$-k\left.\frac{\partial T_t}{\partial x}\right|_{x=L} = hT_t(L,t). \tag{2.14}$$

Substituting the full equation into the boundary condition gives

$$\cot\lambda_n L = -\left(\frac{1}{\lambda_n L}\right)\left(\frac{hL}{k}\right). \tag{2.15}$$

This equation can be used to find the eigenvalues (λ_n) that are necessary for the solution. This adjusts the temperature equation to include the summation of these values,

$$T_t(x,t) = \sum_{n=1}^{\infty} e^{-\alpha\lambda_n^2 t} A_n \sin\lambda_n x. \tag{2.16}$$

Finally, the initial condition is applied to determine the values of A's, which change between eigenvalues,

$$T_t(x,0) = \sum_{n=1}^{\infty} A_n \sin\lambda_n x = T_i - T_s(x). \tag{2.17}$$

Substituting Eq. (2.11) into Eq. (2.17) yields,

$$\sum_{n=1}^{\infty} A_n \sin\lambda_n x = T_i - T_0 - \frac{hx/k\,(T_i - T_\infty)}{hL/k + 1}. \tag{2.18}$$

Because sine functions are orthogonal within the boundaries of the system, to determine A_n, both sides are multiplied by $\sin\lambda_n x$ and integrated from 0 to L, which gives

$$\int_0^L A_n \sin^2\lambda_n x\,dx = \int_0^L \left[\frac{h/k\,(T_i - T_\infty)}{hL/k + 1}\right] x\sin\lambda_n x\,dx + \int_0^L (T_i - T_0)\sin\lambda_n x\,dx. \tag{2.19}$$

Evaluating both integrals and solving for A_n yields

$$A_n = \frac{\left[T_i - T_0 - \frac{h/k\,(T_i - T_\infty)}{hL/k + 1}\right]\left[\frac{\sin\lambda_n L}{\lambda_n^2} - \frac{L\cos\lambda_n L}{\lambda_n}\right] + \left[T_i - T_0\right]\left[\frac{1-\cos\lambda_n L}{\lambda_n}\right]}{\frac{L}{2} - \frac{\sin 2\lambda_n L}{4\lambda_n}}. \tag{2.20}$$

Table 2.1 shows the first few sets of eigenvalues and constants (the properties used are shown in the table as well). The Biot number for the sample of aluminum is 0.0064, which again shows that convective heat transfer has a much smaller influence on the system than conduction. Since the series converges fairly rapidly, a good approximation may be made using only a few terms. The final temperature solution is shown below:

$$T(x,t) = T_0 - \frac{hx/k\,(T_0 - T_\infty)}{hL/k + 1} + \sum_{n=1}^{\infty} A_n \sin\lambda_n x e^{-\alpha\lambda_n^2 t}. \tag{2.21}$$

Table 2.1 Eigenvalues and Constants for Transient One-dimensional Conduction

λ_n	A_n
10.499	-45.9673
31.425	-13.5314
52.365	-8.5692
73.308	-5.91575
Material Properties:	
Thermal Conductivity (k)	237 W/m K
Convective Heat Transfer Coefficient (h)	10 W/m^2 K
Length (L)	0.15 m
Biot Number (Bi)	0.0064

Figure 2.2 shows a set of solutions using a similar set of properties as the eigenvalue calculations (Bi = 0.0064). It is clear that the temperature distribution through the sample changes drastically as time elapses. This is important for systems of this type due to the importance of temperature gradient. A high temperature gradient in the temperature profile will make it difficult to identify potential gradient anomalies due to defects, and a low temperature gradient will not provide a sufficient heat flux to create gradient anomalies.

2.1.2 One-Dimensional Conduction with Moving Heat Source

While it can provide a great deal of knowledge about an acceptable temperature distribution, a one-dimensional stationary transient conduction problem does not completely describe the mechanism involved in a true scanning infrared system. Because the heat source itself is moving, the temperature distribution will change based on how fast or slow the system is scanning. Since there is no inclusion of velocity in the previous analysis, a new set of governing equations must be used to correctly simulate a translating system.

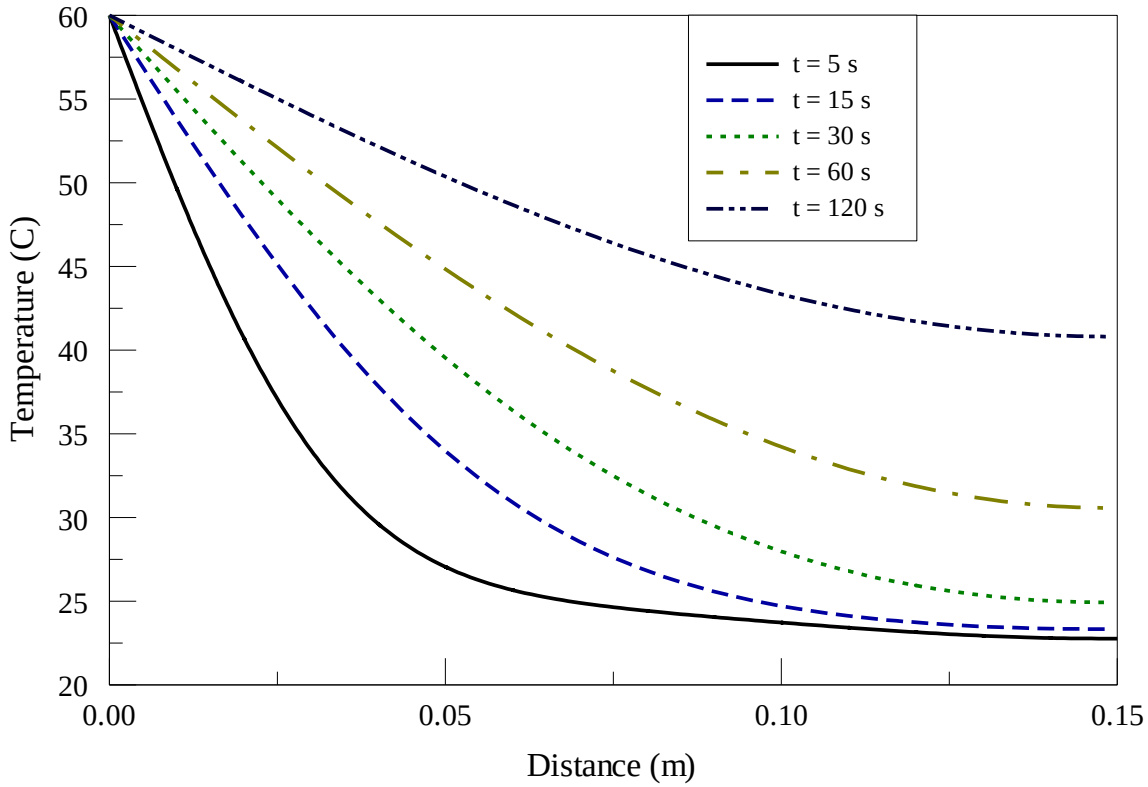

Fig. 2.2 Temperature Profiles for One-Dimensional Transient Heat Conduction.

First, an appropriate set of coordinates must be adopted. It is assumed that the temperature distribution behind the heat source will be relatively uniform, so it is important to have a coordinate system that is concerned with the local distance from the heat source, rather than a conventional coordinate system. In addition, the infrared camera used in the system will be moving with the heat source, so the camera will always be viewing a portion of the sample directly in front of the heat source. Thus, it is proposed to consider two coordinate systems – a local coordinate system (x_L) that measures the distance from the heat source, and a total coordinate system (x_T). Figure 2.3 demonstrates the difference between the two coordinate systems. If the system is moving at a constant velocity (v_t), then the two coordinate systems can be related using the following equation,

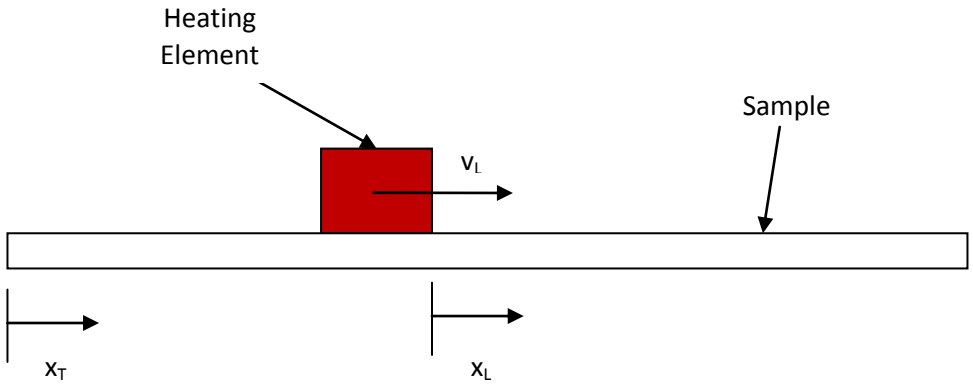

Fig. 2.3 Schematic of Two Coordinate Systems Used in the Analysis of Transient Heat Conduction with a Moving Source.

$$x_T = x_L + v_t t. \tag{2.22}$$

Again, to find the temperature distribution, we must solve the one-dimensional transient heat conduction equation,

$$\frac{\partial^2 T}{\partial x_T^2} = \frac{1}{\alpha}\frac{\partial T}{\partial t}. \tag{2.23}$$

The boundary conditions for this solution are actually simpler than the previous example. While the left boundary will still be considered as a constant temperature, it is assumed that the sample is sufficiently large that the right boundary of the sample is always at the initial temperature.

$$T\left(x_L = 0\right) = T_0, \tag{2.24}$$

$$T\left(x_T = L\right) = T_i. \tag{2.25}$$

To solve this new partial differential equation, a few derivatives must be expressed in terms of the appropriate coordinates,

$$\frac{\partial^2 T}{\partial {x_L}^2} = \frac{\partial^2 T}{\partial {x_T}^2}\left(\frac{\partial x_T}{\partial x_L}\right)^2, \tag{2.26}$$

$$\frac{\partial T}{\partial t} = \frac{\partial T}{\partial x_T}\frac{\partial x_T}{\partial t} + \frac{\partial T}{\partial t}, \tag{2.27}$$

$$\frac{\partial x_T}{\partial x_L} = 1, \tag{2.28}$$

$$\frac{\partial x_T}{\partial t} = -v_t \tag{2.29}$$

Substituting Eqs. (2.26-2.29) into Eq. (2.23) produces a new governing equation that involves only the local coordinate system,

$$\frac{\partial^2 T}{\partial {x_L}^2} + \frac{v_t}{\alpha}\frac{\partial T}{\partial x_L} = \frac{1}{\alpha}\frac{\partial T}{\partial t}. \tag{2.30}$$

It can be seen that the temperature distribution locally is only dependent on two factors: the thermal diffusivity of the material, and the translation velocity of the system. If the system is considered to move at a constant velocity, the system can be considered at steady state and all time-dependent terms can be eliminated.

$$\frac{\partial^2 T}{\partial x_L} + \frac{v_t}{\alpha}\frac{\partial T}{\partial x_L} = 0. \tag{2.31}$$

Solution of this differential equation is relatively simple, where the first-order derivative can be set as an arbitrary function, g.

$$\frac{\partial T}{\partial x_L} = g. \tag{2.32}$$

Equation (2.32) can be substituted into Eq. (2.31) to produce a differential equation only involving g,

$$\frac{\partial g}{\partial x_L} + \frac{v_t}{\alpha} g = 0. \tag{2.33}$$

The function g can be readily solved for using basic integration to give

$$g = Ce^{-\frac{v_t x_L}{\alpha}} = \frac{\partial T}{\partial x_L}. \tag{2.34}$$

Equation (2.34) can now be solved to produce the true temperature distribution equation,

$$T = \frac{-c_1 \alpha}{v_t} e^{-\frac{x_L v_t}{\alpha}} + c_2. \tag{2.35}$$

Using boundary conditions Eqs. (2.24) and (2.25), the final solution can be obtained as follows,

$$T = \left(\frac{e^{\frac{-x_L v_t}{\alpha}} - 1}{1 - e^{\frac{-L v_t}{\alpha}}} + 1 \right) \left(T_o - T_i \right) + T_i. \tag{2.36}$$

Figure 2.4 shows some temperature distributions for the moving case using material properties from aluminum (Bi = 0.0064). Unsurprisingly, varying the velocity has a dramatic effect on the temperature distribution locally. As previously discussed, it will become important for scanning purposes to identify the "ideal" scanning velocity that will produce the best opportunity for defect detection.

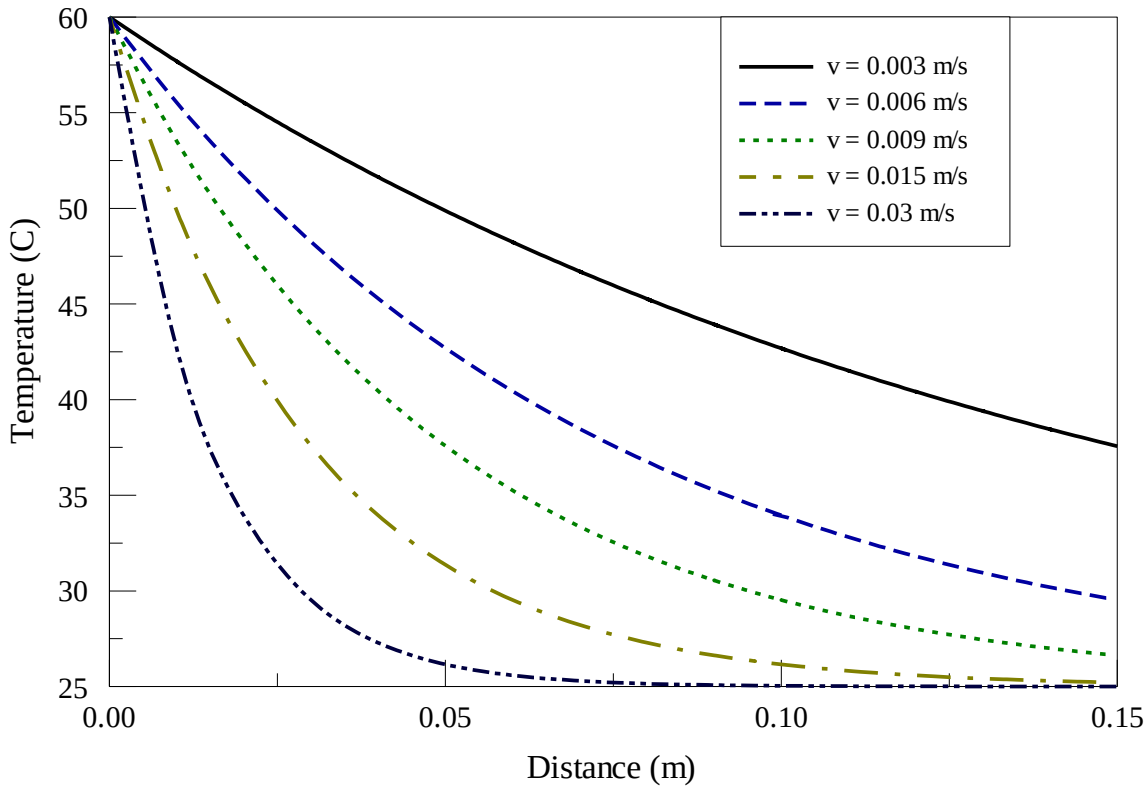

Fig 2.4 Temperature Profiles for One-Dimensional Conduction with a Moving Heat Source.

2.2 Radiative Heat Transfer

An infrared camera is used to evaluate the surface temperatures of the sample, and from those measurements the conduction theory can be applied to detect potential defects. However, the mechanism involving the radiative heat transfer from the sample surface to the infrared camera must be completely understood to ensure the true surface temperature is evaluated.

2.2.1 Emissivity and Reflectivity

The sample is viewed by an infrared camera that records the amount of radiation received (radiosity) from the surface. The radiation received by the camera comes from

three sources: the emitted radiation of the surface being measured, the incident (reflected) radiation from the same surface, and the attenuation of the fluid between them. Incident radiation is energy from outside sources that can be reflected off the surface being measured. This radiation reflects the temperature of the original surface it emanated from, not the surface being imaged. Fortunately, the amount of incident radiation that is reflected (or reflectivity) is based on the emissivity itself. It is a typical assumption that the emissivity (ε) is equal to the absorptivity (α_{abs}) of the material [4],

$$\varepsilon = \alpha_{.abs} \tag{2.37}$$

Also applicable is the relationship between reflectivity (ρ_r), transmissivity (τ), and absorptivity (α_{abs}) [4],

$$\rho_r + \tau + \alpha_{abs} = 1. \tag{2.38}$$

If the surfaces are opaque, transmissivity becomes zero, and the relationship between emissivity and reflectivity becomes,

$$\rho_r + \varepsilon = 1. \tag{2.39}$$

This shows that when emissivity is low, the reflectivity is high. Only the surface emitted radiation provides the true temperature of the source, so the other two radiation components must be eliminated or at least accounted for to obtain a true temperature profile. For the present study, the distance between the camera and the sample is sufficiently small that air attenuation effects are negligible.

As previously mentioned, infrared cameras use the Stefan-Boltzmann Law (Eq. (1.2)) to calculate temperature using the amount of incoming radiation. However, since the radiation received by the camera comes from primarily two sources, the equation must be modified to reflect those sources,

$$\varepsilon\sigma T_{surf}^4 + (1-\varepsilon)\sigma T_{ref}^4 = J \tag{2.40}$$

The first term in Eq. (2.40) represents the amount of radiation emitted directly from the surface and is representative of the true sample temperature (T_{surf}). The second term represents the amount of incident (reflected) radiation and is representative of the temperature of the original source (T_{ref}).

2.2.2 Diffusivity and Specularity

One key assumption made in the previous section is the equality of emissivity and absorptivity. This assumption can be made if the surface is considered diffuse where the emissivity and absorptivity are observed to be directionally independent. In this case, the surface is considered gray, and incident radiation scatters in many directions instead of simply bouncing off in a single direction. This dramatically simplifies many considerations that must be made in any radiative heat transfer analysis.

For surfaces that do show some directional dependence of emissivity or absorptive, they are said to be specular. In these cases, it is helpful to have a function or other relationship that describes the directional dependence of the radiation. However, most calculations are quite involved and solutions are only available for the simplest cases.

2.2.3 Directional Dependence and Shape Factors

While emissivity and reflectivity have a large impact on radiation between surfaces, the orientation of those surfaces with respect to each other also has a dramatic effect on the amount of radiation exchanged between them. The fraction of diffusely distributed radiation that leaves one surface and reaches another is known as the radiation

shape factor and is calculated using the size, shape and orientation of the two (or more) surfaces. If one is to consider the fraction of radiation received by one surface (j) that originated from another surface (i), the shape factor (F) can be calculated using the following equation,

$$F_{ij} = \frac{1}{A_i} \int_{A_i} \int_{A_j} \frac{\cos\theta_i \cos\theta_j}{\pi R^2} dA_i dA_j . \tag{2.41}$$

The shape factor considers the area (A) of each surface, the polar angle (θ) that exists between the normal vector from the surface and the line that connects both surfaces, and the distance between both surfaces (R). Numerous relationships have been developed for common surface orientations, such as parallel surfaces of different size and rectangles of different size that share a common edge and are perpendicular. These relationships have been used to create tabulated values in the form of figures and charts [19]. These specific relationships will be discussed further in Chapter 4.

CHAPTER THREE

EXPERIMENTAL APPARATUS, PROCEDURE AND ANALYSIS

3.1 Experimental Apparatus

The system's overall function is to detect thermal anomalies within a material sample by recording the surface temperature changes over time using the infrared camera. As shown in Fig. 3.1, the temperature of the material is raised by a set of resistors in direct contact with the surface. As the heat permeates the material, it alters the surface temperature, which can be recorded by the infrared camera.

3.1.1 Test Bed and Heating Element

The camera and other hardware are mounted to a plywood shelf, which is mounted on a pair of commercially available drawer slides. This allows the scanning equipment to translate in a direction parallel to the anticipated direction of the applied heat flux. The upper shelf of the test rig also has the ability to be adjusted vertically to allow for a change in camera view by bringing the sample closer to the scanning equipment. The samples are heated using a series of four 100-ohm electric resistors attached to a copper plate. The resistors are controlled by a temperature controller box that maintains the temperature of the element at 60 ºC.

3.1.2 Infrared Camera

The camera used in this application is the FLIR Thermovision A20M. The camera produces images with a resolution of 320 by 240 pixels at a maximum rate of 60 frames per second [20]. The camera can detect temperatures within the range of -20 to

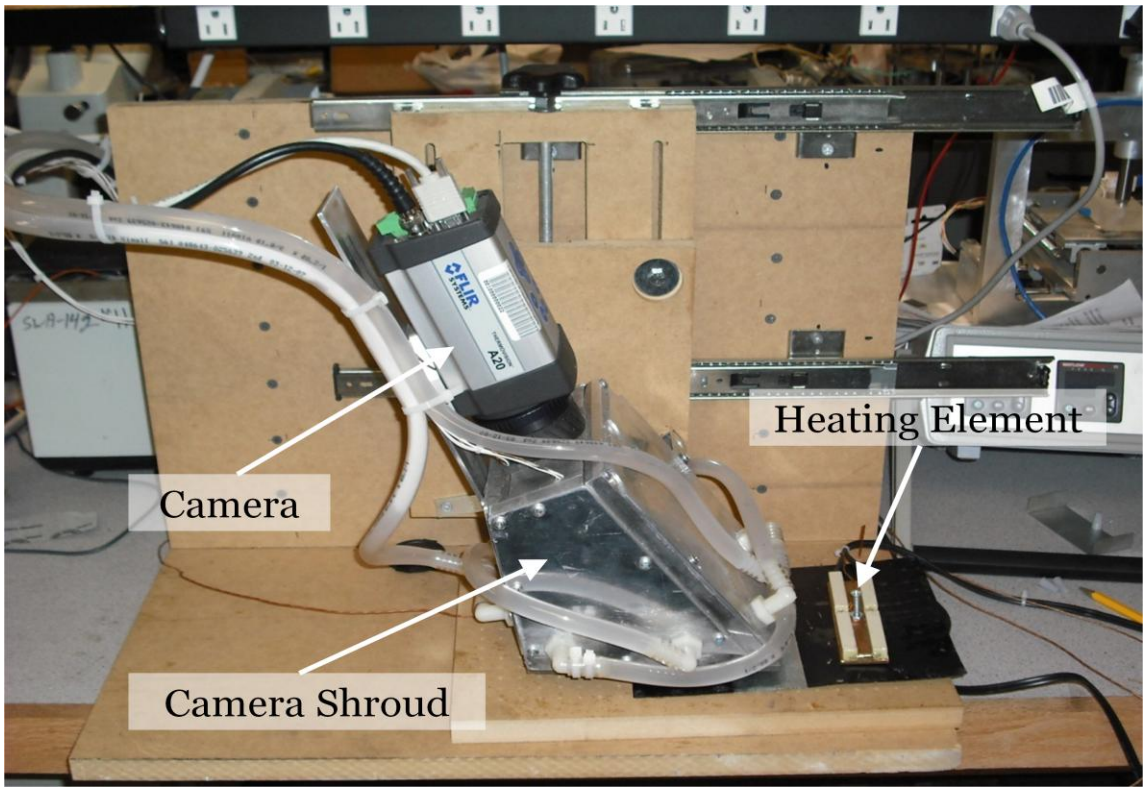

Fig. 3.1 Scanning Infrared Thermographic System (Current Version).

250 ºC with a minimum temperature resolution of 0.1ºC and reported accuracy of ± 2% [20].

In addition to the camera's ability to upload data to a computer, the camera itself has an onboard software package that allows for detailed analysis with numerous adjustable functions, including spot temperatures, boxes, minimum/maximum temperatures, and temperature alarms to fine tune data collection [20]. The camera captures the thermographic images by measuring the amount of radiation received (radiosity) through the lens from each point within the camera's view angle, which is reported to be 45º horizontally and 35º vertically [20]. However, in order to accurately determine the temperature value, the camera takes into account several environmental parameters. For precise measurements to be made, the distance to and emissivity (ε_{cam})

of the target must be known as well as the temperatures of the ambient environment and the air between the camera and the target surface (T_{amb}). Equation (3.1) shows the mathematical formula used to calculate the true temperature of the surface in question (T_{meas}), which is based on Eq. (2.40).

$$\varepsilon_{cam}\sigma T_{meas}^4 + (1-\varepsilon_{cam})\sigma T_{amb}^4 = J_{cam} \tag{3.1}$$

Only the surface emitted radiation provides the true temperature of the source, so the other radiation components must be eliminated or at least accounted for to obtain a true temperature profile. Figure 3.2 shows graphically how the radiation is received by the camera.

While the resolution and sensitivity of the IR camera itself is quite good, the operating system provided is not capable of sophisticated data manipulation or correction, such as in the case of variable emissivity surfaces. In order to maximize the camera's utility, it is best to remotely connect the camera to a computer program that allows direct control of camera settings as well as automated data collection. While the camera can be controlled quite easily by remote access, the camera still has difficulty with low and variable emissivity surfaces. The onboard software will take into account a value of emissivity specified by the user, but this value cannot be changed with any speed. Therefore, it would not be possible to continually correct emissivity if a surface being scanned had a variation of emissivity. Figure 3.3 shows two examples of the effects of reflected radiation, one of a polished metal surface (low emissivity) that reflects the camera's own heat signature (Figure 3.3(a)) and another of a partially painted surface with bare metal rivets that show a significantly higher temperature (Figure 3.3(b)). In

these cases, unheated surfaces that are in actuality at a uniform constant temperature exhibit hot or cold spots that are caused by the reflected radiation rather than a variation in the actual surface temperature.

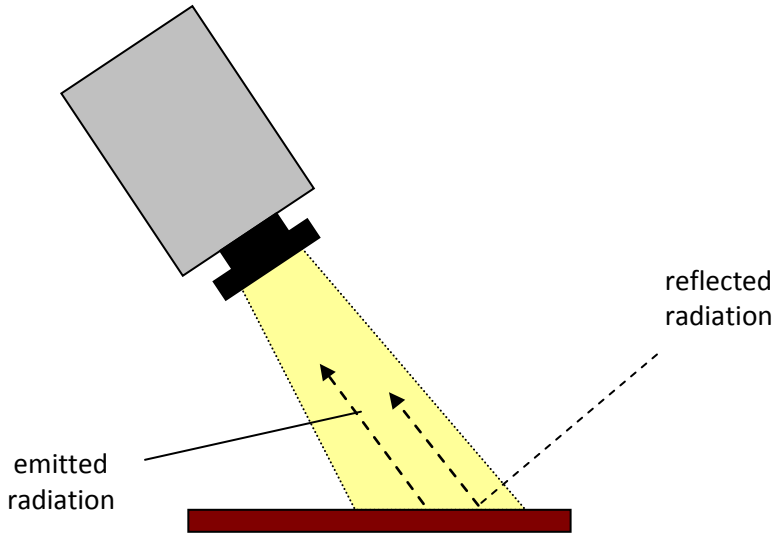

Fig. 3.2 Radiation Received by the Camera.

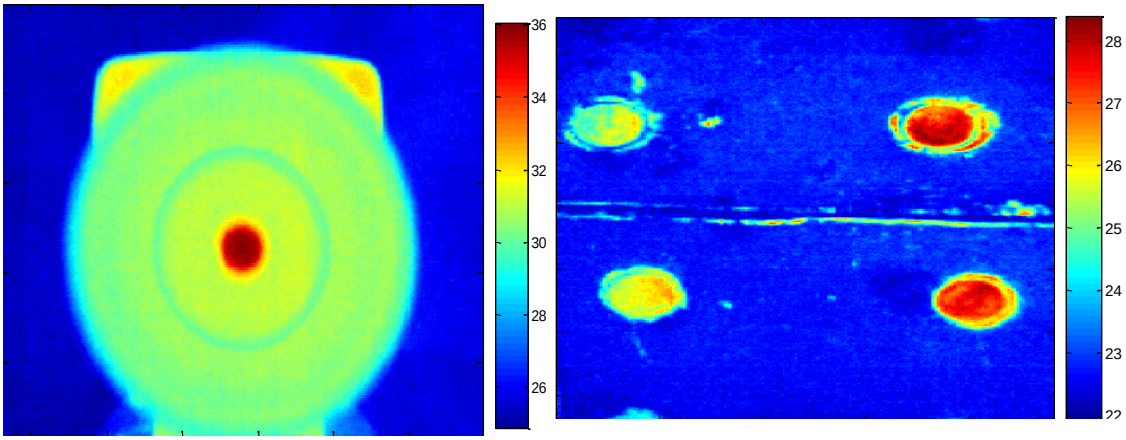

(a) (b)

Fig. 3.3 Examples of Reflected Radiation: (a) Reflection of Camera's Heat Profile from Isothermal Surface with Low Emissivity (0.3), (b) Image of Bare Rivets on Isothermal Painted Surface, Temperature Differences Caused by Emissivity Variation.

3.1.3 Camera Shroud

While it may appear to be a rather simple procedure to account for superfluous incident radiation in the image, the situation can be quickly compounded if there is significant temperature variation in the ambient environment. While the camera's on-board software has the ability to account for uniform reflected radiation, it has no mechanism to account for variations in this parameter.

Reflected radiation can be difficult to treat because in order to properly quantify it one must know the temperature of origin for each point that is reflected. In an open space, this can prove quite difficult, especially if there are numerous items or areas in the room with different temperatures. The shroud is intended to block as much non-uniform reflected radiation from outside sources by surrounding the area between the camera lens and the sample being tested. Hence, the only reflected radiation will presumably be from the shroud itself, which can be maintained at a prescribed temperature.

Previous versions of the camera shroud proved unsuccessful at maintaining a uniform temperature, so a new shroud, shown in Fig. 3.4, was constructed from aluminum because of the material's high thermal conductivity. To maintain the temperature, the aluminum is carved with channels through which heated water flows that are kept at a specific elevated temperature by a constant temperature bath. Each of the 4 sides of the shroud is heated by its own flow, which allows the shroud to not only reach equilibrium quickly, but also maintains the temperature within a narrow band.

In addition, keeping the shroud at an elevated temperature is beneficial because it allows the IR camera to more easily discern the difference between the incident and emitted radiation. This discerning ability is important if the surface emissivity is to be

Fig. 3.4 Camera Shroud.

calculated from the unheated image. If the shroud were at approximately the same temperature as the surface, it would be essentially impossible to uniquely calculate the emissivity.

While a shroud can be successful at obstructing the outside radiation that would reflect off the material surface, the image can still be marred by the camera's own reflection off the surface. In order to remove the non-uniform heat signature of the camera from the images, the camera must be oriented such that the radiation emitted from the camera housing has no clear path to return to the camera's lens as reflected radiation. Images were taken at 5° increments from normal to the captured surface until the camera's heat signature was no longer visible. In this case, the shroud and camera are tilted at 27° relative to the normal of the surface being measured in order to eliminate this effect. This adjustment of camera angle is shown in Fig. 3.5.

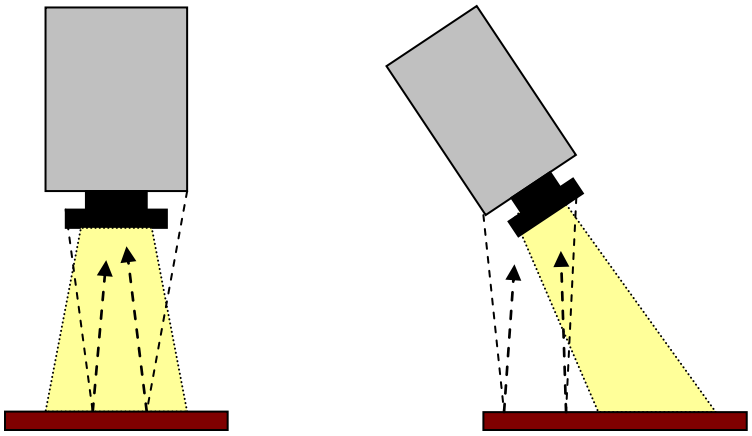

Fig. 3.5 Variation of Camera Angle and Its Effects on Reflected and Received Radiation.

3.2 Experimental Procedure

The procedure for checking defects in a sheet material begins with placing the sample in the apparatus where it is only contacted in a few small areas. This makes sure that little or no heat transfer occurs between the part and the holding apparatus. For each sample, the ultimate goal is a corrected thermal image that shows any defect where the temperature gradient is unusually high. To this end, it is necessary to acquire not only the raw temperature image, but also a cold image where the temperature is uniform and at ambient conditions. This image, captured first, will be used to calculate the emissivity of the surface, which will in turn be used to correct the image that is actively heated.

In preparation for the two-step scanning process (first a "cold" or unheated image is captured followed by a heated gradient image), the heating element is placed over one edge of the part with the radiation shielding as close to the part as possible. The portion of the image nearest the radiation shielding will be the top (in terms of the camera view), where the shroud will be as close to the material without touching to prevent stray radiation from skewing the data. Once both the heating element and camera/shroud

assembly are in place, the LabView data collection program can be activated. Initially, this program continually updates the image, but does not store any data. At this point, one can take advantage of the cropping, data reduction, and noise reduction options in the program to contour the program settings to their specific need.

The heating element is then turned on to begin sample heating. Heat begins to propagate along the material and images can be taken at whatever time intervals deemed necessary. Testing has shown that most samples are heated to acceptable temperatures after 30-60 seconds, depending on the size and thermophysical properties of the material. One must be cautious, however, to avoid prolonged exposure of the samples to high heat, which can not only damage the surface coating but also the integrity of the part. Since the surface temperatures of the sample are elevated slightly above the room temperature, this can also avoid the complication caused by the temperature-dependent emissivity.

As previously stated, the infrared camera images are sometimes skewed by the effect of reflected radiation, where the temperatures shown in the images are not the temperature of the surface being measured but in fact the temperature of a surface simply being reflected. While there have been physical adjustments in the hardware to minimize and accurately depict the amount of reflected radiation present in the signal, it is still necessary to remove it to obtain the true surface temperature. Our solution to this problem takes into account not only the raw image temperature, but also the camera settings that created the image (emissivity, ambient temperature, etc.). The solution is based on the principle that the amount of radiosity in the raw image can be corrected by determining the amount of reflected radiation and simply subtracting it, leaving only the emitted radiation.

$$\varepsilon_{cam}\sigma T_{meas}^4 + (1-\varepsilon_{cam})\sigma T_{amb}^4 = J_{cam} = \varepsilon_{actual}\sigma T_{actual}^4 + (1-\varepsilon_{actual})\sigma T_{ref}^4 \quad (3.2)$$

The above equation shows the differences between how the camera interprets the radiosity values as temperature (left side of the equation) and what the true interpretation is (the right). On the left, the temperature value for each pixel (T_{meas}) is calculated using the set camera values for the emissivity (ε_{cam}) and the ambient temperature (T_{amb}). On the right, the temperature values for each pixel (T_{actual}) are calculated using the true emissivity at each point (ε_{actual}, calculated from the unheated image) and the reflected temperature (T_{ref}), which represents the average temperature of all reflected radiation.

To calculate the true temperature values for a surface that is partially heated (T_{actual}), the other values in the equation must be known, or at least estimated. The uncorrected temperature (T_{meas}) as well as the camera emissivity (ε_{cam}) and ambient temperature (T_{amb}) are known, which leaves only the true emissivity (ε_{actual}) and reflected temperature (T_{ref}) to be determined to correct the image. The reflected temperature can be taken as the temperature of the interior of the camera shroud, which is assumed to be uniform and constant. Therefore, the only variable left unknown is the true emissivity that can be calculated from Eq. (3.2) to give

$$\varepsilon_{actual} = \frac{\varepsilon_{cam}T_{meas}^4 + (1-\varepsilon_{cam})\sigma T_{amb}^4 - T_{ref}^4}{T_{actual}^4 - T_{ref}^4}. \quad (3.3)$$

As previously stated, the camera values of emissivity and ambient temperature are known, as well as reflected temperature. To calculate the actual emissivity, only the actual temperature needs to be known. For this calculation, the cold image can be used, since the surface temperature can be verified with a thermocouple or other temperature

reading device and used as the actual temperature. Once all the variables are known, emissivity can be calculated for all pixels in the image. When the true emissivity is known, the heated images can be corrected to give

$$T_{actual} = \sqrt[4]{\frac{\varepsilon_{cam}\sigma T_{meas}^4 + (1-\varepsilon_{cam})\sigma T_{amb}^4 - (1-\varepsilon_{actual})T_{ref}^4}{\varepsilon_{actual}}}. \tag{3.4}$$

The actual temperature values for each pixel can be calculated using the camera settings and the newly found emissivity values as well as the reflected temperature of the camera shroud. One difficulty encountered in using this method is the sensitivity of measurements at or near ambient conditions. If the expected surface temperature is at or near the reflected temperature, it can cause a near-zero condition in the denominator of Eq. (3.3). Therefore, to use this method, the reflected temperature (in this case the temperature of the camera shroud) should be high enough to avoid this problem.

After the images have been stored, the next step is to remove the effects caused by reflected radiation if necessary. This would be necessary in cases where the emissivity varies over the surface or is uniformly low. If it is not required, or after the removal has been performed, the next step is the final data conditioning where noise can be removed with a variety of filters and a gradient image can be created. Finally, the gradient images can be inspected for suspect areas where the gradient is unusually high. These areas of higher gradient are areas that need to be closely inspected on the surface itself and checked for signs of damage.

3.3 Software and Computer Program

As previously stated, the images captured by the camera can be misrepresentations of the actual surface temperature. The digital images have some amount of noise present, as well as errors in the form of reflected radiation that produce an incorrect temperature distribution. In addition to correcting the error in the images, it is also convenient to create options to adjust images to save memory, remove unwanted data, and create more meaningful images. Therefore, it is necessary to create a software package that not only provides these options, but also is fairly simple in its construct so that personnel with limited computer knowledge can use it with ease. The previous version of this procedure was performed using 3 programs in two different software packages, but the newest procedure allows for all data processing and modification in a single LabView program, shown in Fig. 3.6.

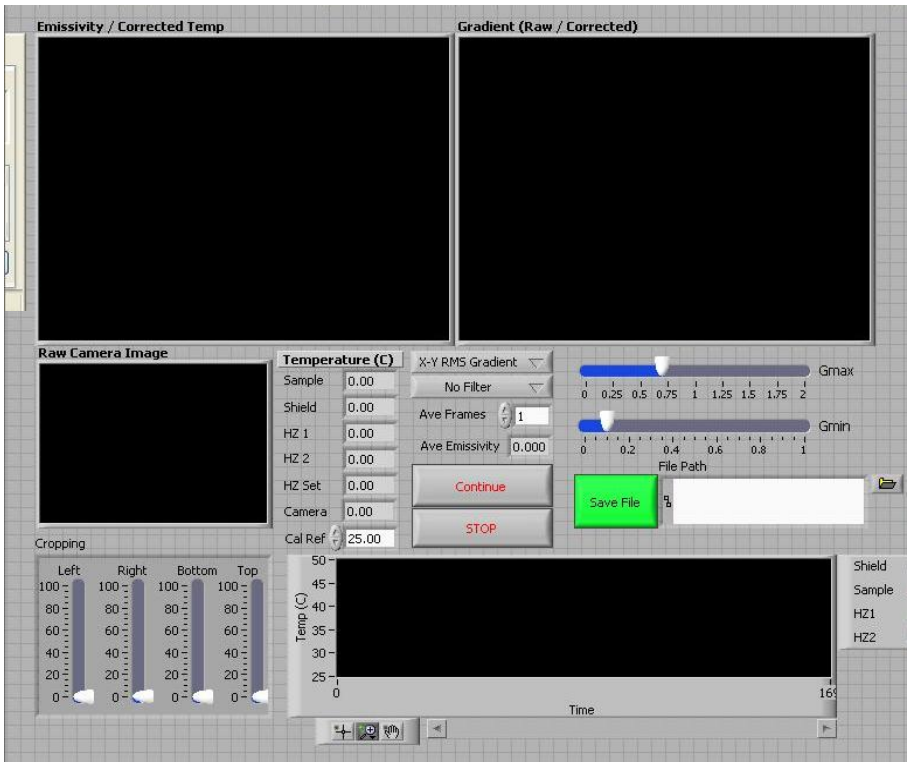

Fig. 3.6 Screenshot of LabView Program.

3.3.1 Cropping and Data Reduction

The first step in analyzing the images produced by the camera is to determine whether the raw image needs to be cropped or reduced in resolution. The program allows for adjustments to the image in terms of size and quality before data collection. The two methods available for size change are the cropping function and the data reduction function. The cropping function, as the name suggests, is simply the ability to remove lines of data from all 4 sides of the image. This could be necessary due to misleading data at one edge of the camera's view (edge of a sample, an extraneous reflection, etc.) or to simply close in on a particular area of interest. The current function has the ability to remove up to 100 lines from any side if required.

The data reduction function is provided to create an opportunity to reduce the amount of data that is recorded without decreasing the image acquisition speed. The current output of the program is a text file of an array of temperature values that approaches 500 kilobytes of data (unaltered) for each image. The amount of required data storage can quickly mushroom depending on the time lapse between images. Therefore, it could be necessary to reduce the amount of data while still preserving the general image properties.

The reduction of image size is performed by taking a prescribed block of pixels and averaging them (4 in the case of ½ reduction, 9 in the case of 1/3 reduction, etc.) to create a single value that is representative of the whole. In this fashion, an image's storage space can be reduced by significant amounts (75 percent in the case of ½ reduction, 89 percent in the case of 1/3 reduction). However, this can create a risk of missing smaller sized defects due to a lower resolution image.

3.3.2 Emissivity and Raw Gradient

After these corrections have been made, data collection can begin. First, Eq. (3.2) is used along with the cold image to determine the emissivity map of the surface. This allows for a more detailed depiction of the amount of reflected radiation for each pixel. The raw gradient can also be seen at this time, although the information is still unavailable, since the surface has yet to be heated.

3.3.3 Corrected Temperature and Gradient

Once the emissivity has been calculated, the "Continue" button is selected and the heating element is applied to the surface to begin active heating. The emissivity and raw (cold) image are saved for future reference.

After the emissivity map has been created, the reflected radiation can be removed from the hot image using Eq. (3.3). This new image can be viewed in the window labeled "Corrected Temperature," with the "Corrected Gradient" directly next to it.

3.3.4 Noise Reduction/Gradient

Because the image produced is an electronic signal originally, it naturally contains noise that can be reduced to make the image sharper. The sliders positioned below the thermographic images are designed to filter image noise while attempting to detect thermal anomalies. There are three options in terms of reducing the amount of noise present in the signal: the mean filter, the median filter, and the mean gradient filter. The three options all have advantages and disadvantages in terms of removing different types of noise.

The mean filter is the most simplistic of the three filters. For each pixel, as shown in Eq. (3.5), the filter takes the surrounding 8 pixels and averages them together with the original to create a new value, and does the same for all pixels in the image.

$$T_{i,j} = \frac{\sum_{k=-1}^{1}\sum_{m=-1}^{1} T_{i+k,j+m}}{9} \tag{3.5}$$

This serves to smooth the image and reduce noise, but it also has the side effect of blurring hard edges that can be potentially important.

The median filter addresses the liability of the mean filter, which is the distortion of edges and corners. This filter takes the subject pixel, along with the surrounding 8 pixels and sorts them from highest to lowest. After sorting, the median value is selected and used to replace the pixel being filtered. The median filter has the advantage that it does not inherently blur or damage corners and edges that appear in the image. Also, its product is all original data whereas the mean filter is capable of producing pixel values that were not present in the original image. However, the median filter is more computationally intensive, due to the required sorting, and can slow real time analysis.

The final filter, the mean gradient, is a newly created filter of our own design. Its design is to calculate the center point of the nine pixels selected and recalculate it based on the forward and backward differences in both x and y directions. The differences are calculated not with the two points, but the average of the 3 pixel values in the corresponding row or column.

$$T_{i,j} = T_{i+1,j} - \left[\left(\frac{1}{3}\sum_{k=-1}^{1} T_{i+1,j+k}\right) - \left(\frac{1}{3}\sum_{k=-1}^{1} T_{i,j+k}\right)\right] \tag{3.6}$$

$$T_{i,j} = T_{i-1,j} - \left[\left(\frac{1}{3} \sum_{k=-1}^{1} T_{i-1,j+k} \right) - \left(\frac{1}{3} \sum_{k=-1}^{1} T_{i,j+k} \right) \right] \tag{3.7}$$

$$T_{i,j} = T_{i,j+1} - \left[\left(\frac{1}{3} \sum_{k=-1}^{1} T_{i+k,j+1} \right) - \left(\frac{1}{3} \sum_{k=-1}^{1} T_{i+k,j} \right) \right] \tag{3.8}$$

$$T_{i,j} = T_{i,j-1} - \left[\left(\frac{1}{3} \sum_{k=-1}^{1} T_{i+k,j-1} \right) - \left(\frac{1}{3} \sum_{k=-1}^{1} T_{i+k,j} \right) \right] \tag{3.9}$$

After all 4 differences are calculated, 4 potential center pixel values are calculated, and then averaged to create a new center value. While this method is excellent for creating a filter that smoothes the data based on an accurate gradient, it favors the edge points over the corner points by a 2 to 1 margin when performing analysis.

After noise reduction, the program creates a temperature gradient image, presumably showing areas where heat flux has slowed, creating a high gradient. Currently there are two gradient methods available in the program, the RMS gradient and the max/min gradient. The RMS gradient calculates the gradient for each pixel based on the following formula:

$$G_{i,j} = \sqrt{\left(T_{i-1,j} - T_{i+1,j}\right)^2 + \left(T_{i,j-1} - T_{i,j+1}\right)^2} \tag{3.10}$$

This provides a combination of both x and y gradients at each point. The max/min gradient is calculated by locating the maximum and minimum values within the 9 pixels analyzed and subtracting the two to create the highest gradient possible. While the RMS gradient creates a more accurate account of the gradient at each point in terms of a true gradient value, the max/min makes the gradients more visible. However, the max/min gradient requires a sorting of values to detect the maximum and minimum, which is computationally intensive and can slow the data processing.

CHAPTER FOUR

COMPUTATIONAL MODELING OF SCANNING INFRARED THERMOGRAPHY

The system presented within has already proven successful in several applications. However, there are many questions that one must address before the system can be used in a true industrial application. First, what is the defect resolution of the system, or the smallest defect that can be detected by the current system? Second, since the removal of reflected radiation has only been somewhat successful, is the reflected radiation being correctly quantified? Third, if the complete removal of reflected radiation proves to be impossible, is coating a feasible option that would successfully (and inexpensively) raise the emissivity of the samples to a point where reflected radiation can be ignored? Fourth, what additional steps must be taken in analysis and configuration to automate the current system to make it a true scanning infrared thermography system? And finally, can the system handle other materials, in particular non-metallic materials such as composite resin and thermoplastics?

While the third and fifth questions concern experimental testing (which will be addressed in Chapter Five), the remaining questions can all be addressed using computational modeling. The issue of detection resolution will be tested using both ANSYS simulations and a newly developed computational heat transfer program in MATLAB. Several defect geometries will be simulated in both programs to determine what minimum, if any, exists for defect detection. The issue of radiation quantification will be determined using radiation analysis; the shape factor of the camera shroud, as well as the sample itself, will be determined and the amount of radiation from a simple

geometry will be calculated and compared to the expected value from our traditional analysis. The issue of automation will be addressed using a set of derived equations as well as some basic program considerations and flowcharts.

4.1 Analysis of Defect Resolution Using Computational Models

As previously mentioned, one desired trait of the system is the determination of its resolution – that is the minimum size of defect that can be successfully detected. While this is a complex question, there are several options available to successfully determine this value. While experimental testing may be the only way to truly determine the resolution of this system, manufacturing defects on a continually smaller scale will prove increasingly difficult. In addition, the current apparatus has a fixed field of view; due to the size of the camera shroud, the camera will always be at a fixed distance from the samples being tested. Without the ability to move the camera closer to the sample, it is impossible to determine whether the resolution can be continually increased by moving the camera closer to the sample.

Therefore, computational models will be used to help determine the potential resolution of this system. Two methods will be used – first using a commercial software package (ANSYS) to create samples under the same testing conditions as our experiment and simulate an actual test. Second, a two-dimensional transient heat conduction model will be developed using MATLAB that will again simulate a testing environment. Both models will be compared to experiments previously performed as well as each other.

4.1.1 ANSYS Modeling

A simple model was developed using ANSYS to verify the previous experimental results [21]. A simple rectangular geometry was produced using Pro/ENGINEER (30 cm long, 20 cm wide and 0.13 cm thick). A variety of defects (cracks, void and thinning) were investigated using the geometry. Rather than imposing complex heat transfer conditions, the ANSYS models applied simple constant temperature boundaries on the left and right, and insulated condition on the top and bottom surfaces. Also, instead of transient solutions, steady-state solutions were sought after using the ANSYS models. The material properties of aluminum listed in Table 2.1 were used in the models.

a. Crack Results

Figure 4.1 shows the temperature gradient image of a longitudinal crack which is perpendicular to the direction of heat flow from the ANSYS model. The crack is clearly visible as a region of higher gradient in the center of the sample. When the crack is oriented in a different direction, as it is shown in Figs. 4.2 and 4.3 respectively, the crack becomes less visible. Figure 4.2 shows the gradient image of a crack oriented at 45° with respect to the heat flux, and Fig. 4.3 shows the gradient image of a "parallel" crack oriented in the direction of the heat flow. In the 45° case, the crack is still highly visible, but in the parallel case the crack is not visible. This is not unexpected because the gradient in the image is directly dependent on the amount of area removed in the direction perpendicular to the heat flux. In the parallel case, the amount of area removed in this case is very small, so there is little gradient.

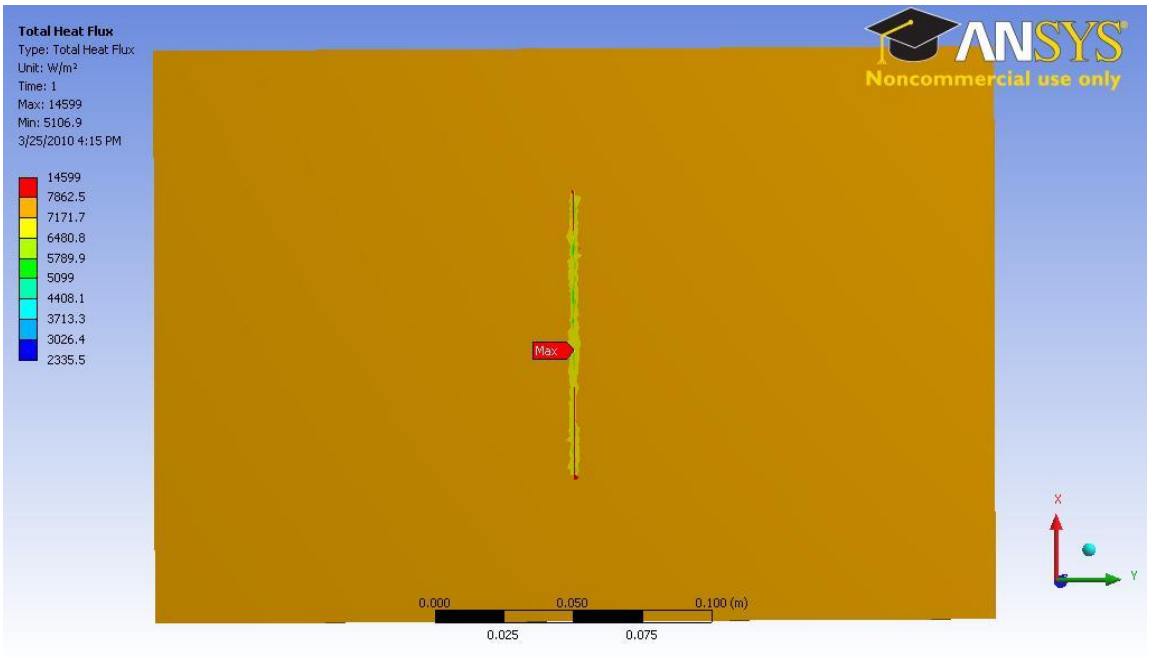

Fig. 4.1 Image of Temperature Gradient Resulting from a Longitudinal Crack from ANSYS Model.

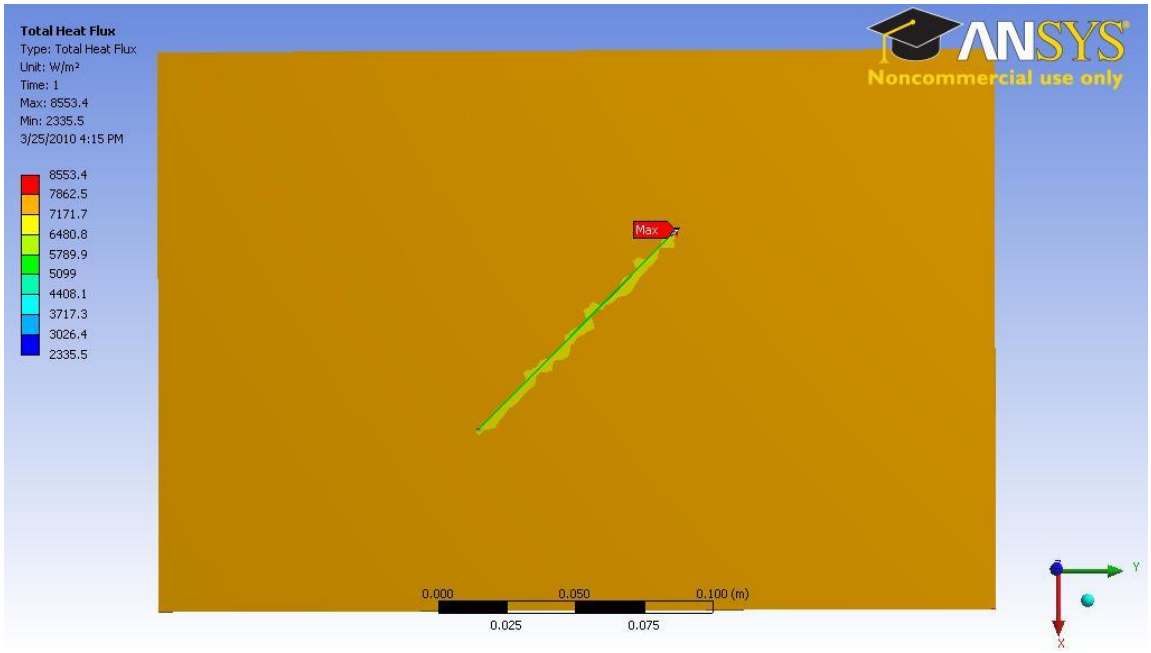

Fig. 4.2 Image of Temperature Gradient Resulting from an Angled Crack from ANSYS Model.

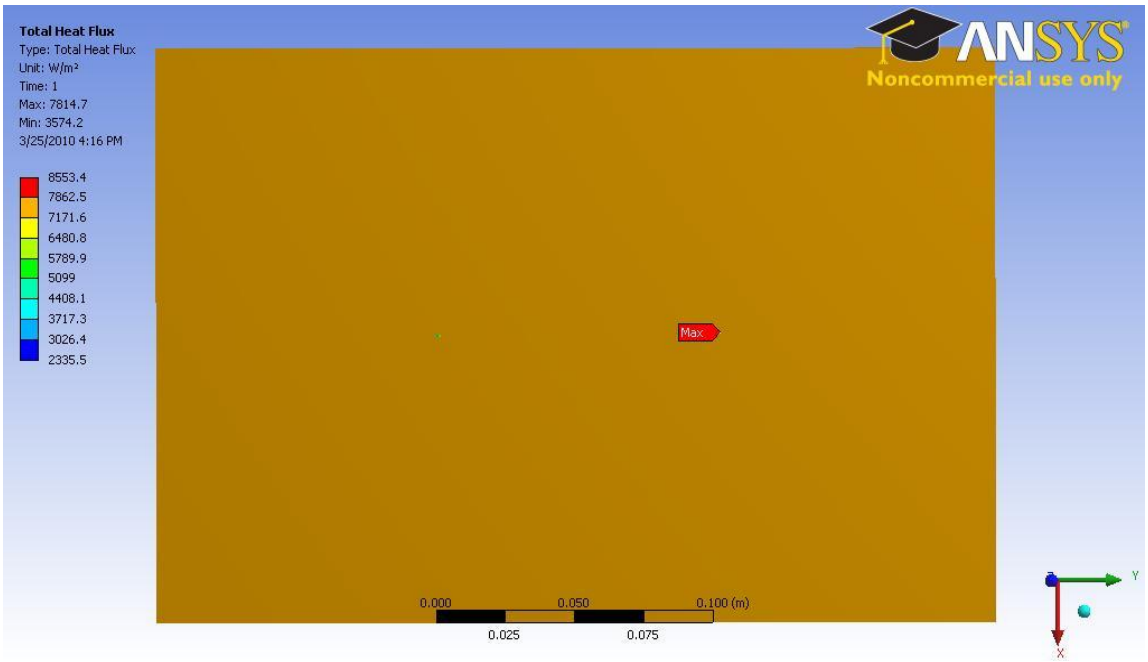

Fig. 4.3 Image of Temperature Gradient Resulting from a Parallel Crack from ANSYS Model.

b. Void and Thinning Results

Figure 4.4 shows the Pro/ENGINEER model used for the simulation of a thinning. The thinning itself is a 5 cm square that reduces the thickness of the sheet by half. The edges of the thinning are beveled so that there is not an abrupt change in thickness. Figure 4.5 shows the temperature gradient image of the thinning from ANSYS. The thinning is clearly visible in the image, especially at the edges of the thinning. This is due to the effect of reduction in the cross-sectional area on the heat flux locally.

Figure 4.6 shows a close-up view of the void cross-section produced by Pro/ENGINEER. The void is a 1.25 cm square that is beveled at the edges. Figure 4.7 shows the temperature gradient image produced by ANSYS. The gradient image looks

similar to that of the thinning case previously discussed because both are resulted strictly from a reduction in the cross-sectional area which causes a change in heat flux.

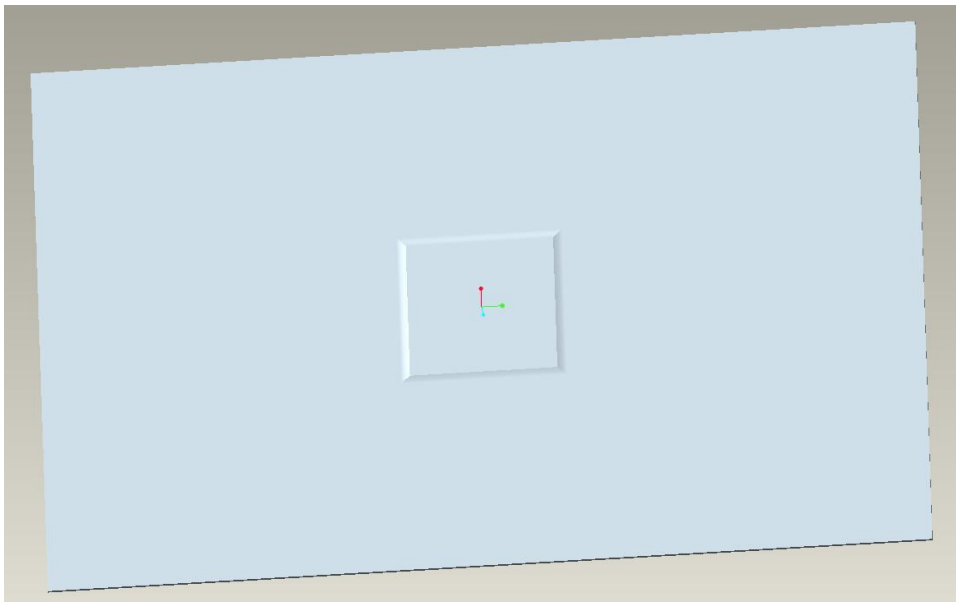

Fig. 4.4 Pro/ENGINEER Model of Thinning

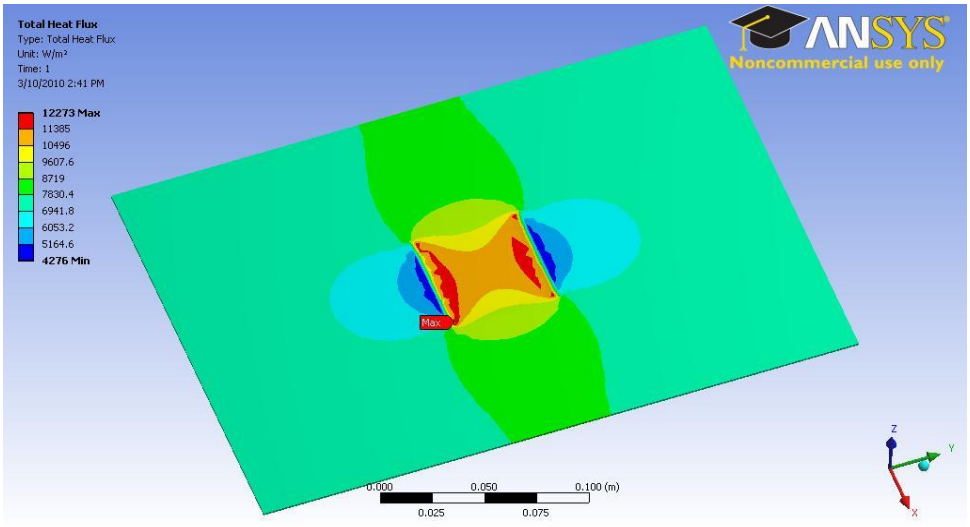

Fig 4.5 Image of Temperature Gradient Resulting from a Thinning from ANSYS Model.

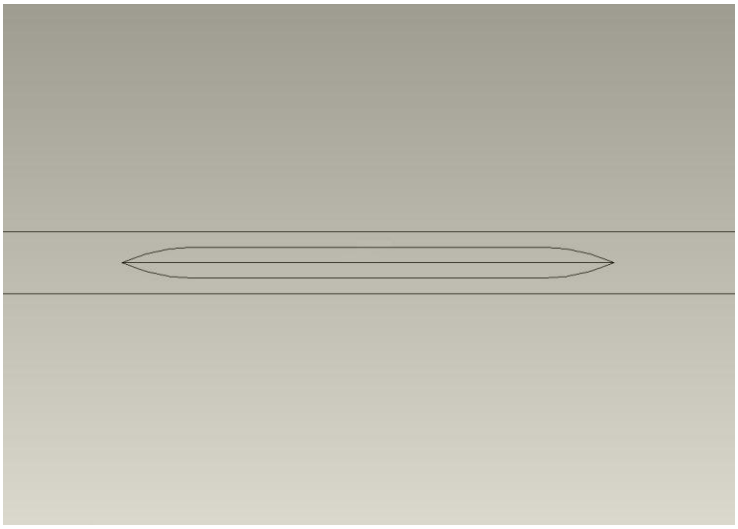

Fig 4.6 Close-up View of Void Cross-section.

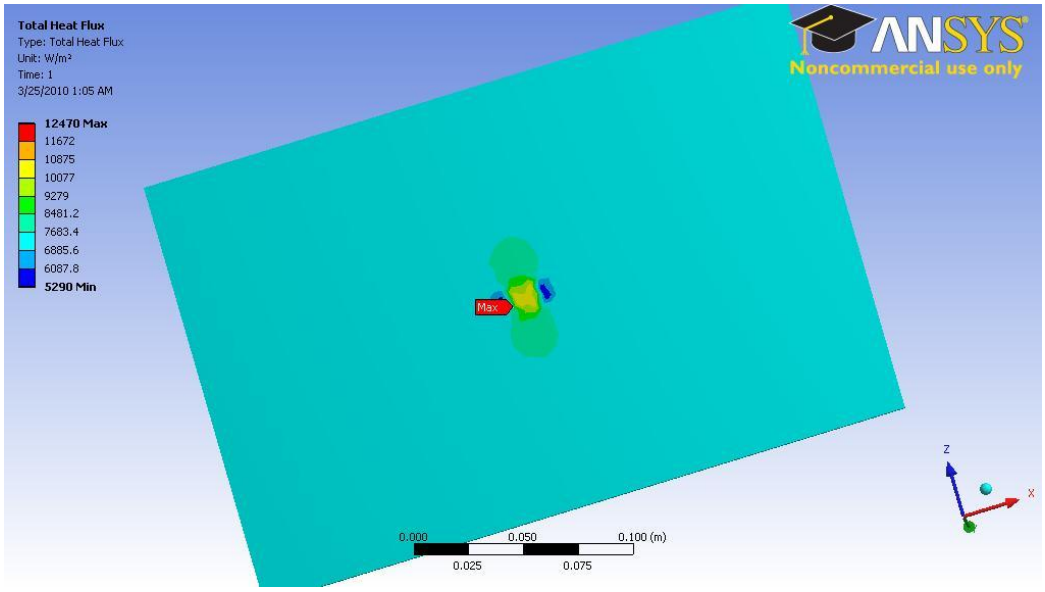

Fig. 4.7 Image of Temperature Gradient Resulting from a Void from ANSYS Model.

4.1.2 Two-Dimensional Transient Analysis

a. Model Development

A two-dimensional transient heat conduction program was developed using traditional numerical algorithms. The program (shown in Appendix) uses the two-dimensional explicit difference equations to calculate the temperature distribution at a new time step based on the previous values [19]. If the material does not have internal heat generation, the equation for internal nodes can be simplified as (full solution in Appendix):

$$T_{i,j}^{m+1} = T_{i,j}^{m} + \alpha\Delta t\left\{\frac{T_{i+1,j}^{m} - 2T_{i,j}^{m} + T_{i-1,j}^{m}}{\Delta y^2} + \frac{T_{i,j+1}^{m} - 2T_{i,j}^{m} + T_{i,j-1}^{m}}{\Delta x^2}\right\} \qquad (4.1)$$

In the above equation, the new temperature distribution (T^{m+1}) is calculated using the temperature distribution previously calculated (T^{m}), as well as using the size of the elements (Δx, Δy), the time step (Δt), and the thermal diffusivity (α). Two boundary conditions are used for this program – the left boundary is maintained at a constant temperature of 60°C which is meant to simulate our heating element, and the other 3 boundaries use a natural convection boundary condition. For example, here is the condition used for the right boundary (which is column "M"):

$$T_{i,M}^{m+1} = T_{i,M}^{m} + \frac{2\Delta t}{\rho c\Delta x^2}\left\{k\left(\frac{T_{i+1,M}^{m} + T_{i-1,M}^{m}}{2} + T_{i,M-1}^{m} - 2T_{i,M}^{m}\right) - h\Delta x\left(T_{i,M}^{m} - 2T_{\infty}\right)\right\} \qquad (4.2)$$

The temperature of the boundary nodes are calculated using the thermal conductivity (k), density (ρ) and specific heat (c) of the material as well as the heat transfer coefficient (h), which is calculated using the fluid properties of the air, including temperature (T_∞).

While these equations are extremely powerful and can be used to handle most two-dimensional problems, they assume a uniform composition for the material in question, with no material anomalies. Therefore, in order for these equations to be used for this analysis, they must be modified to accommodate variations in the material. It is proposed to model crack defects as thermal contact resistance, where the material properties in the crack are assumed to be that of air. Figure 4.8 shows how the grid is altered to allow for this change.

Because this is an explicit finite difference method, the time step for each iteration is critical due to the potential for divergence of solutions. The time step is calculated using the smaller of the two grid dimensions (Δx, Δy):

$$\Delta t = \frac{\Delta x^2}{4\alpha} \tag{4.3}$$

The equation is similar to the calculation of Fourier number, with the exception that a

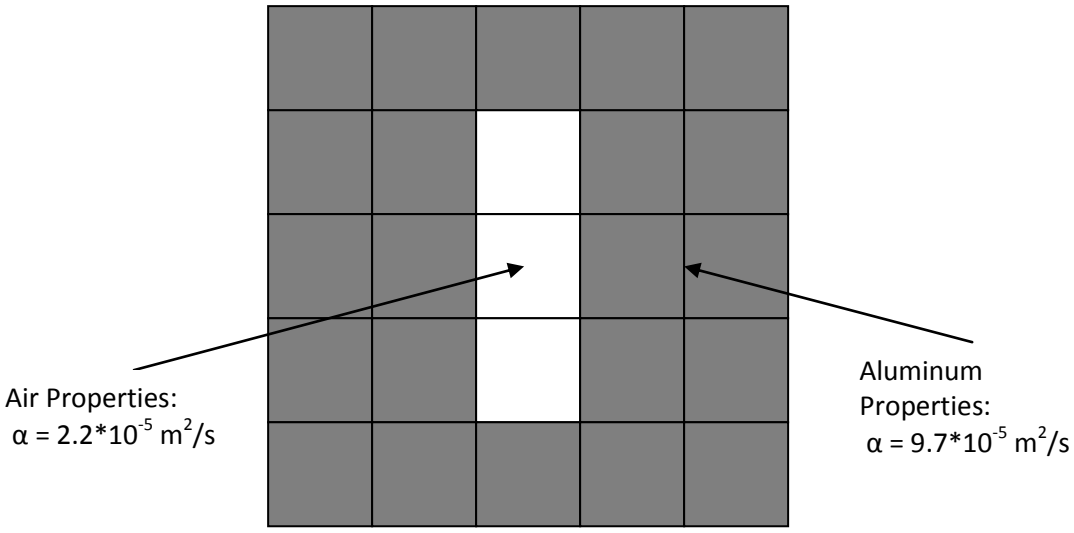

Fig 4.8 Numerical Grid Used for the Longitudinal Crack Simulation.

factor of 4 has been used instead of 2 to again prevent the solution from divergence. The program proceeds using this time step until the total time elapsed is above the time input to the program.

Once the program has calculated the final temperature array, the temperature gradient can be calculated similar to Eq. (4.2). The program prints a contour plot of both the temperature of the surface as well as the temperature gradient. Both time and defect size can be varied to evaluate the success of detection for each type of defect. Currently, the sample size is a square of 0.15 m and a grid size of approximately 0.00075 m in both dimensions, which is similar to the size and image resolution of the experimental tests. The material properties used in the program are that of pure aluminum. The ambient air conditions are 25°C and a heat transfer coefficient of 12 $W/m^2 K$.

b. Results – Longitudinal Crack

The first model tested is the first experimental test ever successfully completed by our system, a longitudinal crack. In the program, a crack is simulated by using the thermal properties of stagnant air for one grid size in the center of the sample. The goal of these analyses is to determine what the resolution of the system is with respect to a longitudinal crack. The first case analyzed was a 2 cm crack in the center of the sample.

Figure 4.9 shows a sample of gradient images produced for the 2 cm longitudinal crack (the remaining images can be found in the Appendix B). The crack is clearly visible at several time periods (10, 15, 30, and 60 seconds) where the temperature gradient is significantly higher than the surrounding surface. However, the crack becomes more or less visible depending on the time elapsed. This is because of the change in the temperature distribution over that time – the more time that has elapsed, the

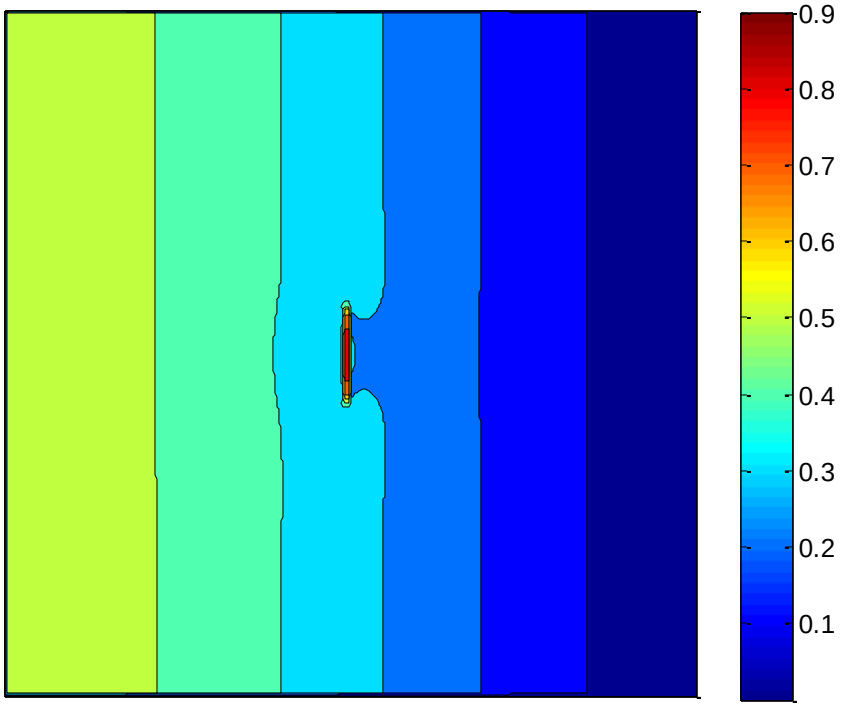

(a)

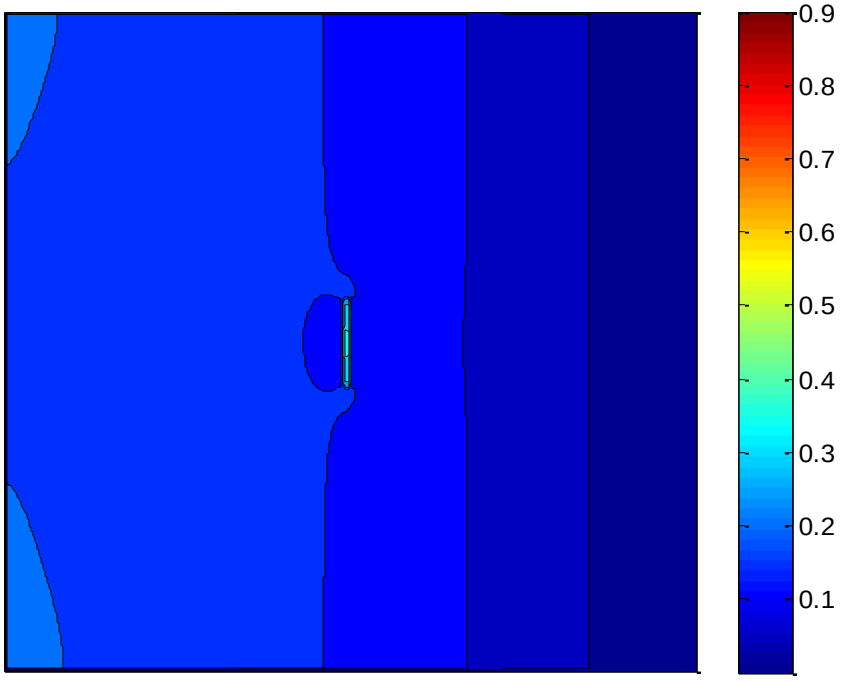

(b)

Fig 4.9 Images of Temperature Gradient for a 2-cm Longitudinal Crack, (a) at 15 seconds, (b) at 60 seconds.

lower the temperature gradient is throughout the sample. It will become an important issue when the system is automated to correctly adjust the translation velocity so that the average temperature gradient on the surface is high enough to produce meaningful results.

Previous experimental results have shown success at detecting a crack 1 cm in length, therefore the next crack size to analyze will be a crack of 0.5 cm. Figure 4.10 shows the results of this analysis. In this case, the reduction in size of the crack had a drastic effect on the detection ability; the temperature anomaly is significantly smaller due to the smaller area of defect. In addition, the crack is only plainly visible in a shorter time frame (10, 15, 30 seconds). This is also not unexpected because the heat flux has a shorter path to move around the defect, and therefore less time is required for the heat to go past the defect.

c. Results – Angled Crack

Another consideration for crack defects is the orientation of the crack with respect to the direction of heat flux. Prior studies have shown that a less than optimal angle will lead to difficulties in detection due to the ease of heat passing around the defect. A 3 cm crack is analyzed, but it is oriented at 45° with respect to the direction of heat transfer. The crack was modeled in a similar fashion to the longitudinal cracks previously discussed. Figure 4.11 shows how the grid is altered for this analysis.

Figure 4.12 shows the results of the analysis. As expected, the crack is highly visible in the first 60 seconds of heating and becomes less visible after that. An interesting observation to note is that while the crack is approximately 3 cm long, because it is oriented at a less than optimal angle it has a similar gradient signature to the

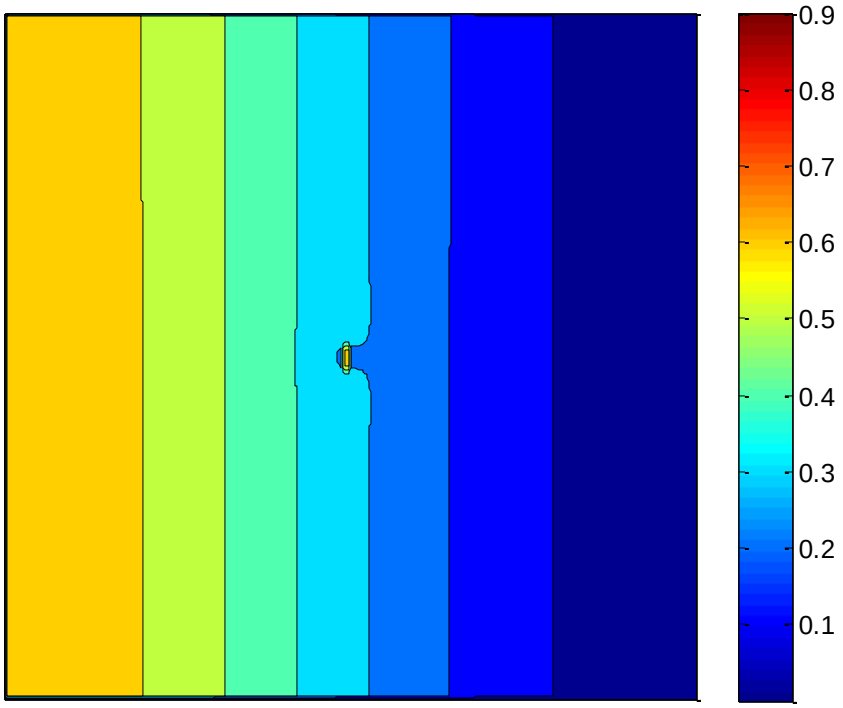

(a)

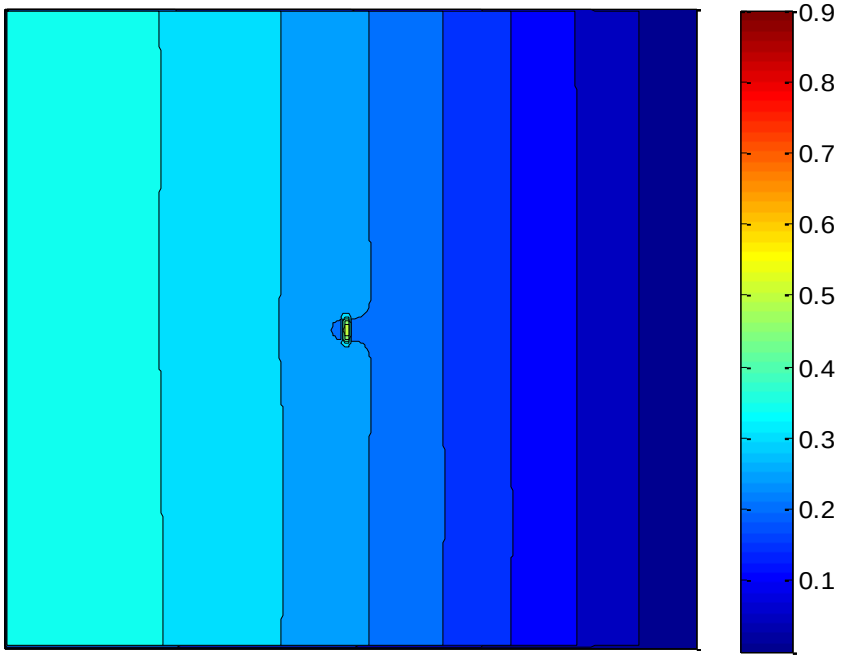

(b)

Fig 4.10 Images of Temperature Gradient for a 0.5-cm Longitudinal Crack, (a) at 10 seconds, (b) at 30 seconds.

2 cm longitudinal crack. One possible explanation for this similarity is due to the "frontal area" of the crack, or the visible area of the crack if one is viewing it from the same direction as the heat flux. In both cases the frontal area is approximately 2 cm, so in both cases the heat must travel the same distance around the crack.

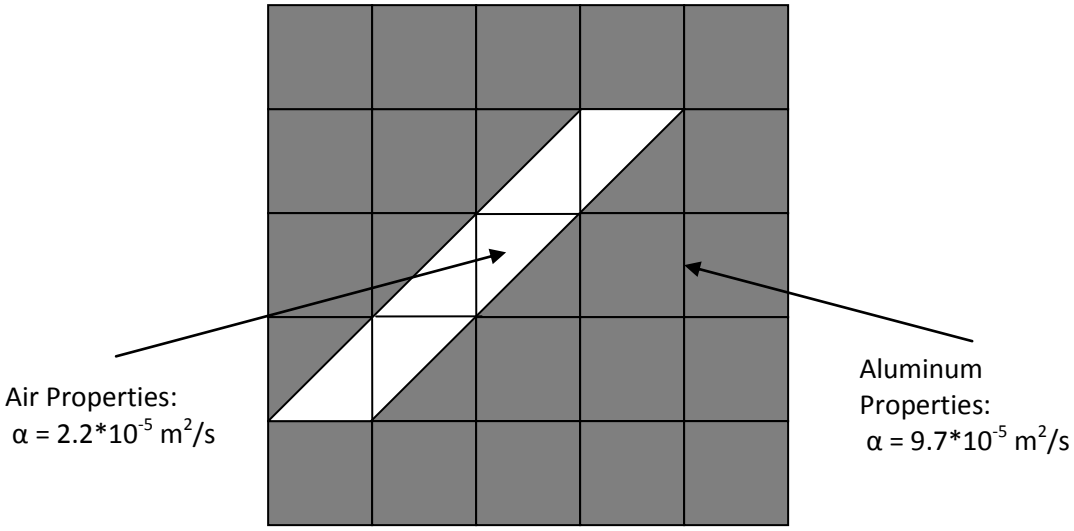

Fig 4.11 Numerical Grid Used for the Angled Crack Simulation.

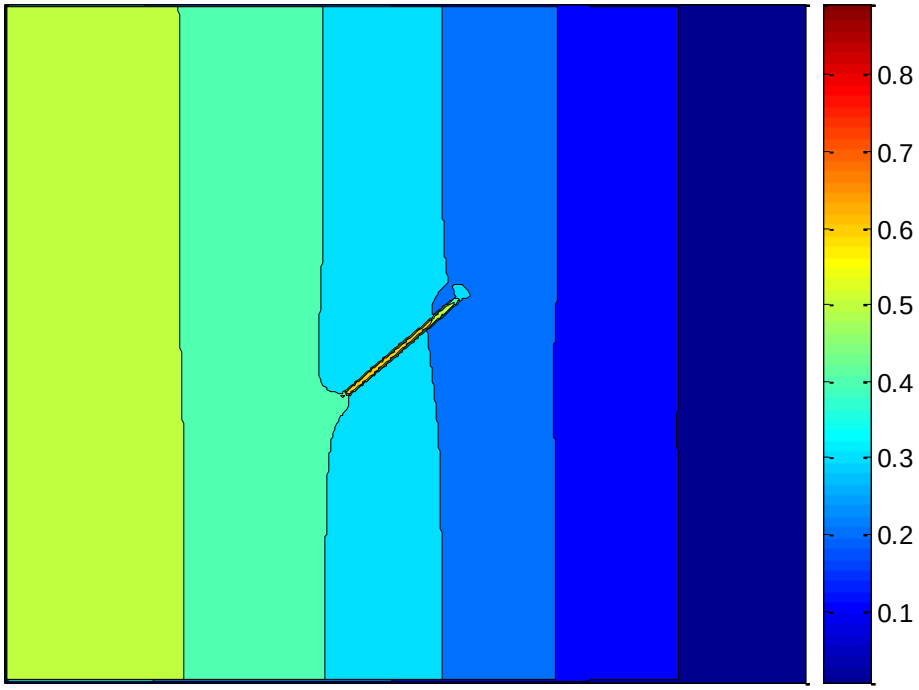

(a)

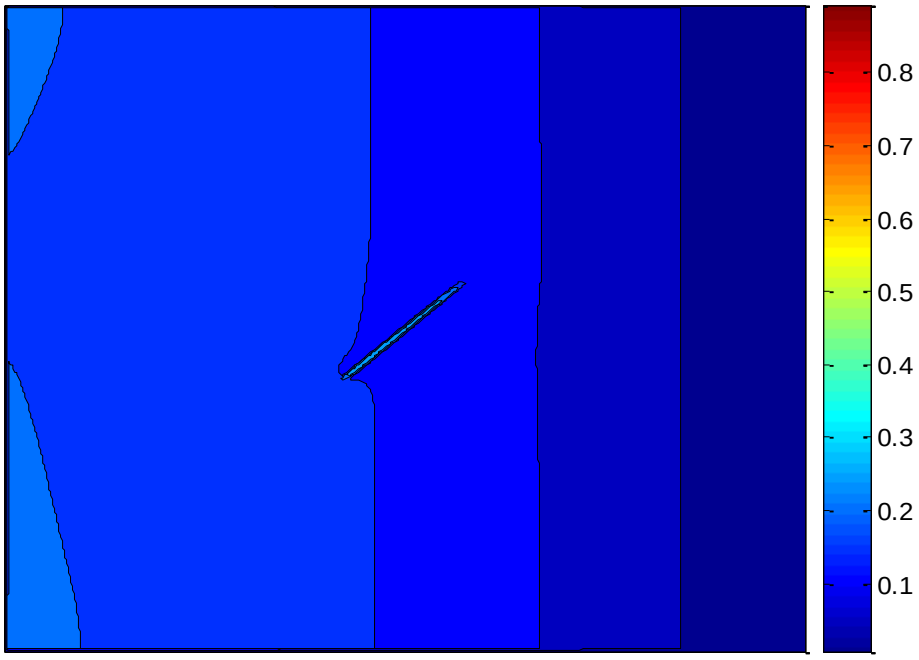

(b)

Fig 4.12 Images of Temperature Gradient for a 3-cm Angled Crack,

(a) at 15 seconds, (b) at 60 seconds.

d. Results – Effect of Thermal Conductivity on Crack Detection

While the results above are positive and verify previous experimental tests, it is conceivable that a material with a significantly lower emissivity could be analyzed as well. While it is certain that with lower thermophysical properties the heat will propagate slower and thus increase testing time, it is uncertain whether it will have an effect on defect detection resolution. Therefore, the model was modified to use a set of smaller thermophysical properties (similar to brass); the thermal conductivity used is approximately half that of the previous results. The results of the analysis are shown in Fig. 4.13.

Because of the lower thermal conductivity the crack isn't visible until later in the testing, in this case at 30 seconds. However, the crack is also visible for a longer period of time than before, with the crack still marginally visible at 120 seconds. Looking at the maximum gradient inside the crack, the lower conductivity reduced the maximum gradient by approximately one half. This means that while the crack will remain visible for a longer period, the amount of visibility is diminished. Since it has already been shown that reduction in crack size results in a smaller gradient as well, this shows that detection effectiveness decreases when the conductivity of the material is lowered.

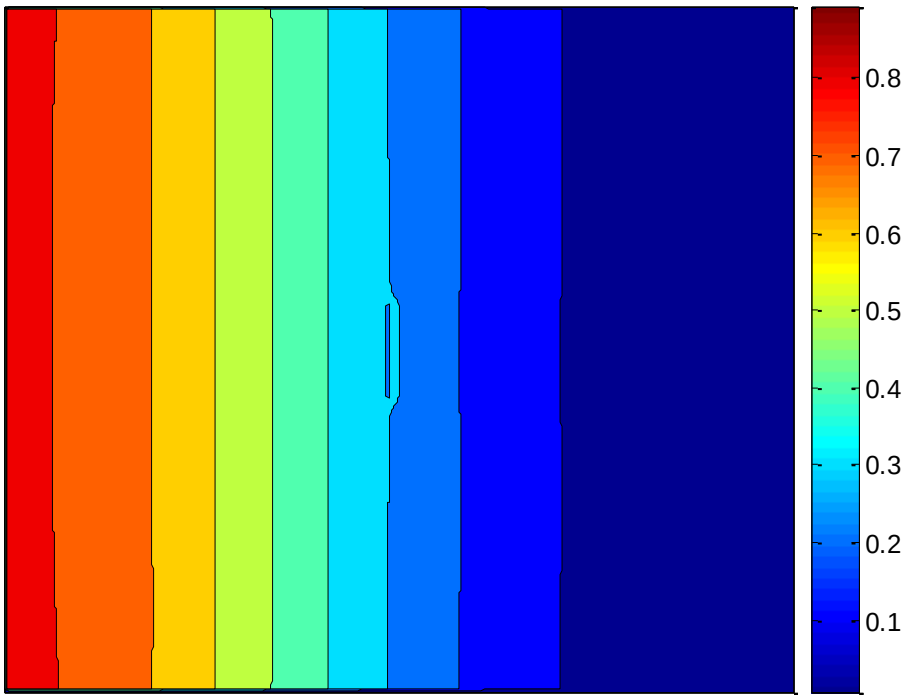

(a)

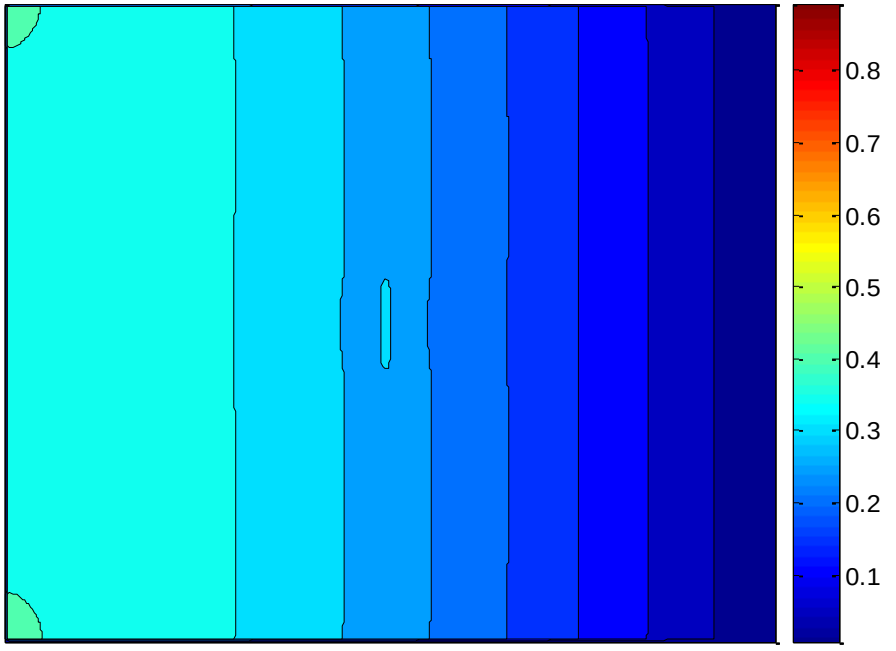

(b)

Fig 4.13 Images of Temperature Gradient for a 2-cm Crack with Lower Conductivity, (a) at 30 seconds, (b) at 120 seconds.

4.1.3 Three-Dimensional Transient Analysis

a. Model Development

To model more complex geometries such as reduction in cross-section or voids it is necessary to develop a three-dimensional model that adds thickness to the model. The program uses a similar explicit finite-difference method as the two-dimensional model previously discussed. If the material does not have internal heat generation, the equation for internal nodes can be simplified as:

$$T_{i,j,k}^{m+1} = T_{i,j,k}^{m} + \alpha\Delta t\left\{\begin{array}{l}\dfrac{T_{i+1,j,k}^{m} - 2T_{i,j,k}^{m} + T_{i-1,j,k}^{m}}{\Delta y^{2}} + \dfrac{T_{i,j+1,k}^{m} - 2T_{i,j,k}^{m} + T_{i,j-1,k}^{m}}{\Delta x^{2}} + \\ \dfrac{T_{i,j,k+1}^{m} - 2T_{i,j,k}^{m} + T_{i,j,k-1}^{m}}{\Delta z^{2}}\end{array}\right\} \tag{4.4}$$

All external boundaries are considered convective for this analysis, and an example boundary condition can be seen in Eq. (4.5).

$$T_{N,j,k}^{m+1} = T_{N,j,k}^{m} + \frac{\Delta t}{\rho c}\left\{\begin{array}{l}\dfrac{k}{\Delta x^{2}}\left(T_{N,j+1,k}^{m} - 2T_{N,j,k}^{m} + T_{N,j-1,k}^{m}\right) + \\ \dfrac{k}{\Delta z^{2}}\left(T_{N,j,k+1}^{m} - 2T_{N,j,k}^{m} + T_{N,j,k-1}^{m}\right) + \\ \dfrac{2k}{\Delta y^{2}}\left(T_{N-1,j,k}^{m} - T_{N,j,k}^{m}\right) - 2\dfrac{h}{\Delta y}\left(T_{N,j,k} - T_{\infty}\right)\end{array}\right\} \tag{4.5}$$

Again, these equations must be modified to allow for a change in geometry or composition. Since this program was written to evaluate defects larger than the grid size in every dimension, a different method of analysis was used. Voids within the sample will be considered as just a variation in conductivity to that of stagnant air; the only adjustment to the above derivation will be an adjustment for diffusivity for a selection of nodes within the sample. The heat flux is initiated from the upper left edge as a constant

temperature boundary condition. The images produced are of the upper surface of the sample.

b. Results – Center Void

The first three-dimensional defect analyzed will be a void in the center of the sample. The void has is a prism with dimensions of 3 cm in both length and width and 0.5 cm in thickness (4.5 cm^3 in volume), which is half of the total sample thickness. The results of the analysis can be seen in Fig. 4.14. The void is only marginally visible in the gradient image as a variation in the contours. The void is visible in this way for an extended period. Figure 4.14 is the surface profile after 30 seconds, and the subsequent images at 60 and 120 seconds have a similar profile.

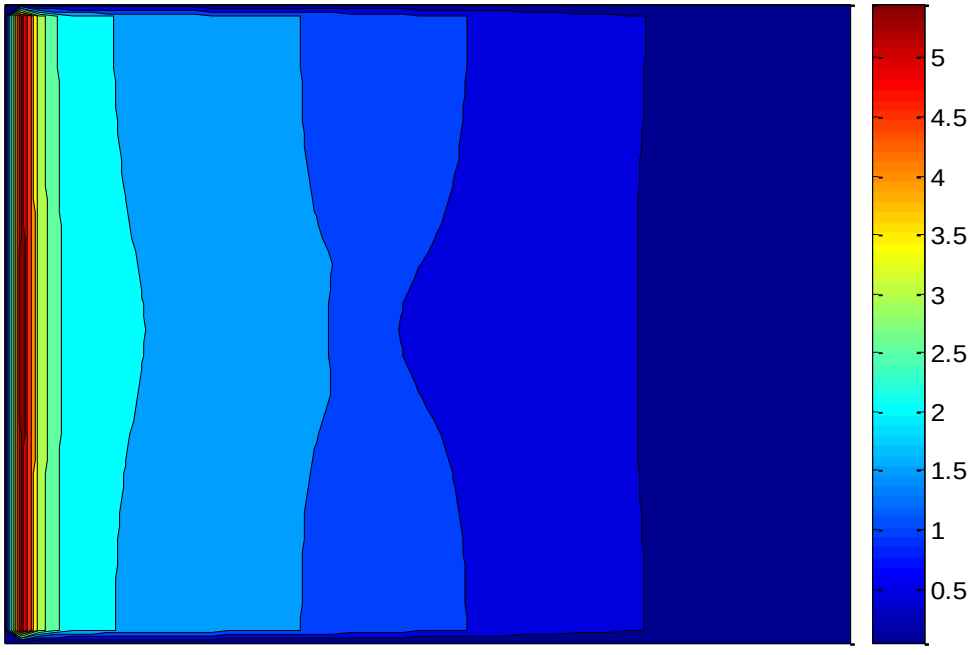

Fig. 4.14 Image of Surface Temperature Gradient for a 3-cm Center Void.

The next simulation analyzed is a larger void. The thickness remains the same, but the length and width of the void are increased to 5 cm (12.5 cm^3 in volume). The results of the analysis are shown in Fig. 4.15. The void is more visible than the previous size, but it is not as visible as the crack defects previously analyzed. Just like the previous void size the defect is visible for a prolonged period, from 30 to 120 seconds.

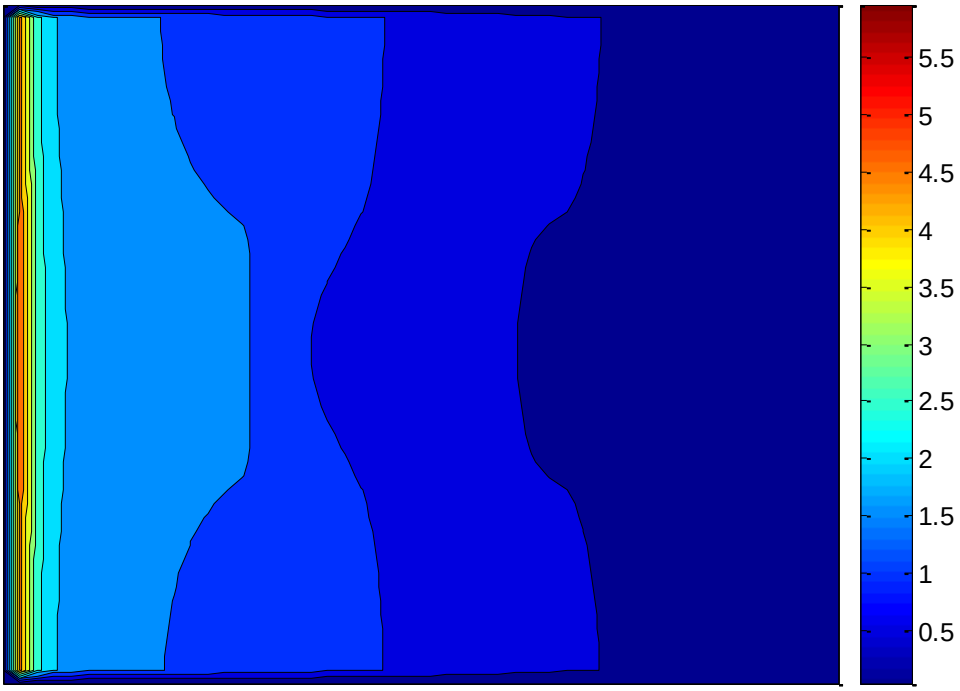

Fig. 4.15 Image of Surface Temperature Gradient for a 5-cm Center Void.

4.2 Radiative Heat Transfer

While it is important to understand and predict the conductive heat transfer occurring in each sample, it is perhaps more important to have a complete understanding of the radiative heat transfer, since this mode of heat transfer is the one recorded by the infrared camera. The goal of the radiative heat transfer simulation is to calculate the shape factor for the camera shroud and sample to determine the percentage of radiation emitted from the sample that is received by the camera.

4.2.1 Model Development

As previously mentioned, shape factor calculations have been developed for many types of geometric arrangements. First, one must determine the geometry of the camera shroud to determine which arrangements may be appropriate for use. Figure 4.16 shows a diagram illustrating the interior dimensions of the camera shroud (width of the shroud is uniform at 13.5 cm).

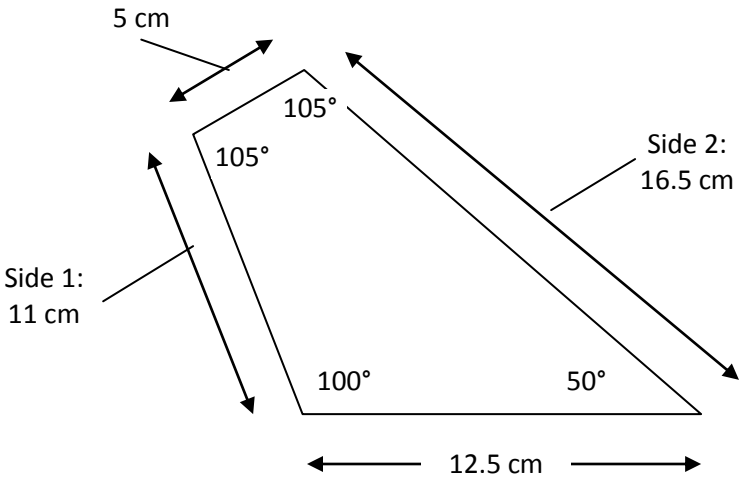

Fig. 4.16 Dimensions of Camera Shroud.

For the shroud itself, there are 4 shape factors to be calculated: the interaction between the 4 "sides" of the shroud and the top surface where the camera is located. The sides will be numbered to avoid confusion; the two sides not perpendicular with the top surface will be labeled as 1 and 2 (as shown in Fig. 4.16), and the two sides that are perpendicular to the top surface will be labeled as 3 and 4. Each set of sides will use a unique shape factor equation that has been previously developed and published in literature.

The non-perpendicular sides will use a relationship derived by Hamilton and Morgan [22] that quantifies the shape factor between a strip element and a rectangular plane intersecting at an angle. Figure 4.17 shows a diagram of the relationship between the two surfaces. The equation for these sides is given as follows:

$$F_{d1-2} = \frac{1}{\pi}\left\{\begin{array}{l} \tan^{-1} B + \dfrac{\sin^2\phi}{2B}\ln\left[\dfrac{X^2 + B^2}{(1+B^2)X^2}\right] - \dfrac{\sin 2\phi}{2B}\left[\dfrac{\pi}{2} - \phi + \tan^{-1}\left(\dfrac{C-\cos\phi}{\sin\phi}\right)\right] \\ + \dfrac{Y}{B}\left[\tan^{-1}\left(\dfrac{C-\cos\phi}{Y}\right) + \tan^{-1}\left(\dfrac{\cos\phi}{Y}\right)\right]\cos\phi + \dfrac{C\cos\phi - 1}{X}\tan^{-1}\left(\dfrac{B}{X}\right) \end{array}\right\} \quad (4.6)$$

B, C, X, and Y are all geometric ratios evaluated using the following equations:

$$B = \frac{b}{a} \quad (4.7)$$

$$C = \frac{c}{a} \quad (4.8)$$

$$X = \sqrt{C^2 - 2C\cos\phi + 1} \quad (4.9)$$

$$Y = \sqrt{B^2 + \sin^2\phi} \quad (4.10)$$

The parameters a, b, c, and Φ are from the geometry of the surfaces and can be seen in Fig. 4.17.

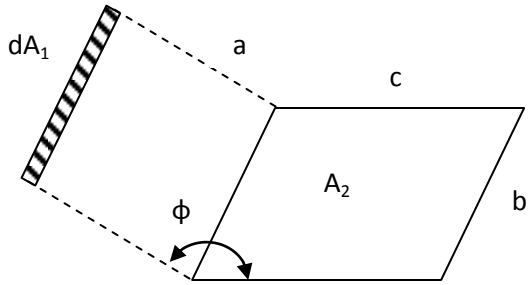

Fig. 4.17 Parameters in Shape Factor Calculation for Strip Element to Rectangular Plane.

The perpendicular sides will use a relationship from Hottel [23] that relates two finite rectangles of same length having a common edge, and a 90° angle between them. While the two perpendicular sides are not rectangles, this will provide a good approximation of the shape factor for the entire surface. A diagram of the two surfaces can be seen in Fig. 4.18. The equation that relates the two surfaces can be written as:

$$F_{1-2} = \frac{1}{W\pi}\left\{\begin{array}{l} W\tan^{-1}\frac{1}{W} + H\tan^{-1}\frac{1}{H} - \sqrt{H^2+W^2}\,\tan^{-1}\sqrt{\frac{1}{H^2+W^2}} \\ +\frac{1}{4}\ln\left(\frac{\left(1+W^2\right)\left(1+H^2\right)}{1+W^2+H^2}\right)\left[\frac{W^2\left(1+W^2+H^2\right)}{\left(1+W^2\right)\left(W^2+H^2\right)}\right]^{W^2}\left[\frac{H^2\left(1+W^2+H^2\right)}{\left(1+H^2\right)\left(W^2+H^2\right)}\right]^{H^2} \end{array}\right\} \quad (4.11)$$

H and W are parameters defined with the following equations:

$$H = \frac{h}{l} \quad (4.12)$$

$$W = \frac{w}{l} \quad (4.13)$$

The parameters h, w, and l are the dimensions of the two rectangles and can be seen in Fig. 4.18.

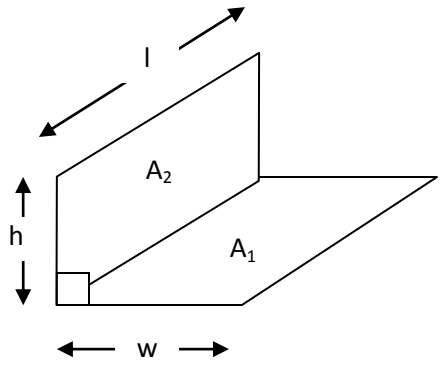

Fig. 4.18 Parameters in Shape Factor Calculation for Two Perpendicular Finite Rectangles.

The final relationship used is for the relationship between the top surface of the shroud and the bottom surface, which is typically the sample surface. The relationship used is the relationship between a differential element tilted at an arbitrary angle to a finite rectangle from Hollands [24]. A diagram of the relationship can be seen in Fig. 4.19. The equation used can be written as:

$$F_{d1-2} = \frac{1}{2\pi}\left[\begin{array}{l}\left(\tan^{-1} B\right)\cos\theta_i + \left(\tan^{-1} A\right)\cos\theta_j + \dfrac{A\cos\theta_k - \cos\theta_i}{\sqrt{1+A^2}}\tan^{-1}\left(\dfrac{B}{\sqrt{1+A^2}}\right) \\ + \dfrac{B\cos\theta_k - \cos\theta_j}{\sqrt{1+B^2}}\tan^{-1}\left(\dfrac{A}{\sqrt{1+B^2}}\right)\end{array}\right] \quad (4.14)$$

The parameters A and B can be written as:

$$A = \frac{a}{c} \quad (4.15)$$

$$B = \frac{b}{c} \quad (4.16)$$

The parameters a, b, θ_i, θ_j, and θ_k are geometric relationships and can be seen in Fig. 4.19. The angles are between the coordinate axes defined by the rectangle and the normal vector from the surface of the element.

The computational program written to handle these relationships is fairly simple; for the two relations that involve a differential element, the surface to be analyzed is divided into elements and each element is evaluated separately and combined to form the total shape factor for the surface using shape factor algebra. The output of the program is the shape factor values for each of the 4 sides of the shroud, as well as the surface of the sample. Once the shape factor values are produced, the total shape factor for the shroud can be found using the relationship:

$$F_{Total} = \frac{A_1 F_{1-T} + A_2 F_{2-T} + A_3 F_{3-T} + A_4 F_{4-T}}{A_1 + A_2 + A_3 + A_4} \tag{4.17}$$

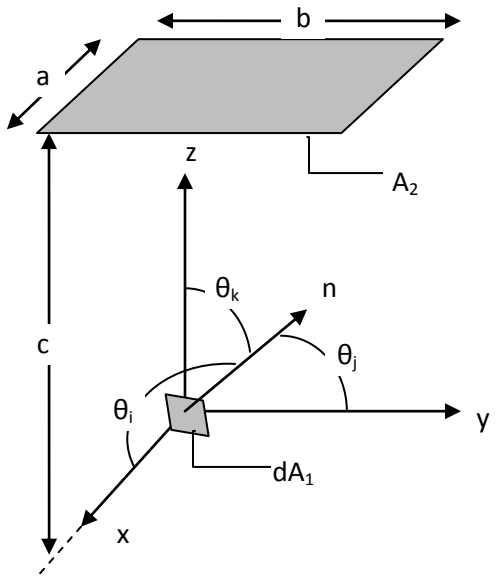

Fig. 4.19 Parameters in Shape Factor Calculation for Differential Element to Finite Rectangle.

4.2.2 Results

Table 4.1 shows the results of the computational program to determine shape factor. All 4 sides of the camera shroud contribute very little radiation to the top surface; this is somewhat expected because the surfaces are at perpendicular or oblique angles to the surface. It can be said that the camera shroud does not significantly alter the radiation signature of the surface. It is surprising to note the value for shape factor for the sample surface, which is less than 6 percent. If you consider that the top surface of the camera is much smaller than the sample surface, and that the radiation is being treated as diffuse and being emitted in every direction, this also is not unexpected. In fact, the infrared camera takes this scattering effect into account when the images are analyzed [20]. These results are significant in that it appears there are no large effects in terms of radiation from the shield that are not currently quantified. With a sample that is uniformly diffuse, the system should be able to analyze the emissivity correctly and calculate the true temperature of the surface.

Table 4.1 Shape Factors of Camera Shroud

Configuration	Shape Factor Value
Side 1 to top: $F_{1\text{-}T}$	0.0943
Side 2 to top: $F_{2\text{-}T}$	0.0718
Side 3 to top: $F_{3\text{-}T}$	0.139
Side 4 to top: $F_{4\text{-}T}$	0.139
Camera Shroud: $F_{S\text{-}T}$	0.0956
Sample Surface to top: $F_{5\text{-}T}$	0.0590

4.3 Automation Considerations

While the system has proven successful in several instances, it is still lacking in that it is not a true scanning system, where the heat source and camera scan across the material and calculate values simultaneously. While creating the hardware to make the system autonomous would not be a difficult problem, the issue that presents the most challenges is revising the method of detection. As discussed in Chapter 2, once the heat source begins to move, the temperature gradient function is changed dramatically which has a huge effect on the system's ability to detect defects. Therefore, considerations must be made to determine how the system would operate in a scanning environment: how would data be collected and analyzed, how would the existing analysis be altered, and how would the ability to detect a variety of defects be improved or diminished.

4.3.1 Collection of Data

Since the system will no longer be stationary it's important to determine how it would be possible to calculate the set of values necessary to perform the removal of reflected radiation. The requirement for the current analysis is using a cold image to calculate the emissivity which is in turn used to calculate the corrected temperature. However, with a moving heat source and camera, the area of the sample viewed by the camera will always have a temperature gradient of some type. Therefore, in order to use the same method of analysis, the scanning velocity must be adjusted so that the temperature at the far edge of the sample is still at the initial temperature.

A similar process of analysis can be used by analyzing portions of the image separately while the camera is in motion. First, the portion of the image the farthest away from the heat source that is still at the initial temperature can be used to measure

emissivity. If even only 10-15% of the image is used for emissivity calculations that will still allow for approximately 25-40 pixels to obtain an average emissivity value for a particular point. Figure 4.20 shows a diagram of how the analysis could potentially be used. The remainder of the sample can now be corrected using the analysis listed in Chapter 3.

4.3.2 Modification of Gradient Analysis

After correction of the temperature image, the gradient would now be calculated to search for defects. However, with a moving heat source and camera, the image will

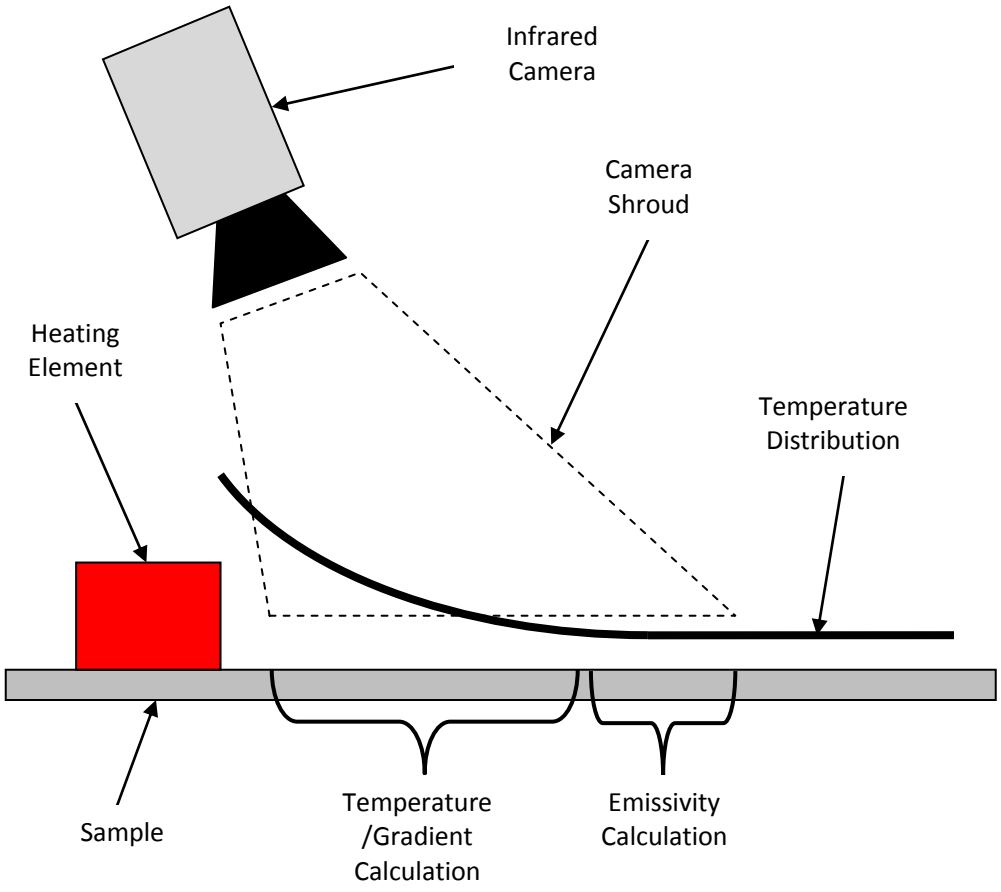

Fig. 4.20 Diagram of Scanning Analysis.

have a constant gradient, particularly near the heat source. In this case, a high gradient due to a defect may go unnoticed with the traditional analysis. In order to correct this issue, a different type of calculation may be performed that could be used instead of the gradient calculation.

As previously discussed in Chapter 2, the temperature distribution in a scanning system is dependent only on the diffusivity of the material as well as the scanning velocity. In this case, if both values are known during analysis, the temperature distribution will be well known in a uniform material. A defect present in the material would alter the temperature distribution such that the difference between the new temperature distribution and the uniform material distribution would be noticeable, especially as the temperature gradient increases closer to the heat source. Figure 4.21 shows a diagram demonstrating the potential detection of a defect. The two profiles could be subtracted from one another and any large differences could be checked for defects.

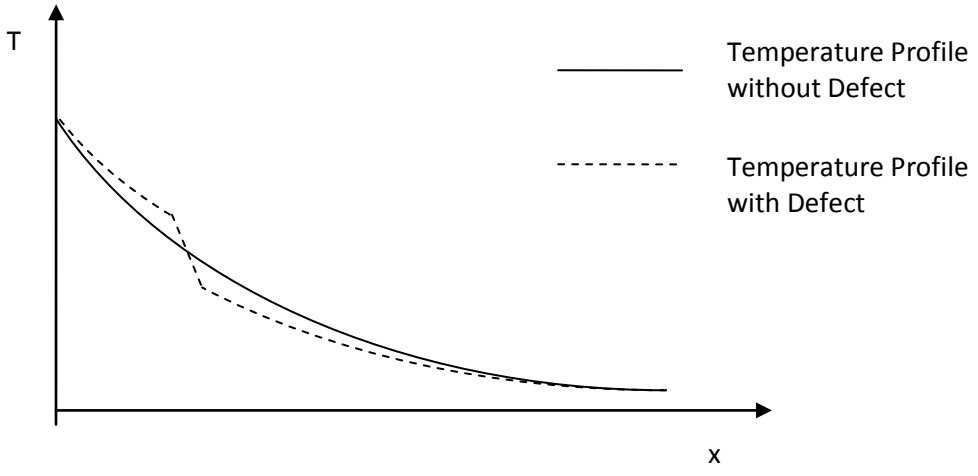

Fig. 4.21 Scanning Temperature Profiles.

4.3.3 Defect Detectability

In the scanning system, crack defects and other similar defects that significantly block the flow of heat should be easily detected using the method described in the previous sections. However, subsurface defects such as delaminations and thin voids could potentially be visible with some alterations to the system. In a method similar to flash diffusivity, the camera could trail the heat source instead of leading it and record the results of the heat penetrating into the material. Much like flash diffusivity, the camera could be adjusted in terms of position so that a longer time period elapses between the heat source passing over the sample and when the camera views the area of heating. If there are defects present in the depth of the material, the heat will reflect off and return to the surface resulting in an elevated surface temperature. In this case, with each scan, the system would only be able to detect defects in a small section of the depth, and would need to be repeated in order to analyze the entire thickness.

To maximize the potential of a system such as this, it would be beneficial to have two infrared cameras: one leading the heat source and the other trailing. This would allow for detection of both crack-type defects and subsurface defects. While this may be cost prohibitive at this point, with the continued decline in cost of equipment there may come a time when the cost of time spent rescanning sections could outweigh the cost of an additional camera.

CHAPTER FIVE

EXPERIMENTAL TESTING

The previous study [21] has been focused primarily on crack defects present in thin metal sheets. The tests yielded some promising results, but it was shown that the previous iteration of the system was only marginally successful at removing reflected radiation from variable emissivity surfaces. It will first be determined whether the improvements in the system's hardware have improved its ability to remove reflected radiation. Second, in the event that in certain circumstances reflected radiation removal proves too difficult (for example very low emissivity polished surfaces), a series of coatings will be evaluated based on their ease of application and removal, emissivity, and cost. Finally, the system will be used to analyze a new set of non-metallic materials: an epoxy resin sample and a carbon fiber/epoxy composite.

5.1 Improvements in Reflected Radiation

Several sheet metal samples that have been previously tested have been re-evaluated to determine whether improvements in the system's hardware have improved its ability to remove reflected radiation from the data and produce accurate thermographic images. Two samples will be re-evaluated: a sample coated with both black and white paint, and a sample with a paint barrier directly over a crack defect.

5.1.1 Results – Black and White Paint

Figure 5.1 shows a 1/32" steel sheet metal sample coated with both black and white paint. In previous tests [21], the system was unable to completely eliminate the effects of the difference in paints due to the non-uniformity of the shield temperature.

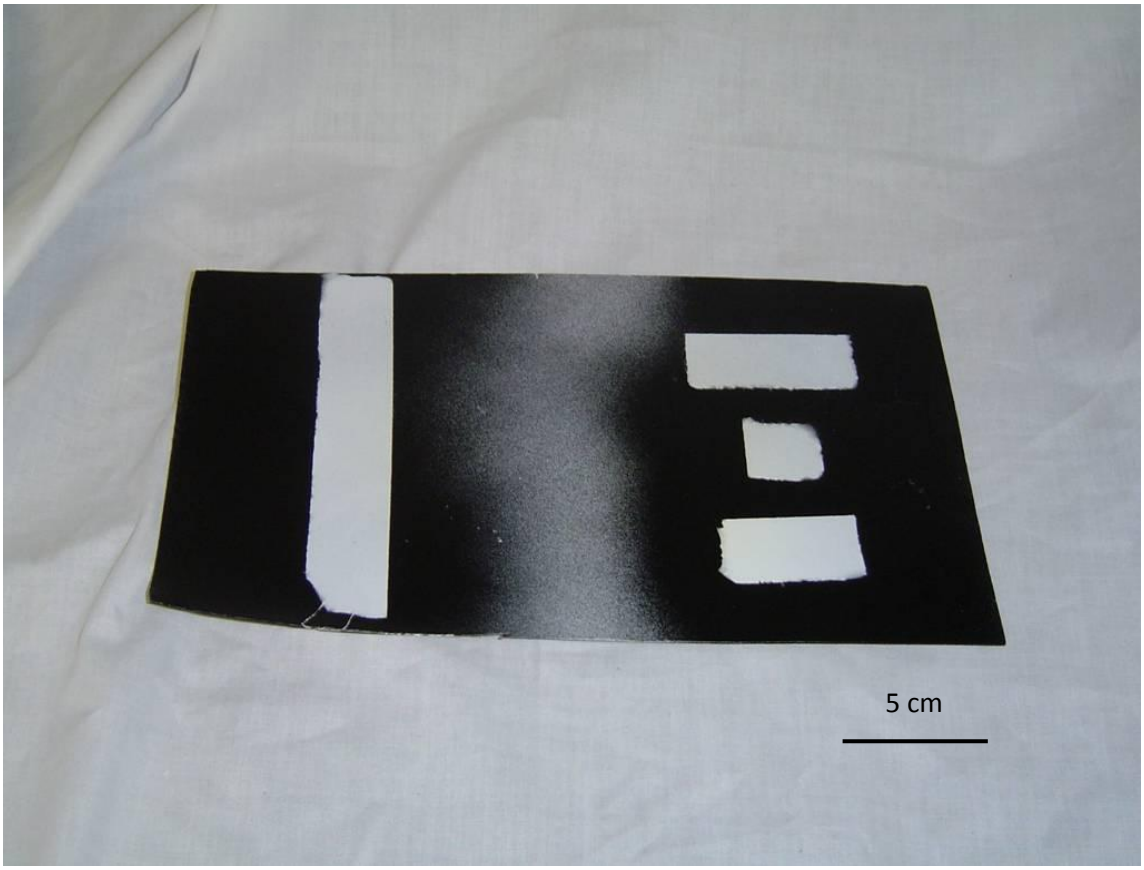

Fig. 5.1 Sheet Metal with Variable Emissivity Due to Coating.

The emissivity of the sample is shown in Fig. 5.2. Just like the previous test [21], the emissivity values are high for the entire surface, varying from 0.72 to 0.94. Figures 5.3 and 5.4 show the images of raw temperature and corrected temperature, respectively. The effects of variable emissivity appear to be completely removed in the corrected temperature image, where only the temperature change due to the heating is visible. Therefore, it appears that the system has improved in its ability to remove reflected radiation for surfaces that are diffuse in nature.

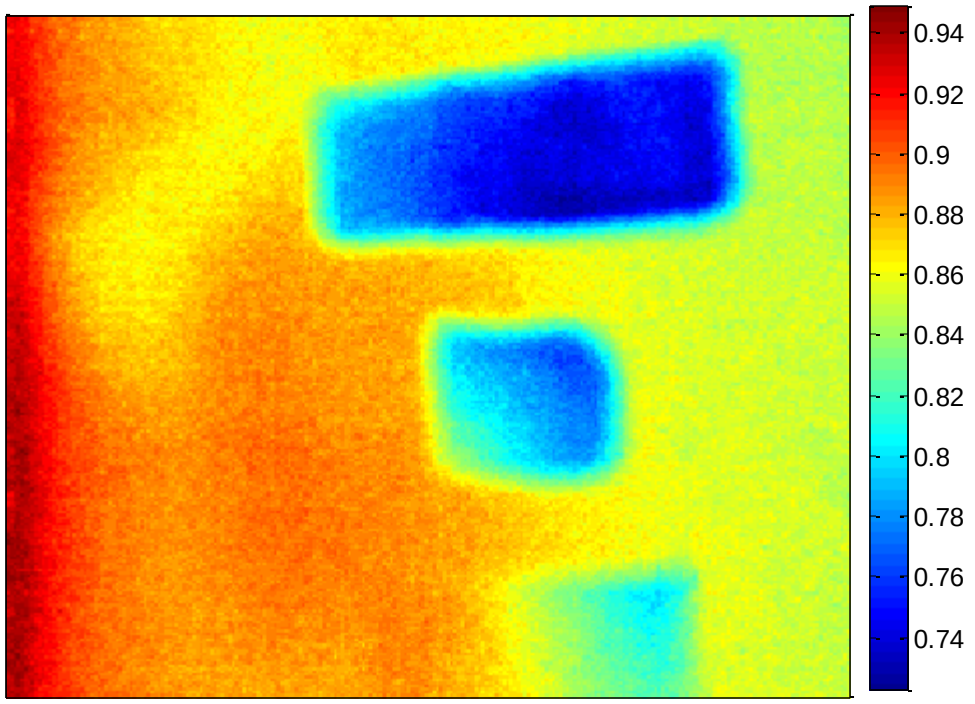

Fig. 5.2 Emissivity of Black/White Paint Sample.

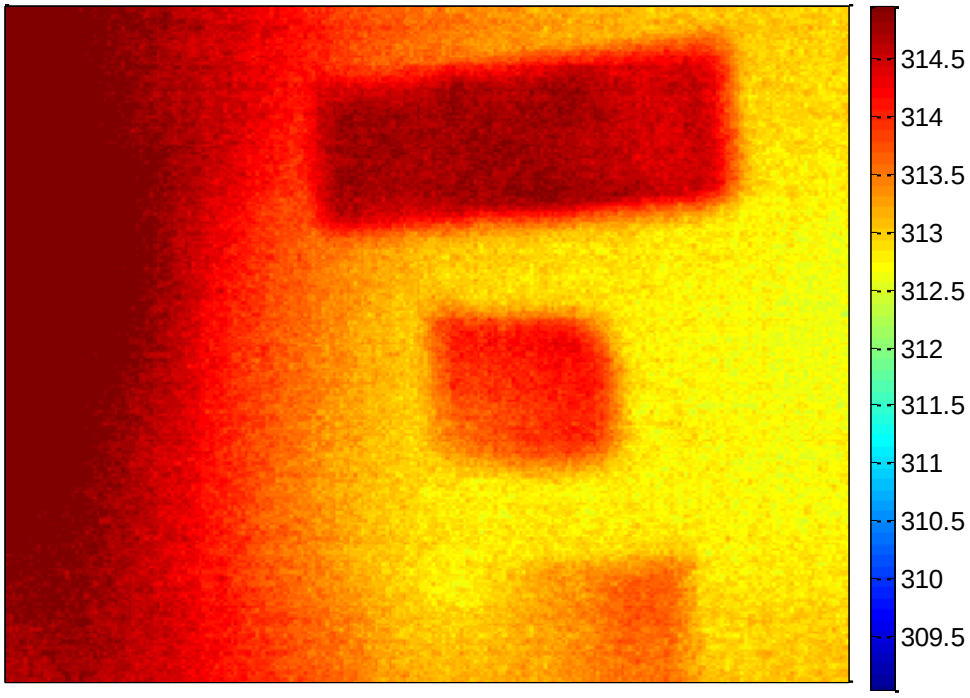

Fig. 5.3 Raw Temperature of Black/White Paint Sample.

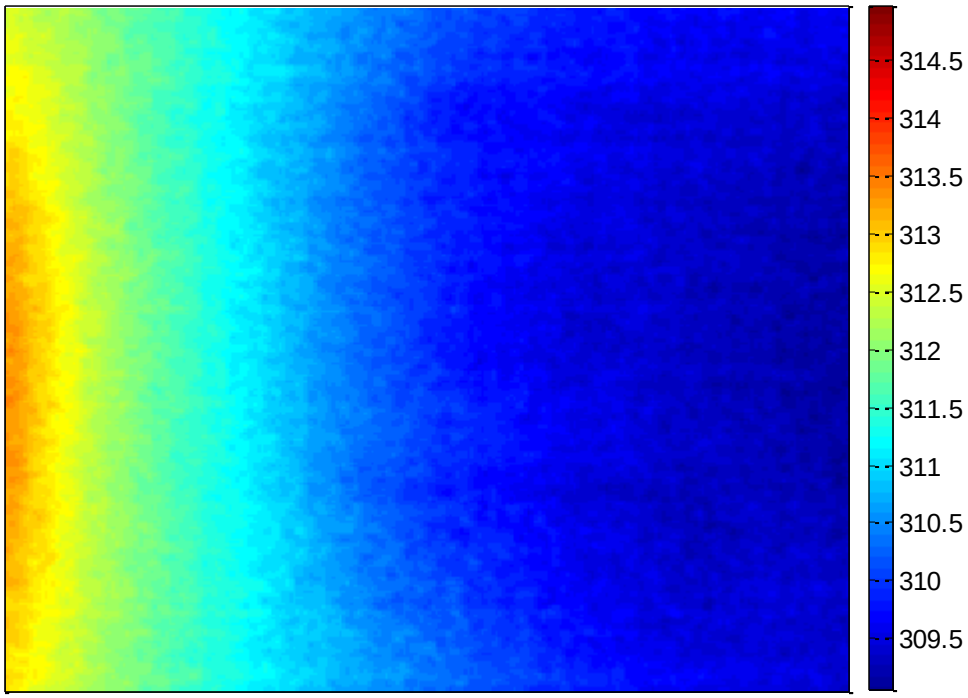

Fig. 5.4 Corrected Temperature of Black/White Paint Sample.

5.1.2 Results – Crack on Paint Barrier

Figure 5.5 shows the second sample to be tested: a 1/32" steel sample with a 3 cm crack at the interface between the painted surface and bare metal. In the previous tests [21], the system was unable to differentiate between the actual defect and the paint/bare metal barrier. There has been one small edition to the sample – part of the unpainted section has been coated with a clear cement. Figure 5.6 shows the emissivity image of the sample; the center section appears as a significantly lower emissivity as the rest. The portion coated with the clear cement raised the emissivity slightly, but the section still has an emissivity significantly lower than the painted portion of the sample.

Figures 5.7 and 5.8 show the raw and corrected temperature images of the sample. It is expected that the raw temperature image will show incorrect temperature portions,

but the corrected temperature image also shows a large amount of anomalies. Figure 5.9 shows the gradient image of sample; one area of higher gradient is directly over the crack location, but there is a similar portion of higher gradient visible in the image where the other side of the paint barrier is located. While it appears that the program can successfully analyze surfaces with variable emissivity that are uniformly diffuse, the equations that govern the system break down with surfaces that are highly specular.

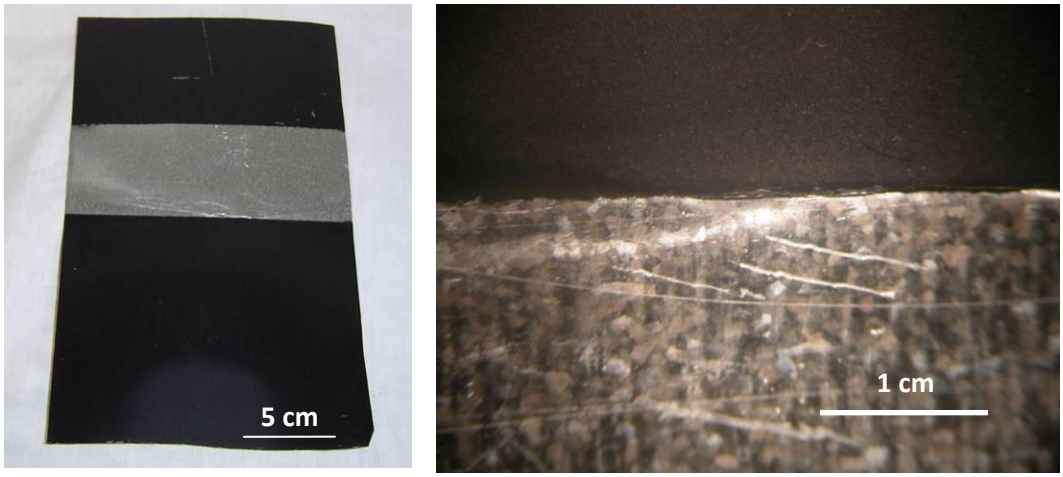

(a) (b)

Fig. 5.5 Sample with Crack on Paint Barrier, (a) Full Image of Sample, (b) Close-up View of Crack.

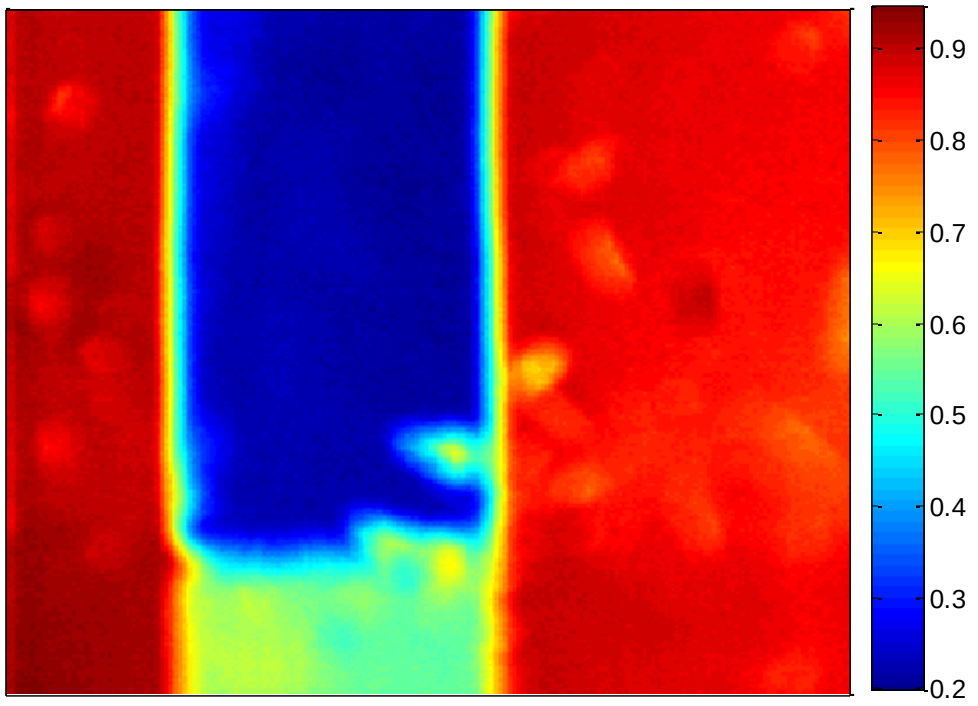

Fig. 5.6 Emissivity of Bare Metal/Paint Sample.

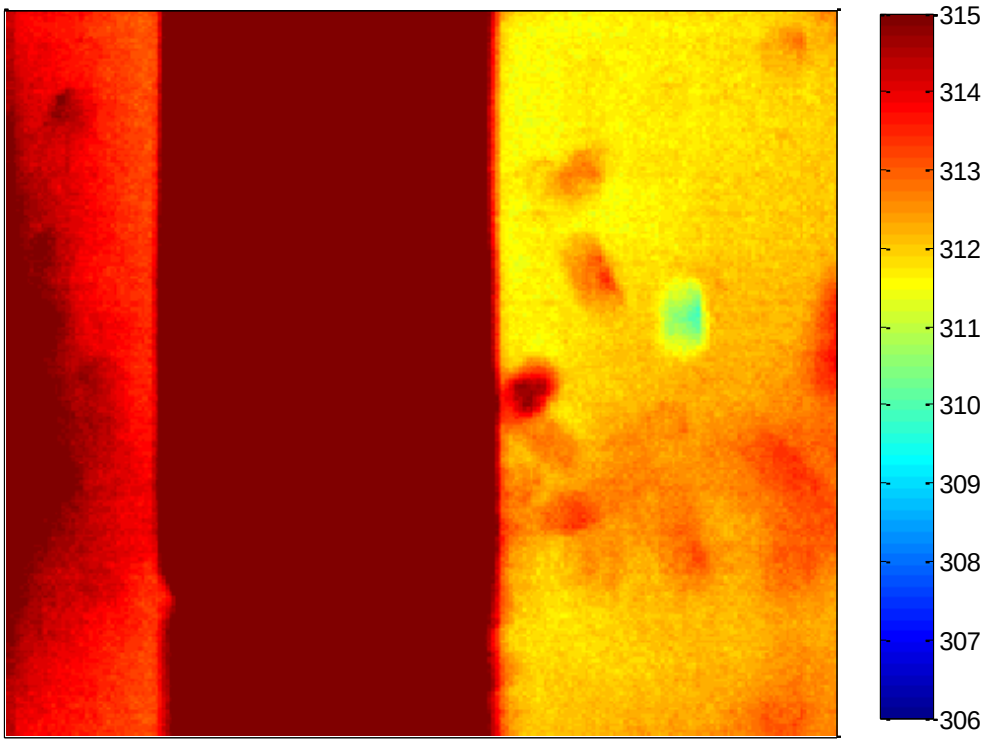

Fig. 5.7 Raw Temperature of Bare Metal/Paint Sample.

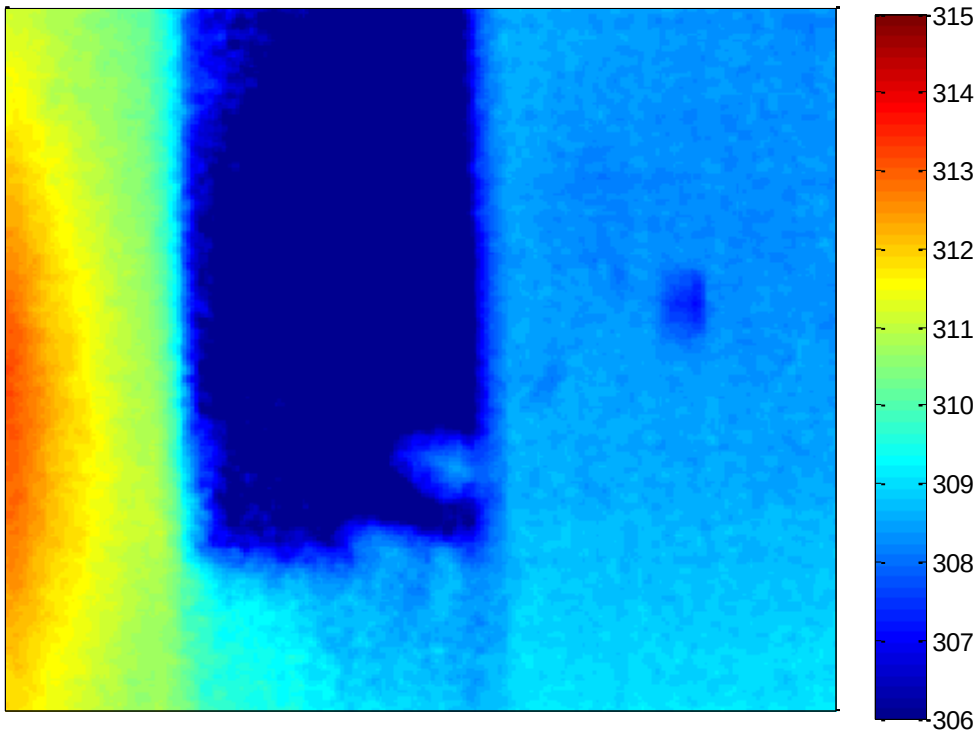

Fig. 5.8 Corrected Temperature of Bare Metal/Paint Sample.

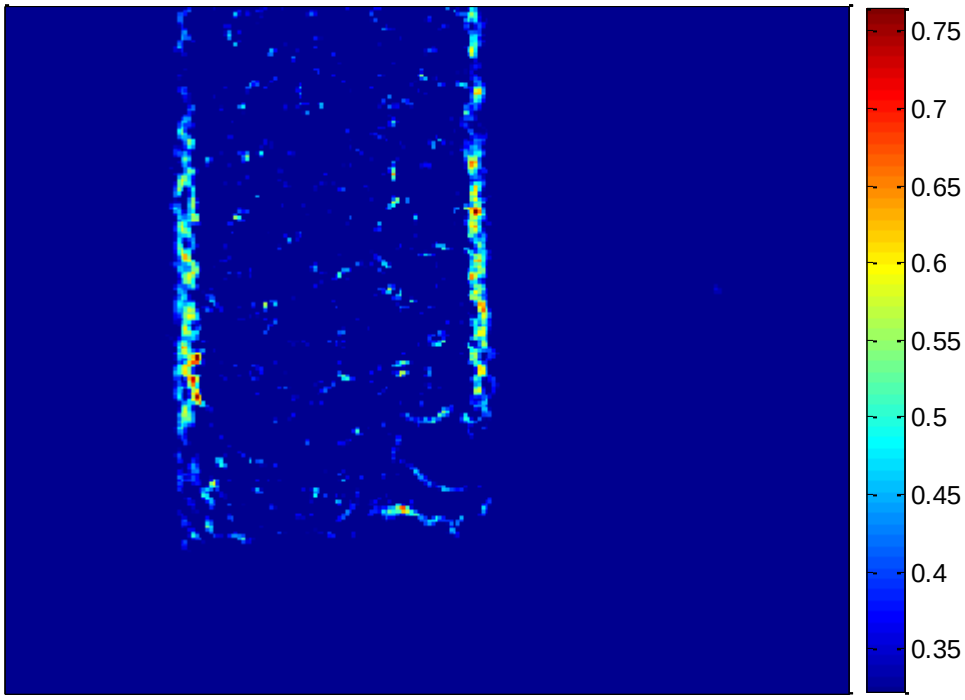

Fig. 5.9 Temperature Gradient of Bare Metal/Paint Sample.

5.2 Coating Analysis

Despite the many successes of the current system, samples with low emissivity still prove difficult to analyze. The radiation analysis for the system is limited in its ability to handle samples with a high degree of specularity, such as a highly polished metal. Therefore, in such cases, it may be preferable to utilize a simple coating during analysis to raise the emissivity, produce a more diffuse surface, and produce meaningful temperature results. The coatings in question should be easily applied and removed, and have a relatively low cost. The series of coatings selected for this analysis were commercially available water-based tempera paints. Because the coatings are water-based, they are easily removed with water, even after complete drying. The coatings were made by combining a measured amount of paint by weight and mixing it with water at the desired amount of weight. The coatings were applied by mixing the appropriate ratio, pouring a measured amount on the sample, and holding the sample vertically to allow the paint to spread, thus allowing for a uniform coating with no variations due to brushes or other applicators. A variety of colors were selected for analysis, as well as a series of water-to-paint ratios. The emissivities of each sample were calculated using the initial portion of the LabView program.

5.2.1 Color Analysis

First, a series of colors were selected to determine whether the color of the paint would have a significant effect on improving the emissivity. Since each color absorbs and emits different wavelengths of energy, it is probable that these colors would also have an effect on emissivity of the surface. Five colors were selected for analysis: red, blue, green, black and white. Each was mixed in a 1-to-1 ratio with water and applied to

an aluminum sample. The initial emissivity of the bare surface was calculated as 0.25. The results of the analysis can be seen in Table 5.1.

The results produced some interesting findings. All the paint colors produced a dramatic increase in emissivity, with black producing the highest emissivity of 0.879. However, the remaining colors all increased the surface emissivity to above 0.8, which is excellent for analysis of this type. This set of emissivity values agrees fairly well with published values that list the range of emissivities for enamel paints between 0.876 and 0.90 [19]. The blue, green and red values reveal no distinct trend between each other and all have emissivities between 0.855 and 0.865. Therefore, outside of black and white it is believed that color has no dramatic effect on the emissivity of the surface. It is advised that any coating used be black or darker in color, but it appears that any color coating will be acceptable for the goal of improving emissivity.

5.2.2 Water/Paint Ratios

After determining the effect of color on modifying emissivity, the next step is to determine whether reducing the amount of paint used will have a detrimental effect on the surface emissivity. It is hypothesized that increasing the water-to-paint ratio (thereby decreasing the amount of paint in the coating) will reduce the emissivity, but the values will still be acceptable to use for the scanning system. A set of 3 ratios will be tested using the green paint: 3-to-1, 2-to-1 and 1-to-1. Tables 5.2, 5.3, and 5.4 show the results of the testing.

As expected, the emissivity decreases a large amount with increasing ratio. This can be explained by viewing the samples directly (shown in Fig. 5.10); the coatings become slightly translucent as the ratio increases, which allows the metal surface below

to be somewhat visible. While this reduces the emissivity dramatically, the coating does still decrease the specularity of the sample, which in turn should lead to improved analysis ability. While it may appear that an even higher ratio could be even more cost effective, the continuing decrease and emissivity as well as difficulty producing a uniform coating at lower ratios makes it less attractive. Therefore, it is proposed that for this type of coating, a 3-to-1 water-to-paint ratio could be used effectively to both increase the emissivity of the surface and reduce the cost of applying said coating.

Table 5.1 – Emissivities of Various Color Coatings

Color	**Emissivity**
Black	0.879
Blue	0.861
Green	0.864
Red	0.858
White	0.833

Table 5.2 – Emissivities of Green Paint with Various Water/Paint Ratios

Ratio	**Emissivity**
1-to-1 (50% paint)	0.87
2-to-1 (33% paint)	0.71
3-to-1 (25% paint)	0.54

Table 5.3 – Emissivities of Black Paint with Various Water/Paint Ratios

Ratio	**Emissivity**
1-to-1 (50% paint)	0.88
2-to-1 (33% paint)	0.83
3-to-1 (25% paint)	0.76

Table 5.4 – Emissivities of White Paint with Various Water/Paint Ratios

Ratio	Emissivity
1-to-1 (50% paint)	0.83
2-to-1 (33% paint)	0.80
3-to-1 (25% paint)	0.75

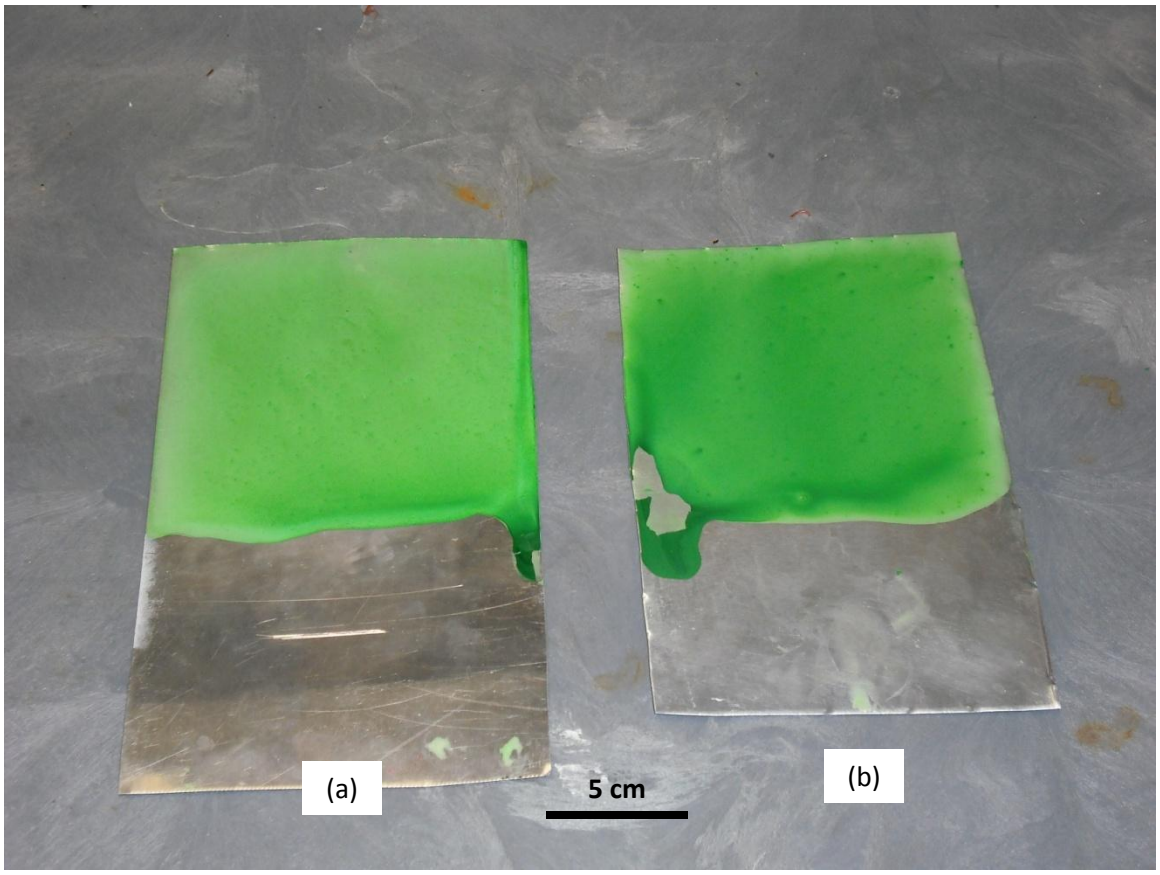

Fig. 5.10 Example of Coating Samples, (a) 3-to-1 Water/Paint Ratio, (b) 2-to-1 Water/Paint Ratio.

5.2.3 Coating Test

Since samples with a specular surface have proven difficult to analyze, a test was performed to determine whether a coating would be successful at locating defects in a partially specular surface. The sample used is the steel sample tested in section 5.1.2, where a crack defect is located directly below the barrier between paint and bare metal.

The previous test was unable to successfully locate the defect due to the specular nature of a portion of the sample. The sample was coated with a green paint mixture, with a 2-to-1 water-to-paint ratio. Figure 5.11 shows the results of the coating; while the surface did not produce an even coating due to residue from previous coating attempts, the coating adhered well enough to provide the opportunity for testing.

Figure 5.12 shows the emissivity map of the coated sample. The emissivity ranges from 0.78 to 0.89, which is a vast improvement from the previous range shown in Fig. 5.6, which has a minimum near 0.2. Figure 5.13 shows the corrected temperature image of the sample, and again there is a dramatic improvement in the image; while before there were large temperature anomalies present in the image, the new image of the coated sample displays a much more smooth temperature distribution, which is what is expected in the test. Finally, Fig. 5.14 shows the gradient image of the sample, which reveals two large gradient anomalies in the lower left quadrant of the image. While the upper of the two anomalies is most likely again due to a variation in the coating, the lower anomaly is at the location of the defect. Therefore, it is proposed that for specular or partially specular surfaces, a coating can be applied to improve the emissivity of the sample and successfully locate defects within.

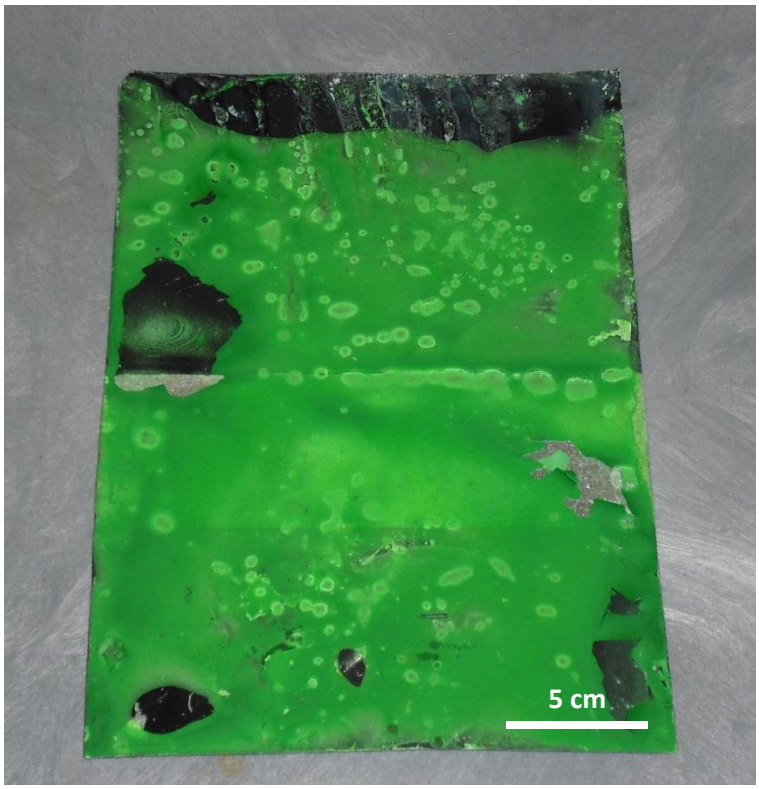

Fig. 5.11 Coated Bare Metal/Paint Sample.

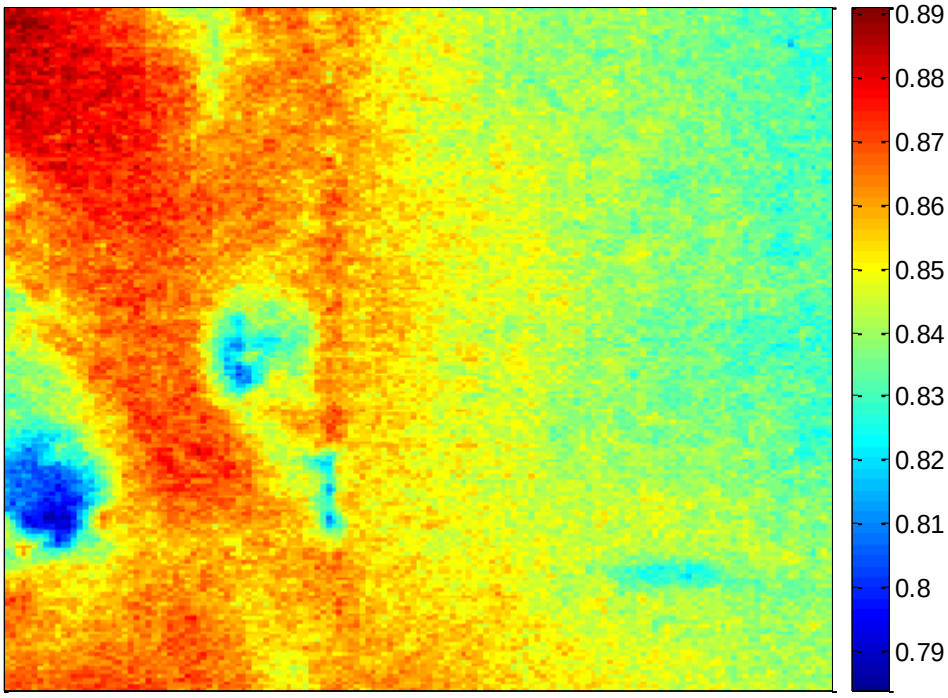

Fig. 5.12 Emissivity of Coated Bare Metal/Paint Sample.

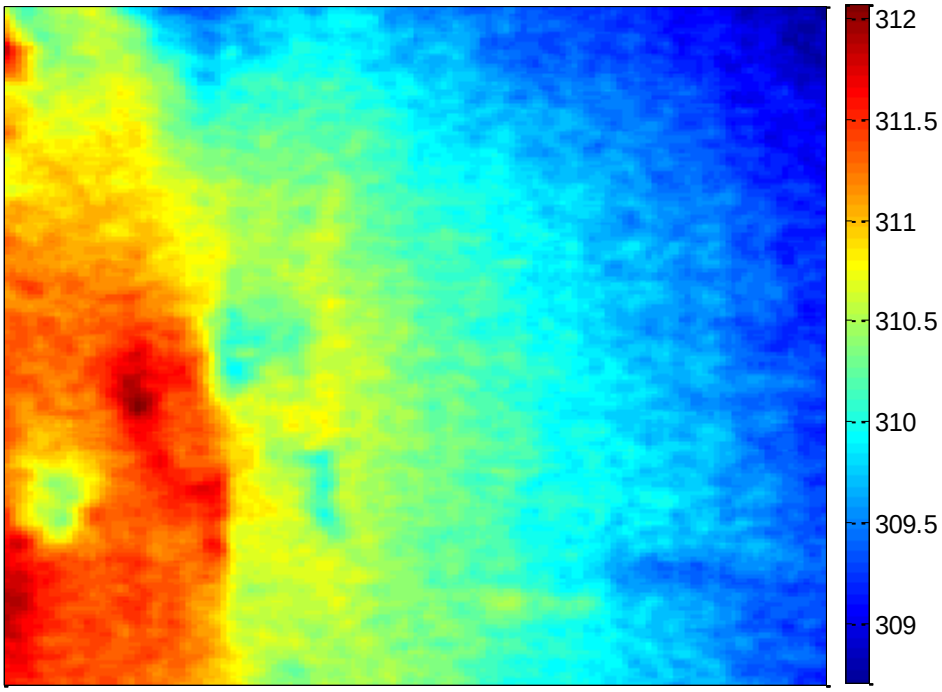

Fig. 5.13 Corrected Temperature of Coated Bare Metal/Paint Sample.

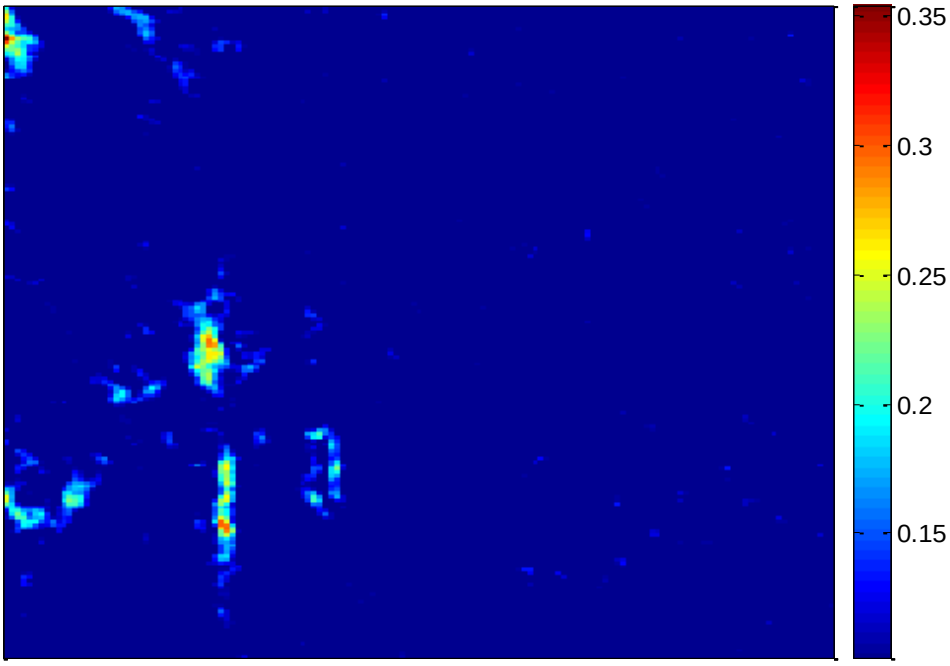

Fig. 5.14 Temperature Gradient of Coated Bare Metal/Paint Sample.

5.3 Testing of Non-metallic samples

The system has proved to be very accurate when analyzing metal samples with a high emissivity, non-specular surface. However, it is desired to expand the capability of the system to include non-metallic materials, in particular composites and other materials that are used in a structural capacity. The computational models presented in Chapter 4 verify the ability of the system to be used in such a way, provided the time is allotted for the heat to permeate through the sample due to a lower thermal conductivity. So, a series of tests have been performed to determine if the current iteration of the system can successfully analyze non-metallic samples. Two sets of samples were analyzed, one set composed primarily of epoxy resin with various internal defects, and the other a pair of carbon-fiber/epoxy resin composites.

5.3.1 Epoxy Resin Sample

Figure 5.15 shows an image of the epoxy resin sample. The bulk material is epoxy resin and was cured in a mold to produce a sample approximately 10 cm in width, 14 cm in length, and 1.5 cm in thickness. Inside the sample were several objects intended to modify the internal structure similar to that of a potential defect. Two sets of spherical objects were selected to simulate voids of varying thermal conductivities; plastic beads (4 and 5 mm in diameter) were used to simulate an air void, while lead fishing weights (approx. 6 mm in diameter) were used to simulate a higher conductivity void, such as what might be experienced with water or another fluid. On the opposite side of the sample, two planar materials were inserted into the sample to simulate a potential planar defect, such as delamination; a piece of aluminum (3 cm by 3 cm with 0.5 mm thickness) and a piece of dense foam (3 cm by 3 cm with 2 mm thickness) were used for this

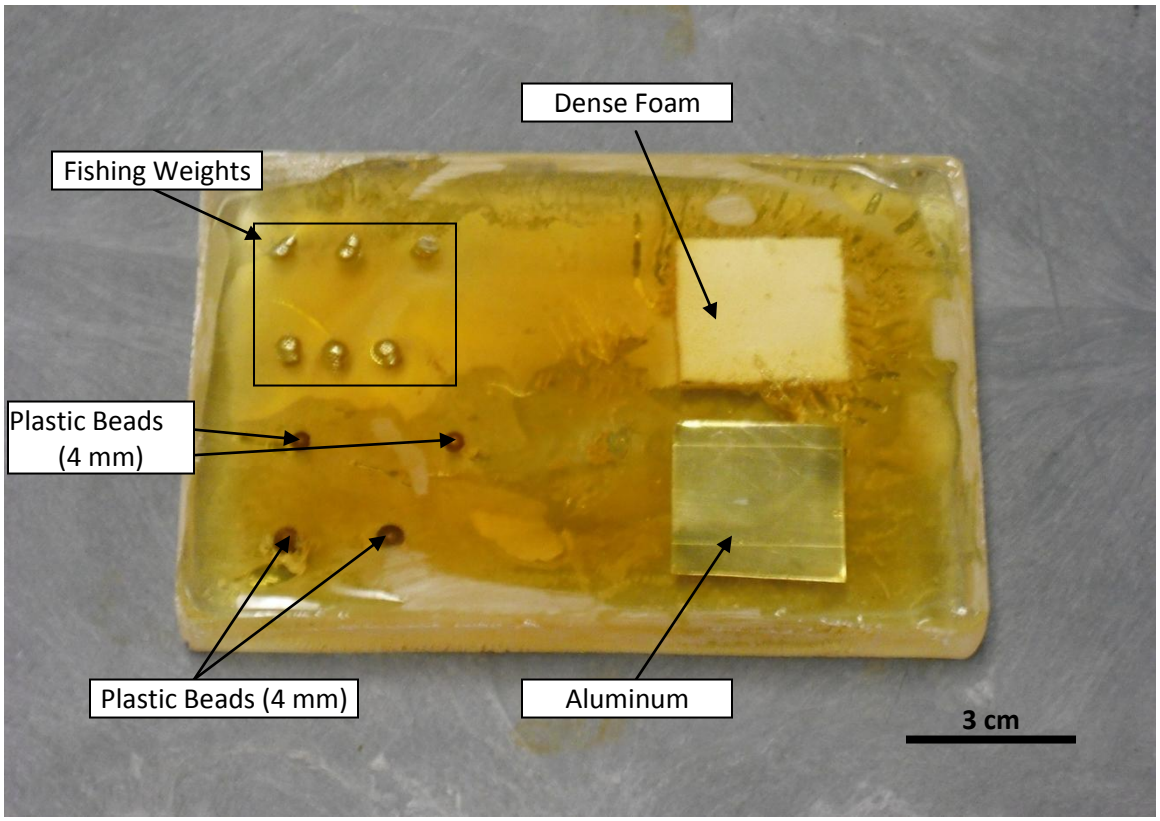

Fig. 5.15 Sample of Epoxy Resin.

instance. All materials were positioned in roughly the center of the thickness using fishing line. The goal of these tests is to determine whether or not these inserted defects, which are well below the surface, can be successfully detected by the system.

The first test performed was to determine whether the two planar defects could be successfully detected using the system. Since there are no variations in the emissivity of the sample, and the values are relatively high (0.83), there are no concerns about losing information due to reflected radiation for this analysis. However, due to the extremely low conductivity of the material (approx. 0.025 W/m K), the heating element temperature was raised to 100° C in an attempt to create a higher temperature gradient. The image of corrected temperature for this test can be seen in Fig. 5.16.

Due to the extremely low thermal conductivity of the resin, the temperature variation within the sample is relatively small, even after a longer period of time has elapsed for the experiment (in this case, approximately 15 minutes). However, there is a significant change in temperature in the lower right quadrant of the image where the foam is located. While we have already demonstrated that a defect (which typically represents a reduction in conductivity) will create an increase in temperature, it is also possible that if a portion of the material has an increased thermal conductivity the opposite effect can be seen. In this case, the foam material appears to have a higher conductivity than the surrounding resin and therefore pulls heat out of the surrounding resin which results in a lower temperature. Another interesting item to note is that while the foam portion is visible in this image, the aluminum is not. It is believed that due to the relatively small amount of aluminum in the sample, the amount of heat that the aluminum pulled away from the surrounding resin was much smaller than the foam, even though the aluminum has a much higher thermal conductivity.

While this anomaly can be easily seen in the corrected temperature image, the gradient image, shown in Fig. 5.17, offers little to verify that a defect is present. Again, it is believed that the extremely low conductivity of the resin makes it difficult to produce a high temperature gradient of any type, whether from a high heat flux or a defect present in the system. While it may be possible in this case to facilitate a higher temperature gradient by continually raising the temperature of the heating element until a desirable gradient is achieved, it is not recommended due to the potential for damage to the material, potential injury to the operator, and the increased energy required to raise the temperature. Therefore, due to the system's inability to produce a significant temperature

gradient across the sample, one may conclude that it will not be attractive in circumstances where the conductivity of the sample is at such a low range.

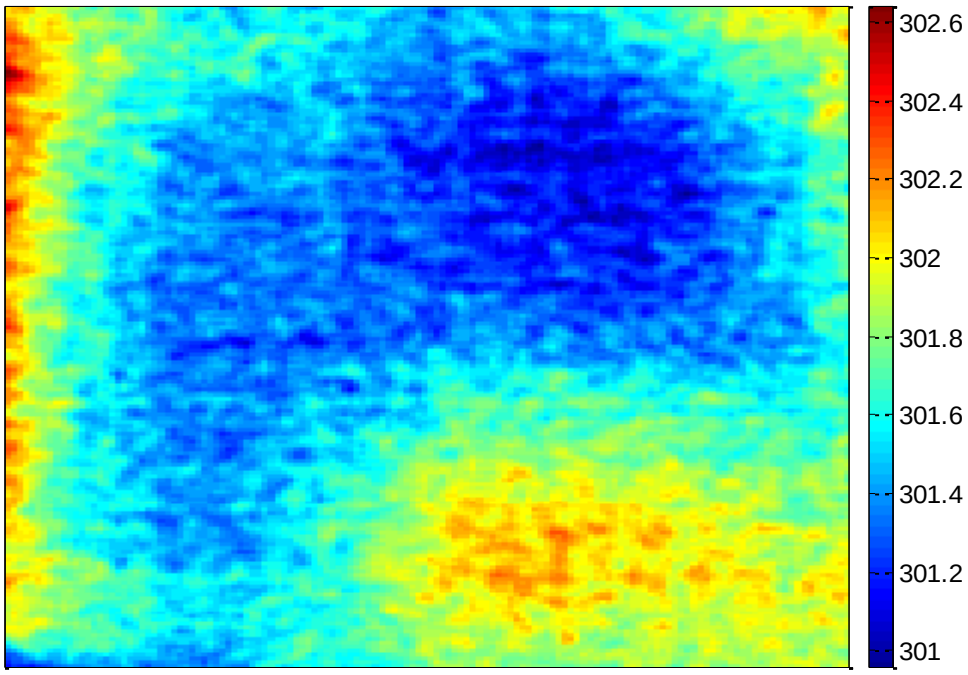

Fig. 5.16 Corrected Temperature of Resin/Epoxy Sample – Foam/Aluminum Portion.

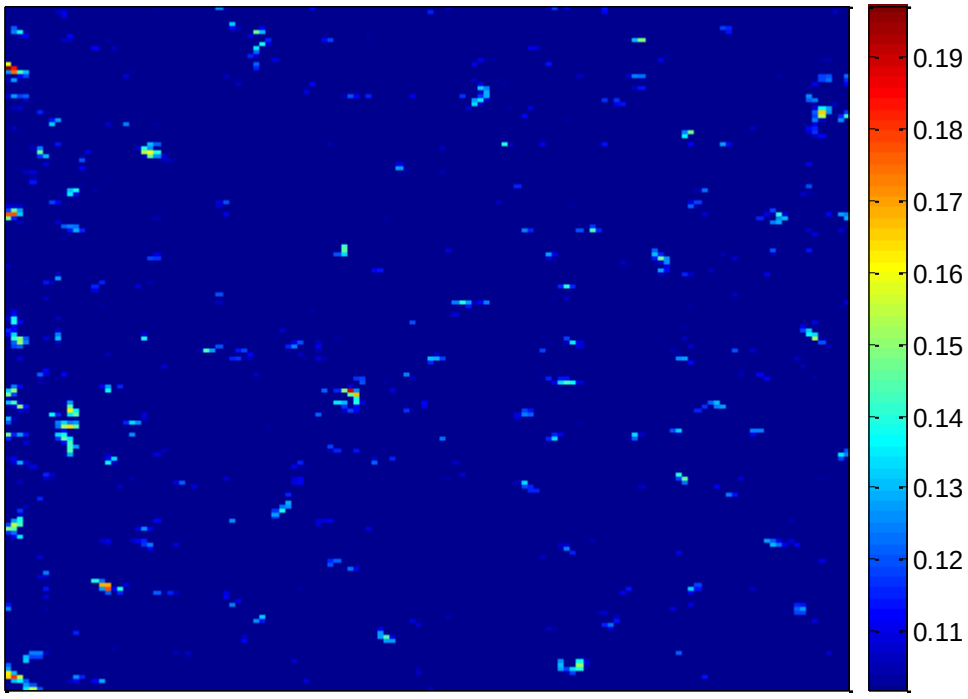

Fig. 5.17 Temperature Gradient on Resin/Epoxy Sample – Foam/Aluminum Portion.

The second test performed with this sample is to determine whether the two types of spherical defects embedded in the sample can be detected by the system. Again, due to the conductivity of the resin, the operating temperature of the heating element was raised to 100° C. The corrected temperature of the sample can be seen in Fig. 5.18. In the corrected temperature image, there is no sign of any spherical defect embedded in the material. It is believed that, like the aluminum in the previous test, the objects are too small to have a significant effect on the surface temperature. While the lead weights have a significantly higher thermal conductivity than the surrounding, the plastic beads do not and would be even more difficult to locate.

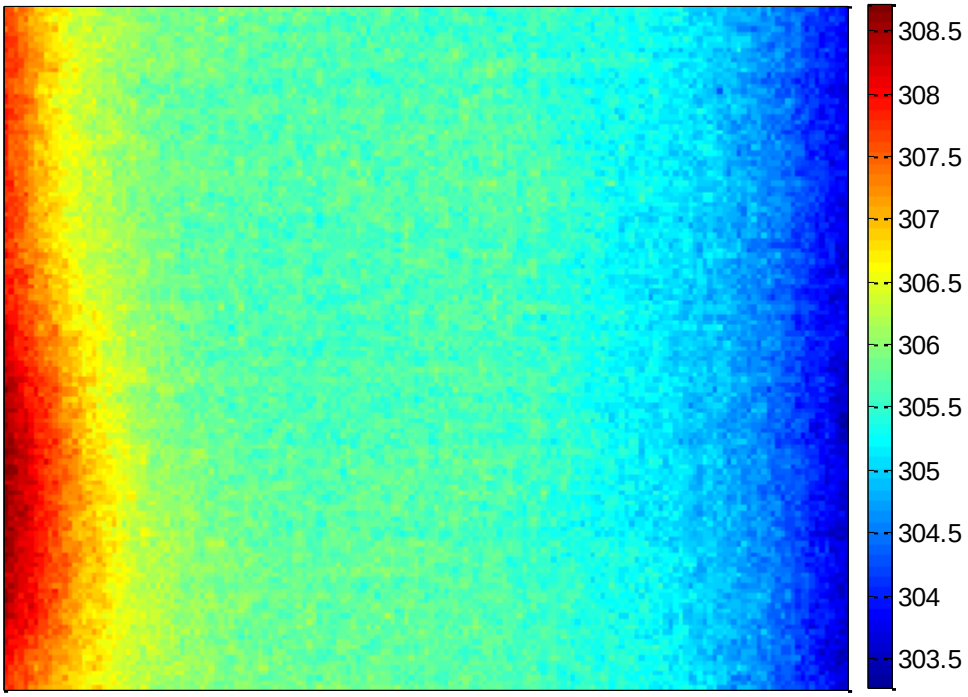

Fig. 5.18 Corrected Temperature of Epoxy Resin Sample – Spherical Defect Portion.

5.3.2 Carbon Fiber/Epoxy Resin Composite

With the increase in use of a variety of composites, including carbon fiber/epoxy resin, it is important to determine which type of NDEs that can be successfully used to inspect the materials. In this case, the system will be used to determine what differences, if any, can be detected between the two samples, which are shown in Fig. 5.19. The two composites in questions vary in how the layers are oriented. The first composite sample is a cross-ply sample, where the fiber orientation in some layers is perpendicular to others. The second composite sample is a unidirectional composite, where all fibers are oriented in the same direction. In addition to fiber orientation, an error in fabrication led to the unidirectional composite sample being unsatisfactory. The layers of the sample are not well laminated and a large delamination can be seen in the cross-section of the sample, which is shown in Fig. 5.20. The analysis procedure for these samples is the same as previous tests, with one minor change – in order to compare the two samples, data was taken after 15 minutes of heating for both samples. Again, due to the high emissivity of both samples (0.91 – 0.94), reflected radiation is not a concern. The goal of this analysis will be to determine whether there is any noticeable difference in temperature distribution between the two samples.

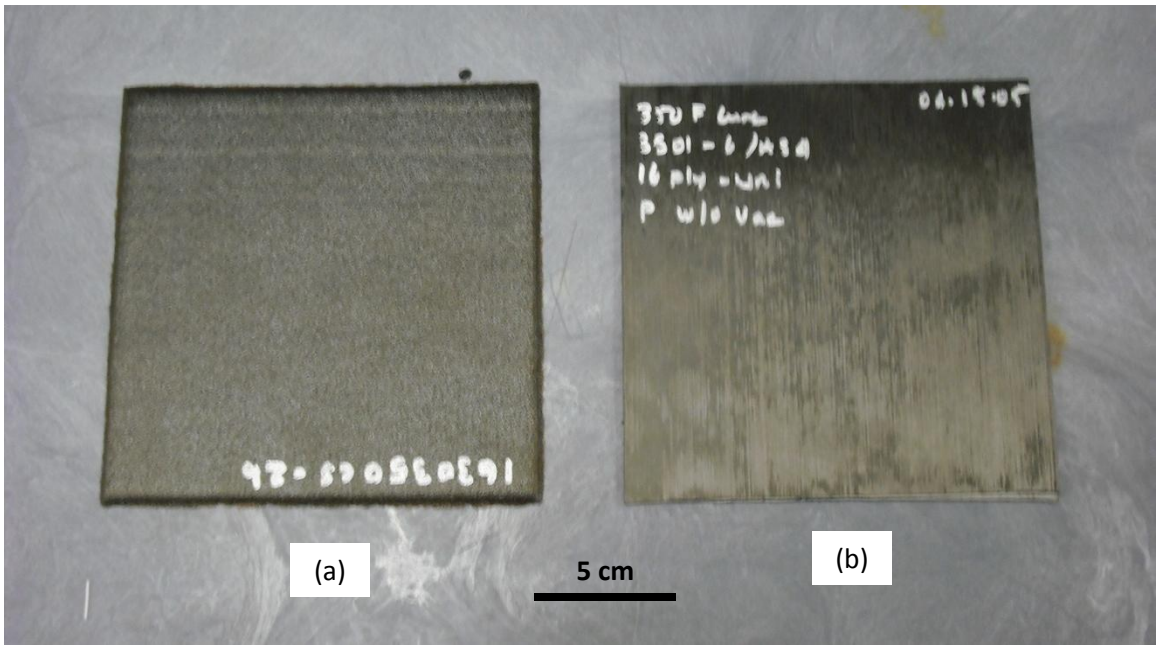

Fig. 5.19 Comparison of Two Composite Samples, (a) Cross-ply Composite, (b) Unidirectional Composite.

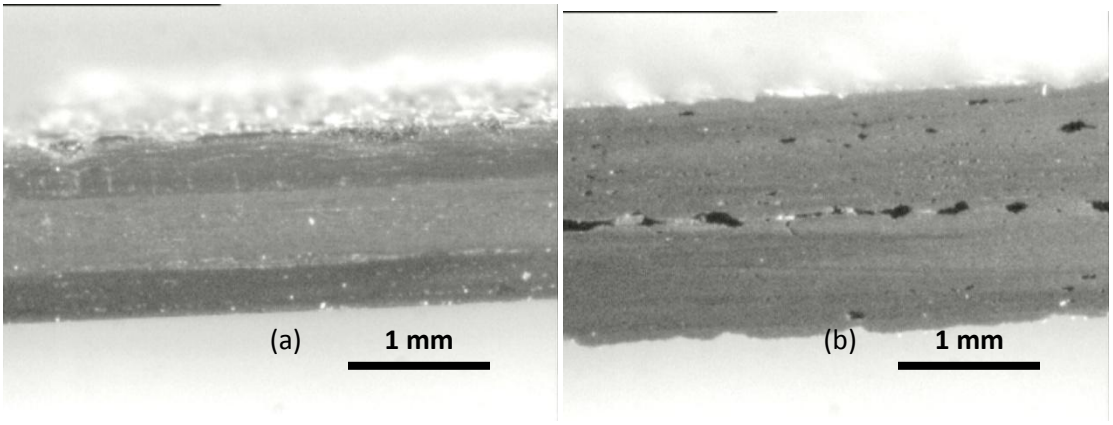

Fig. 5.20 Comparison of Composite Cross-Sections, (a) Cross-Ply Composite, (b) Unidirectional Composite.

Figure 5.21 shows a comparison of the two corrected temperature profiles. There are two noticeable differences between the two temperature profiles: the profile for the unidirectional composite exhibits a higher rate of heat transfer (shown by an elevated surface temperature) as well as higher dissipation of heat near the edges of the sample. The first difference can be explained by the difference in fiber orientation; in the cross-ply case, a lower overall thermal conductivity is seen in the sample due to the change in material between the carbon fibers and the epoxy resin matrix in the direction of the heat flux. In the unidirectional case, the carbon fibers are continuous in the direction of the heat flux which leads to improved heat transfer in that direction. The second difference in the profiles is believed to be caused by the difference in thickness between the samples as well as the poorly laminated edges in the unidirectional sample. While the two samples display unique temperature profiles, the system was unable to locate the significant delamination present in the unidirectional sample. In this case, a system such as flash thermography that has a heat flux permeated through the depth of the material rather than the length may be preferable, or if this system is used, a scanning system with the modifications mentioned in the previous chapter may be used with some success.

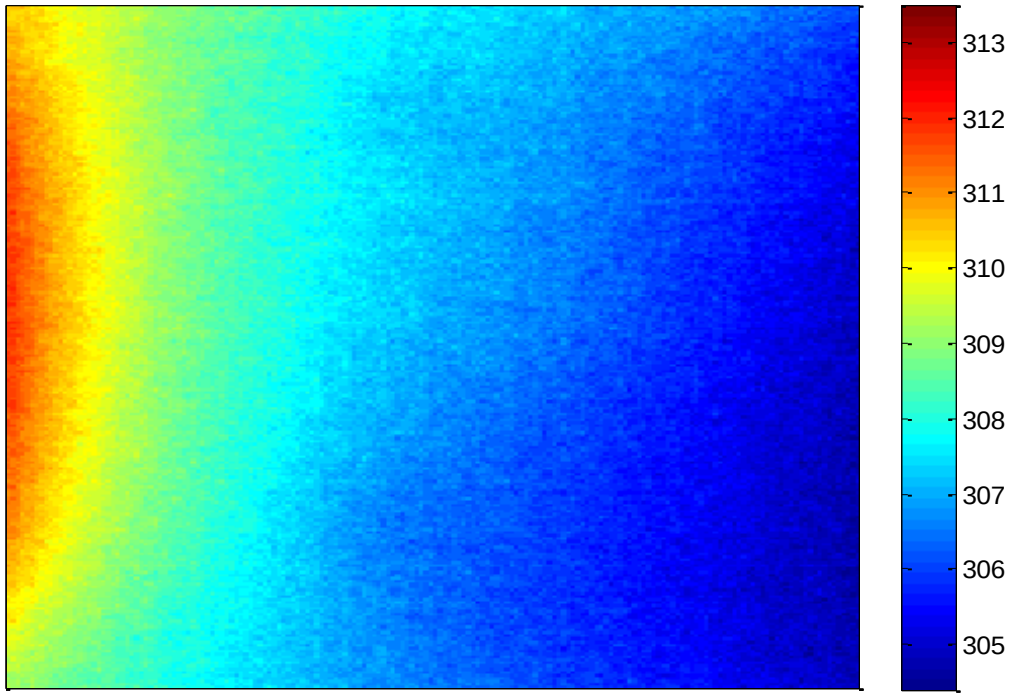

(a)

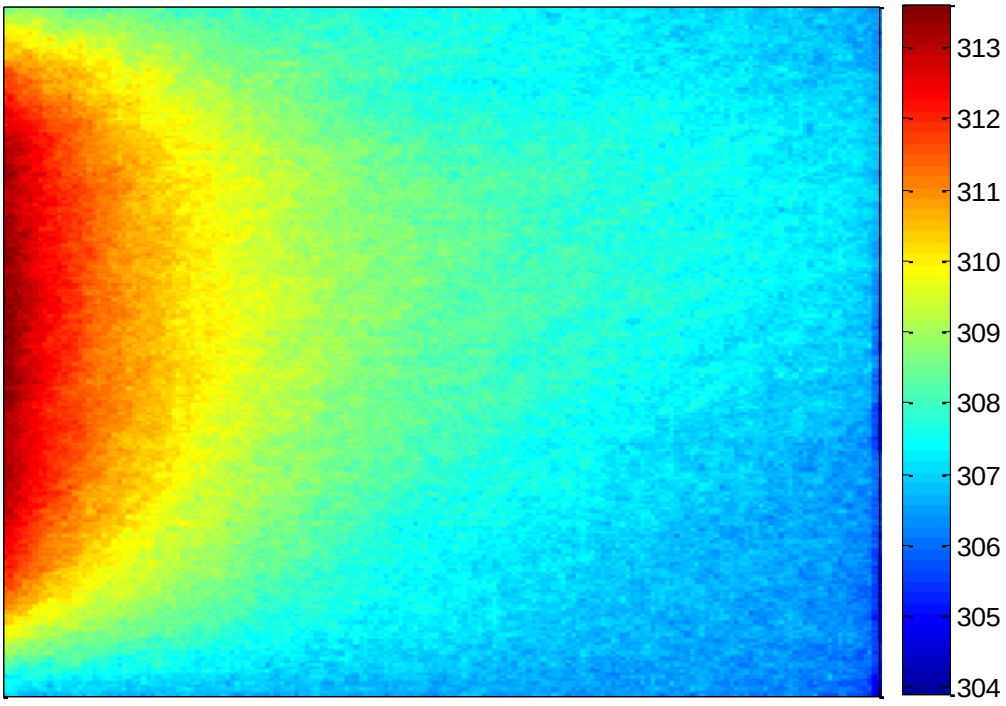

(b)

Fig. 5.21 Comparison of Temperature Profiles of Two Composite Samples, (a) Well Formed Composite Sample, (b) Poorly Formed Composite Sample.

CHAPTER SIX

CONCLUSIONS

6.1 System Improvements

The new test bed and LabView program have allowed for simpler testing by simplifying the movement of the camera, collecting all temperature data electronically and analyzing it in one single program instead of collecting temperature data manually and transferring data from one software program to another. The program is quite computationally intensive but with the advances in computer memory in recent years this is not a difficulty. It is reasonable to believe that a system using a similar analysis technique, with an accompanying LabView program could be implemented with little or no difficulties, and that personnel could be trained in its use in a relatively short period of time.

6.2 Reflected Radiation Reduction

Improvements in hardware, particularly the use of thermocouples and the improved camera shroud have allowed for more precise measurements to be used for the removal of reflected radiation. The camera shield in particular maintains a much more uniform temperature that removes a lot of the errors in calculation we experienced in the previous iteration of the system. Samples that have variable emissivity that are diffuse in nature can now be correctly analyzed with the current iteration of the system, but the system still has difficulties in analyzing surfaces that are specular in nature. This problem will only be exacerbated in a system with motion since specular surfaces reflect in a specific direction; any attempts to remove the effects of specularity will have to be position dependent in order to correctly quantify the effects.

6.3 Computer Models

The computational models developed within have provided a better understanding of the limitations and opportunities for this system. The two-dimensional models presented provided an opportunity to evaluate the potential resolution of the system; currently, the model predicts successful detection of crack defects at a size of approximately 0.5 cm in frontal area. This resolution is highly dependent on the distance of the camera from the sample being viewed; in a system where the camera is positioned closer to the sample it is possible to achieve even higher resolution in locating these types of defects. The three-dimensional models showed the potential difficulty in locating sub-surface defects with a stationary system. The defects were marginally visible, but a scanning system would allow for much better detection of these type of defects.

The program developed to analyze the radiative heat transfer characteristics of the camera shroud showed that the shroud itself has very little effect on the radiation received by the camera. All 4 sides of the shroud are at perpendicular or oblique angles with respect to the upper surface where the camera is located, so the majority of the radiation emitted from these surfaces does not reach the camera unless reflected by the sample surface. The program also showed that only a small fraction of the radiation emitted by the surface being analyzed actually reaches the camera for analysis. However, this issue has been considered by the camera designers and the radiation values collected by the camera have been altered accordingly.

6.4 Experimental Testing

The initial experimental tests performed verified that the improvements in hardware and software have improved the ability of removing reflected radiation to the

point that surfaces that are diffuse in nature can be successfully analyzed provided they are diffuse in nature. However, these tests also verified that the system still has issues with low emissivity, specular surfaces. Future design will have to incorporate specularity considerations if the desire is to have a system that can handle any type of surface.

The experimental tests on non-metallic samples proved only marginally successful. The epoxy resin sample demonstrated that materials with extremely low emissivity will always be difficult to analyze with the current iteration of the system due to the slow speed with which the heat permeates through the material. Since the system is dependent on producing a reasonable temperature gradient throughout the sample, any material with a sufficiently low thermal conductivity will prove difficult to analyze. However, the system was still able to successfully detect a change in thermal conductivity within the sample; in fact, the test showed that a sample with a portion at elevated thermal conductivity can be successfully analyzed as well.

Testing on the composites revealed that the thermal conductivity of the material was not prohibitive for testing using this system. In the future, systems of this type could be used to locate crack defects relatively easily. However, the manufacturing defects present in one sample were not detectable. In the future, a scanning system may have the capability to detect defects of this nature, but currently a better option may be flash diffusivity systems.

6.5 Coating Analysis

Since there are still issues with removing some types of reflected radiation for analysis, coatings are becoming a more likely option to improve the emissivity and reduce specularity for a given sample. Testing showed that emissivity proves to be fairly

independent of color, with the exception of black which proved to have the highest emissivity of all colors tested. In addition, it was shown that reducing the amount of paint within the coating will still provide an improved emissivity, but also reduce costs. Obviously the cost of coatings could prove to be very prohibitive for large surfaces to be analyzed. However, if the cost of time wasted with more time consuming evaluation techniques is considered, the method of coating samples may prove to be cost-effective.

6.6 Automation

While this system is still not fully automated to allow for a true scanning system, several considerations have already been made regarding how the current system could be modified to allow for scanning. Theoretical analysis discussed in Chapter 2 showed that the temperature profile of a system in motion can be easily determined given the material analyzed and the scanning speed of the system. Since the system will be in motion, the method of analysis will have to be altered considerably to operate correctly. However, it is still conceivable that the system could still collect the pertinent data required while moving and still utilize a similar method of removing reflected radiation. Although there will be a considerable temperature gradient in a portion of the system that may disallow the current gradient method of defect detection, it is possible that using an expected temperature distribution and comparing it to a distribution experimentally found, the difference between the two could be used to successfully locate potential defects.

REFERENCES

[1] Mix, P. E., *Introduction to Nondestructive Testing: A Training Guide*, 2nd ed., Wiley Interscience, Hoboken, NJ, 2005.

[2] Woolward, D. F., Cramer, K. E., "Line Scan versus Flash Thermography: Comparative Study on Reinforced Carbon-Carbon," *Proceedings of SPIE*, Vol. 5782, pp. 315-323, 2005.

[3] Maldague, X. P. V., *Theory and Practice of Infrared Technology for Nondestructive Testing*, John Wiley & Sons, New York, 2001.

[4] Dewitt, D. P., and Incropera, F. P., *Fundamentals of Heat and Mass Transfer*, 5th ed., Wiley, New York, NY, 2001.

[5] Sayers, C. M., "Detectability of Defects by Thermal Non-Destructive Testing," *British Journal of NDT*, Vol. 26, No. 1, pp. 28-33, 1984.

[6] Killey, A., and Sargent, J. P., "Analysis of Thermal Non-Destructive Testing," *Journal of Physics D: Applied Physics*, Vol. 22, pp. 216-224, 1989.

[7] Cramer, K. E., Winfree, W. P., Howell, P. A., Syed, H. I., and Renouard, K. A., "Thermographic Imaging of Cracks in Thin Metal Sheets," *Proceedings of SPIE*, Vol. 1682, pp. 162-170, 1992.

[8] Cramer, K. E., Winfree, W. P., "Application of the Thermal Line Scanner to Quantify Material Loss Due to Corrosion," *Proceedings of SPIE*, Vol. 4020, pp. 210-219, 2000.

[9] Cramer, K. E., and Winfree, W. P., "Thermographic Imaging of Material Loss in Boiler Water-Wall Tubing by Application of Scanning Line Source," *Proceedings of the SPIE*, Vol. 3995, pp. 600-609, 2000.

[10] Cramer, K. E. "Quantitative Thermal Imaging of Aircraft Structures," *Proceedings of SPIE*, Vol. 2473, pp. 226-232, 1995.

[11] Cramer, K. E., and Winfree, W. P., "Thermal Characterization of Defects in Aircraft Structures via Spatially Controlled Heat Application," *Proceedings of SPIE*, Vol. 2766, pp. 202-209, 1996.

[12] Avdelidis, N. P., Almond, D. P., Dobbinson, A., Hawtin, B., Ibarra-Castanedo, C., and Maldague, X., "Thermal Transient Thermographic NDT&E of Composites," *Proceedings of the SPIE*, Vol. 5405, pp. 403-408, 2004.

[13] Howell, P. A., Winfree, W. P., and Cramer, K. E., "On-orbit Passive Thermography," *Nondestructive Testing and Evaluation*, Vol. 23, No. 3, pp. 195-210, 2008.

[14] Klein, M. T., Ibarra-Castanedo, C., Maldague, X. P., Bendada, A., "A Straightforward Graphical User Interface for Basic and Advanced Signal Processing of Thermographic Infrared Sequences," *Proceedings of the SPIE*, Vol. 6939, pp. 1-9, 2008.

[15] Penner, N., Non-Destructive Thermal Imaging of Metal Samples, Undergraduate Research Project Report, University of Oklahoma, 2007.

[16] Dalton, C., Olson, B., and Lai, F. C., "Nondestructive Evaluation of Surface Defects Using Scanning Infrared Thermography," *Journal of Thermophysics and Heat Transfer*, Vol. 23, No. 4, pp. 716-723, 2009.

[17] Dalton, C., Olson, B., and Lai, F. C., "Using Scanning Infrared Thermography for Low and Variable Emissivity Surfaces," *Proceedings of the ASME Summer Heat Transfer Conference*, HT2009-88645 (CD-ROM), 2009.

[18] Özişik, M. N., *Basic Heat Transfer,* McGraw-Hill, New York, NY, 1977.

[19] Krieth, F., and Bohn M. S., *Principles of Heat Transfer,* 5th ed., PWS Publishing, Boston, MA, 1997.

[20] ThermoVision A20M Operator's Manual.

[21] Dalton, C., *Using Scanning Infrared Thermography for Non-Destructive Evaluation of Materials,* University of Oklahoma, Master's Thesis, 2007.

[22] Hamilton, D. C. and Morgan, W. R., 1952, *Radiant-Interchange Configuration Factors, NASA TN* 2836.

[23] Hottel, H. C., "Radiant Heat Transmission between Surfaces Separated by Non-Absorbing Media," *Transactions of ASME,* Vol. 53, pp. 265-273, 1931.

[24] Hollands, K. G. T., "On the Superposition Rule for Configuration Factors," *Journal of Heat Transfer,* Vol. 117, No. 1, pp. 241-245, 1995.

APPENDIX A: NOMENCLATURE

A	area (m^2)
A_x	cross-sectional area (m^2)
A_y	cross-sectional area (m^2)
A_n	integration constant
B	integration constant
Bi	Biot number
c	specific heat (J/kg K)
c_0	integration constant
c_1	integration constant
c_2	integration constant
C	integration constant
e	Euler number
F	shape factor
g	arbitrary function
G	gradient (°C)
h	convective heat transfer coefficient (W/m^2 K)
i	computational index
j	computational index
J	radiative energy emitted (W)
J_{cam}	camera radiosity (W)
k	computational index
k_x	thermal conductivity (W/m K)

k_y	thermal conductivity (W/m K)
L	length (m)
m	time index
M	edge node
M_b	total radiation of a blackbody (W)
N	edge node
Q	conductive heat transfer (W)
R	distance between surfaces (m)
T	time (s)
T	temperature (°C)
T_0	boundary temperature (°C)
T_{amb}	ambient temperature (°C)
T_{actual}	actual temperature (°C)
T_i	initial temperature (°C)
T_{meas}	measured temperature (°C)
T_{surf}	surface temperature (°C)
T_{ref}	reflected temperature (°C)
T_s	steady-state temperature solution
T_t	transient temperature solution
T_∞	ambient temperature (°C)
v_t	translation velocity (m/s)
W	width (m)
x	position

x_L	local coordinate system
x_T	total coordinate system
y	position
z	position

α	thermal diffusivity (m^2/s)
α_{abs}	absorptivity
Δ	change in variable
ε	emissivity
ε_{actual}	actual emissivity
ε_{cam}	camera emissivity
θ	polar angle
λ	eigenvalue
λ_n	eigenvalue
π	pi
ρ	density (kg/m^3)
ρ_{ref}	reflectivity
σ	Stefan-Boltzmann constant
τ	transmissivity
Φ	included angle
λ	eigenvalue

APPENDIX B: COMPUTATIONAL CODES

This is a collection of the computational codes that were developed for Chapter 4. They were all written and compiled using Matlab.

Longitudinal Crack Program

```
% This is a finite difference program that solves a
% rectangular transient 2d conduction problem with
% the presence of a longitudinal crack

clear all;                    % Clear all stored variables

%%%%%%%%%%%% MODEL PARAMETERS %%%%%%%%%%%%%%%%%%%%%%
L=0.15;                       % Rectangle Length (m)
W=0.15;                      % Rectangle width (m)

N=200;                        % Number of length
calculation nodes
M=200;                        % Number of width calculation
nodes

kx=14;                        % Material x thermal
conductivity (W/mC)
ky=14;                        % Material y thermal
conductivity (W/mC)
kc=.026;                % crack thermal conductivity
pC=3603637;             % Heat capacity (density*specific
heat) (J/m^3C)
pCa=1175;               % Heat capacity air
To=25;                  % Initial temperature (C)
dy=L/(N-1);                   % Define grid element size
dx=W/(M-1);
h=12;                   %heat transfer coefficient W/m^2K
Tinf=25;                %ambient temperature

if(dx<dy) dt=dx^2/(8*kx/pC); else dt=dy^2/(8*ky/pC);
end%critical time step
t_stop=600;               % Stop time (sec)

%%%%%%%%%%%% ITERATIVE TEMPERATURE COMPUTATION
%%%%%%%%%%%%%%%%
T=To*ones(N,M);         % Initialize temperature matrix
```

```
T(:,1)=60;                % Set left fixed temperature
boundary condition



t=0;                    % Intialize iteration counters

while t<t_stop          % Iteration loop

    for i=2: 1: N-1                 %left nodes
        for j=2: 1: M/2-2
           T(i,j)=T(i,j)+...
          (kx*dt/(pC*dx^2))*(T(i,j-1)-
2*T(i,j)+T(i,j+1))+...
          (ky*dt/(pC*dy^2))*(T(i-1,j)-2*T(i,j)+T(i+1,j));
        end
    end

    for i=2: 1: N-1                 %right nodes
        for j=M/2+1: 1: M-1
            T(i,j)=T(i,j)+...
          (kx*dt/(pC*dx^2))*(T(i,j-1)-
2*T(i,j)+T(i,j+1))+...
          (ky*dt/(pC*dy^2))*(T(i-1,j)-2*T(i,j)+T(i+1,j));
        end
    end

    for i=N/2-13: 1: N/2+13                 %crack nodes
            T(i,M/2-1)=T(i,M/2-1)+...
          (kc*dt/(pCa*dx^2))*(T(i,M/2)-T(i,M/2-1))+...
          (kx*dt/(pC*dx^2))*(T(i,M/2-2)-T(i,M/2-1))+...
          (ky*dt/(pC*dy^2))*(T(i-1,M/2-1)-2*T(i,M/2-
1)+T(i+1,M/2-1));
       T(i,M/2)=T(i,M/2)+...
          (kx*dt/(pC*dx^2))*(T(i,M/2+1)-T(i,M/2))+...
          (kc*dt/(pCa*dx^2))*(T(i,M/2-1)-T(i,M/2))+...
          (ky*dt/(pC*dy^2))*(T(i-1,M/2)-
2*T(i,M/2)+T(i+1,M/2));
    end

    for i=2: 1: N/2-14                %above crack nodes
        for j=M/2-1: 1: M/2
            T(i,j)=T(i,j)+...
          (kx*dt/(pC*dx^2))*(T(i,j-1)-
2*T(i,j)+T(i,j+1))+...
          (ky*dt/(pC*dy^2))*(T(i-1,j)-2*T(i,j)+T(i+1,j));
        end
```

```
    end

    for i=N/2+14 : 1: N-1                  %below crack
nodes
        for j=M/2-1: 1: M/2
            T(i,j)=T(i,j)+...
          (kx*dt/(pC*dx^2))*(T(i,j-1)-
2*T(i,j)+T(i,j+1))+...
          (ky*dt/(pC*dy^2))*(T(i-1,j)-2*T(i,j)+T(i+1,j));
        end
    end


    for i=2: 1: N-1                        %right boundary
        T(i,M)=T(i,M)+((dt)/(pC*dx^2))*...
            ((ky*((T(i+1,M)+T(i-1,M))/2+T(i,M-1)-
2*T(i,M)))-...
            h*dx*(T(i,M)-Tinf));
    end

    for j=2: 1: M-1                        %top and bottom
boundaries
        T(1,j)=T(1,j)+((2*dt)/(pC*dx^2))*((kx*((T(1,j-
1)+...
            T(1,j+1))/2+T(2,j)-2*T(1,j)))-h*dx*(T(1,j)-
Tinf));
        T(N,j)=T(N,j)+((2*dt)/(pC*dx^2))*((kx*((T(N,j-
1)+...
            T(N,j+1))/2+T(N-1,j)-2*T(N,j)))-h*dx*(T(N,j)-
Tinf));
    end

    T(1,M)=T(1,M-1);
    T(N,M)=T(N,M-1);

    t=t+dt;               % Index time variable
    fprintf(1,'t/tstop = %g \n',t/t_stop);

end


G=zeros(N,M);           %Gradient calculation

 for i=2: 1: N-1
        for j=2: 1: M-1
            G(i,j)=sqrt((T(i-1,j)-T(i+1,j))^2+(T(i,j-1)-
T(i,j+1))^2);
```

```
        end
 end

 G2=zeros(N,M);          %second gradient calculation

 for i=2: 1: N-1
        for j=2: 1: M-1
            G2(i,j)=sqrt((G(i-1,j)-G(i+1,j))^2+(G(i,j-1)-
G(i,j+1))^2);
        end
 end
figure(1);
contourf(T);
figure(2);
contourf(G);
figure(3);
contourf(G2);
```

Angled Crack Program

```
% This is a finite difference program that solves a
% rectangular transient 2d conduction problem with a 45
degree crack

clear all;                      % Clear all stored variables

%%%%%%%%%%%% MODEL PARAMETERS %%%%%%%%%%%%%%%%%%%%%%%
L=0.15;                         % Rectangle Length (m)
W=0.15;                        % Rectangle width (m)

N=200;                          % Number of length
calculation nodes
M=200;                          % Number of width calculation
nodes

kx=237;                         % Material x thermal
conductivity (W/mC)
ky=237;                         % Material y thermal
conductivity (W/mC)
kc=.026;                % crack thermal conductivity
pC=2439906;             % Heat capacity (density*specific
heat) (J/m^3C)
pCa=1175;               % Heat capacity air
To=25;                  % Initial temperature (C)
dy=L/(N-1);                     % Define grid element size
dx=W/(M-1);
```

```
h=12;                     %heat transfer coefficient W/m^2K
Tinf=25;                  %ambient temperature

if(dx<dy) dt=dx^2/(4*kx/pC); else dt=dy^2/(4*ky/pC);
end%critical time step
t_stop=60;                % Stop time (sec)

%%%%%%%%%%% ITERATIVE TEMPERATURE COMPUTATION
%%%%%%%%%%%%%%%%
T=To*ones(N,M);           % Initialize temperature matrix

an=(ky/pC)*ones(N,M);     % Initialize diffusivity matrices
as=(ky/pC)*ones(N,M);     % (n=north, s=south, e=east, w=west
ae=(kx/pC)*ones(N,M);
aw=(kx/pC)*ones(N,M);

T(:,1)=60;                % Set left fixed temperature
boundary condition

for i=86: 1: 114          % Set diffusivity for crack nodes
    an(i,i)=kc/pCa;
    ae(i,i)=kc/pCa;
    as(i-1,i)=kc/pCa;
    aw(i-1,i)=kc/pCa;
end

t=0;                      % Intialize iteration counters

while t<t_stop            % Iteration loop

    for i=2: 1: N-1
        for j=2: 1: M-1
           T(i,j)=T(i,j)+...
          (an(i,j)*dt/(dx^2))*(T(i-1,j)-T(i,j))+...
          (as(i,j)*dt/(dx^2))*(T(i+1,j)-T(i,j))+...
          (aw(i,j)*dt/(dx^2))*(T(i,j-1)-T(i,j))+...
          (ae(i,j)*dt/(dx^2))*(T(i,j+1)-T(i,j));
        end
    end




    for i=2: 1: N-1                        %right boundary
        T(i,M)=T(i,M)+((dt)/(pC*dx^2))*((ky*((T(i+1,M)+T(i-
1,M))/2+...
            T(i,M-1)-2*T(i,M)))-h*dx*(T(i,M)-Tinf));
```

```
    end

    for j=2: 1: M-1                        %top and bottom
boundaries
        T(1,j)=T(1,j)+((2*dt)/(pC*dx^2))*((kx*((T(1,j-
1)+T(1,j+1))/2+...
            T(2,j)-2*T(1,j)))-h*dx*(T(1,j)-Tinf));
        T(N,j)=T(N,j)+((2*dt)/(pC*dx^2))*((kx*((T(N,j-
1)+T(N,j+1))/2+...
            T(N-1,j)-2*T(N,j)))-h*dx*(T(N,j)-Tinf));
    end

    T(1,M)=T(1,M-1);
    T(N,M)=T(N,M-1);

    t=t+dt;               % Index time variable
    fprintf(1,'t/tstop = %g \n',t/t_stop);

end


G=zeros(N,M);           % Gradient Calculation

 for i=2: 1: N-1
        for j=2: 1: M-1
            G(i,j)=sqrt((T(i-1,j)-T(i+1,j))^2+(T(i,j-1)-
T(i,j+1))^2);
        end
 end

 G2=zeros(N,M);         % Second Gradient Calculation

 for i=2: 1: N-1
        for j=2: 1: M-1
            G2(i,j)=sqrt((G(i-1,j)-G(i+1,j))^2+(G(i,j-1)-
G(i,j+1))^2);
        end
 end
figure(1);
contourf(T);
figure(2);
contourf(G);
figure(3);
contourf(G2);
```

Three-dimensional Program

```
% This is a finite difference program that solves a
% rectangular transient 3d conduction problem with
potential voids
% and thinnings

clear all;                    % Clear all stored variables

%%%%%%%%%%%% MODEL PARAMETERS %%%%%%%%%%%%%%%%%%%%%%
L=0.15;                       % Rectangle Length (m)
W=0.15;                      % Rectangle width (m)
Z=0.01;                  % Rectangle thickness (m)

N=50;                         % Number of length
calculation nodes
M=50;                         % Number of width calculation
nodes
P=8;                    % Number of thickness calculation
nodes

kx=237;                       % Material x thermal
conductivity (W/mC)
ky=237;                       % Material y thermal
conductivity (W/mC)
kz=237;                  % Material z thermal conductivity
(W/mC)
ka=.026;                    % air thermal conductivity
(W/mC)

pC=2439906;              % Heat capacity (density*specific
heat) (J/m^3C)
pCa=1175;                % Heat capacity air
To=25;                   % Initial temperature (C)
dy=L/(N-1);                   % Define grid element size
dx=W/(M-1);
dz=Z/(P-1);
h=12;                    %heat transfer coefficient W/m^2K
Tinf=25;                 %ambient temperature

if(dx<dz) dt=dx^2/(8*kx/pC); else dt=dz^2/(8*kz/pC);
end%critical time step
t_stop=15;                % Stop time (sec)

%%%%%%%%%%%% ITERATIVE TEMPERATURE COMPUTATION
%%%%%%%%%%%%%%%%
T=To*ones(N,M,P);        % Initialize temperature matrix
```

```
T(:,1,1)=60;           % Set left fixed temperature
boundary condition


an=(ky/pC)*ones(N,M,P);
as=(ky/pC)*ones(N,M,P);
ae=(kx/pC)*ones(N,M,P);
aw=(kx/pC)*ones(N,M,P);
au=(kz/pC)*ones(N,M,P);
ad=(kz/pC)*ones(N,M,P);

for i=N/2-4: 1: N/2+4
    for j=M/2-4: 1: M/2+4
        for k=3: 1: 6
            an(i,j,k)=(ka/pCa);
            as(i,j,k)=(ka/pCa);
            ae(i,j,k)=(ka/pCa);
            aw(i,j,k)=(ka/pCa);
            au(i,j,k)=(ka/pCa);
            ad(i,j,k)=(ka/pCa);

            an(N/2-5,j,k)=(ka/pCa);
            as(N/2+5,j,k)=(ka/pCa);
            aw(i,M/2-5,k)=(ka/pCa);
            ae(i,M/2+5,k)=(ka/pCa);
            au(i,j,2)=(ka/pCa);
            ad(i,j,7)=(ka/pCa);
        end
    end
end



t=0;                    % Intialize iteration counters

while t<t_stop          % Iteration loop
    for i=2: 1: N-1                 %interior nodes
        for j=2: 1: M-1
          for k=2: 1: P-1
            T(i,j,k)=T(i,j,k)+...
          (an(i,j,k)*dt/(dy^2))*(T(i-1,j,k)-T(i,j,k))+...
          (as(i,j,k)*dt/(dy^2))*(T(i+1,j,k)-T(i,j,k))+...
          (aw(i,j,k)*dt/(dx^2))*(T(i,j-1,k)-T(i,j,k))+...
          (ae(i,j,k)*dt/(dx^2))*(T(i,j+1,k)-T(i,j,k))+...
          (au(i,j,k)*dt/(dz^2))*(T(i,j,k+1)-T(i,j,k))+...
          (ad(i,j,k)*dt/(dz^2))*(T(i,j,k-1)-T(i,j,k));
```

```
          end
        end
    end



    for i=2: 1: N-1                      %left and right
boundaries
        for k=2: 1: P-1
            T(i,1,k)=T(i,1,k)+((dt)/(pC))*...
                ((ky/dy^2)*(T(i+1,1,k)-2*T(i,1,k)+T(i-
1,1,k))+...
                (kz/dz^2)*(T(i,1,k+1)-2*T(i,1,k)+T(i,1,k-
1))+...
             (2*kx/dx^2)*(T(i,2,k)-T(i,1,k))-
(2*h/dx)*(T(i,1,k)-Tinf));
            T(i,M,k)=T(i,M,k)+((dt)/(pC))*...
                ((ky/dy^2)*(T(i+1,M,k)-2*T(i,M,k)+T(i-
1,M,k))+...
                (kz/dz^2)*(T(i,M,k+1)-2*T(i,M,k)+T(i,M,k-
1))+...
             (2*kx/dx^2)*(T(i,M-1,k)-T(i,M,k))-
(2*h/dx)*(T(i,M,k)-Tinf));
        end
    end

    for j=2: 1: M-1                      %north and south
boundaries
        for k=2: 1: P-1
            T(N,j,k)=T(N,j,k)+((dt)/(pC))*...
                ((kx/dx^2)*((T(N,j-1,k)-
2*T(N,j,k))+T(N,j+1,k))+...
                (kz/dz^2)*(T(N,j,k+1)-2*T(N,j,k)+T(N,j,k-
1))+...
                (2*ky/dy^2)*(T(N-1,j,k)-T(N,j,k))-...
                (2*h/dy)*(T(N,j,k)-Tinf));
            T(1,j,k)=T(1,j,k)+((dt)/(pC))*...
                ((kx/dx^2)*((T(1,j-1,k)-
2*T(1,j,k))+T(1,j+1,k))+...
                (kz/dz^2)*(T(1,j,k+1)-2*T(1,j,k)+T(1,j,k-
1))+...
                (2*ky/dy^2)*(T(2,j,k)-T(1,j,k))-...
                (2*h/dy)*(T(1,j,k)-Tinf));
        end
    end
```

```
    for i=2: 1: N-1                         %up and down
boundaries
        for j=2: 1: M-1
            T(i,j,1)=T(i,j,1)+((dt)/(pC))*...
                ((kx/dx^2)*(T(i,j-1,1)-
2*T(i,j,1)+T(i,j+1,1))+...
                (ky/dy^2)*(T(i-1,j,1)-
2*T(i,j,1)+T(i+1,j,1))+...
                (kz/dz^2)*(T(i,j,2)-T(i,j,1))-...
                (2*h/dz)*(T(i,j,1)-Tinf));
            T(i,j,P)=T(i,j,P)+((dt)/(pC))*...
                ((kx/dx^2)*(T(i,j-1,P)-
2*T(i,j,P)+T(i,j+1,P))+...
                (ky/dy^2)*(T(i-1,j,P)-
2*T(i,j,P)+T(i+1,j,P))+...
                (kz/dz^2)*(T(i,j,P-1)-T(i,j,P))-...
                (2*h/dz)*(T(i,j,P)-Tinf));
        end
    end

    T(1,:,1)=T(2,:,1);                      %edge boundaries
    T(N,:,1)=T(N-1,:,1);
    T(1,:,P)=T(2,:,P);
    T(N,:,P)=T(N-1,:,P);
    T(:,M,1)=T(:,M-1,1);
    T(:,M,P)=T(:,M-1,P);
    T(1,M,:)=T(2,M,:);
    T(N,M,:)=T(N-1,M,:);
    T(1,1,:)=T(2,1,:);
    T(N,1,:)=T(N-1,1,:);
    T(:,1,P)=T(:,2,P);

    t=t+dt;                % Index time variable
    fprintf(1,'t/tstop = %g \n',t/t_stop);

end

Tsurf=ones(N,M);         %surface temperature
Tsurf=T(:,:,1);
G=zeros(N,M);

 for i=2: 1: N-1             % gradient calculation
        for j=2: 1: M-1
            G(i,j)=sqrt((Tsurf(i-1,j)-Tsurf(i+1,j))^2+...
                (Tsurf(i,j-1)-Tsurf(i,j+1))^2);
        end
 end
```

```
 G2=zeros(N,M);

 for i=2: 1: N-1            % second gradient calculation
        for j=2: 1: M-1
            G2(i,j)=sqrt((G(i-1,j)-G(i+1,j))^2+(G(i,j-1)-
G(i,j+1))^2);
        end
 end

 Tside=ones(P,M);           % center line temperature
distribution
 for i=1: 1: P
     for j=1: 1: M
         Tside(i,j)=T(N/2,j,P+1-i);
     end
 end

figure(1);
contourf(Tsurf);
figure(2);
contourf(G);
figure(3);
contourf(G2);
figure(4);
contourf(Tside);
```

Radiative Heat Transfer Analysis Program

```
%This is a radiative heat transfer program to determine
%shape factor of a camera shroud


clear all;

%%%%%%%%%%Side 1%%%%%%%%%%%%%%%%%%

b1=0.135;       %width of receiving surface (m)
c1=0.05;        %length of receiving surface (m)
L1=0.11;        %length of emitting surface (m)
W1=0.135;       %width of emitting surface (m)
phi1=1.834;     %angle (radians)

N1=20;          %length nodes on emitting surface (m)
dx1=L1/N1;      %grid length on emitting surface
```

```
a1=ones(N1);    %distance from surface matrix
B1=ones(N1);
C1=ones(N1);
X1=ones(N1);
Y1=ones(N1);

F1=ones(N1);    %shape factor matrix

F1t=0;          %total shape factor

for i=2: 1: N1
    a1(i)=(i-1)*dx1;
    B1(i)=b1/a1(i);
    C1(i)=c1/a1(i);
    X1(i)=(C1(i)^2-2*cos(phi1)+1)^0.5;
    Y1(i)=(B1(i)^2+(sin(phi1))^2)^0.5;


F1(i)=(1/pi)*(atan(B1(i))+((sin(phi1)^2)/(2*B1(i)))*log((X1
(i)^2+...
        B1(i)^2)/((1+B1(i)^2)*X1(i)^2))-
(sin(2*phi1)/(2*B1(i)))*(pi/2-phi1+...
        atan((C1(i)-
cos(phi1))/sin(phi1)))+(Y1(i)/B1(i))*(atan((C1(i)-...

cos(phi1))/Y1(i))+atan(cos(phi1)/Y1(i)))*cos(phi1)+((C1(i)*
...
        cos(phi1)-1)/X1(i))*atan(B1(i)/X1(i)));

    F1t=F1t+dx1*W1*F1(i);
end

F1t

%%%%%%%%%%Side 2%%%%%%%%%%%%%%%%%%%

b2=0.135;       %width of receiving surface (m)
c2=0.05;        %length of receiving surface (m)
L2=0.165;       %length of emitting surface (m)
W2=0.135;       %width of emitting surface (m)
phi2=1.834;     %angle (radians)

N2=20;          %length nodes on emitting surface (m)
dx2=L2/N2;      %grid length on emitting surface

a2=ones(N2);    %distance from surface matrix
B2=ones(N2);
```

```
C2=ones(N2);
X2=ones(N2);
Y2=ones(N2);

F2=ones(N2);    %shape factor matrix

F2t=0;          %total shape factor

for i=2: 1: N2
    a2(i)=(i-1)*dx2;
    B2(i)=b2/a2(i);
    C2(i)=c2/a2(i);
    X2(i)=(C2(i)^2-2*cos(phi2)+1)^0.5;
    Y2(i)=(B2(i)^2+(sin(phi2))^2)^0.5;


F2(i)=(1/pi)*(atan(B2(i))+((sin(phi2)^2)/(2*B2(i)))*log((X2
(i)^2+...
        B2(i)^2)/((1+B2(i)^2)*X2(i)^2))-
(sin(2*phi2)/(2*B2(i)))*(pi/2-phi2+...
        atan((C2(i)-
cos(phi2))/sin(phi2)))+(Y2(i)/B2(i))*(atan((C2(i)-...

cos(phi2))/Y2(i))+atan(cos(phi2)/Y2(i)))*cos(phi2)+((C2(i)*
...
        cos(phi2)-1)/X2(i))*atan(B2(i)/X2(i)));

    F2t=F2t+dx2*W2*F2(i);
end

F2t

%%%%%%%%%%%%%%%%%%Sides 3 and 4%%%%%%%%%%%%%%%%%%%%%%%%%%

h3=0.135;           %width of receiving surface (m)
l3=0.05;            %length of receiving surface (m)
w3=0.12;            %length of emitting surface (m)

H3=h3/l3;
W3=w3/l3;

F3=(1/(W3*pi))*(W3*atan(1/W3)+H3*atan(1/H3)-
sqrt(H3^2+W3^2)*...

atan(sqrt(1/(H3^2+W3^2)))+0.25*log((((1+W3^2)*(1+H3^2))/(1+
W3^2+H3^2))*...
```

```
((W3^2*(1+W3^2+H3^2))/((1+W3^2)*(W3^2+H3^2)))^(W3^2)*...
    ((H3^2*(1+H3^2+W3^2))/((1+H3^2)*(H3^2+W3^2)))^(H3^2)));

F3t=l3*w3*F3
F4t=F3t
%%%%%%%%%%%%%%%%%%%%%%%%Camera Shroud Total%%%%%%%%%%%%%%%

Fct= (F1t+F2t+F3t+F4t)/(L1*W1+L2*W2+2*l3*w3)

%%%%%%%%%%%%%%%%%%%%%%%%Side 5%%%%%%%%%%%%%%%%%%%%%%%%%%%%

a5=0.135;           %width of receiving surface (m)
b5=0.05;            %length of receiving surface (m)
c0=0.12;            %normal distance between surfaces (m)
L5=0.135;           %width of emitting surface (m)
W5=0.125;           %length of emitting surface (m)

N5=40;              %number of vertical nodes
M5=40;              %number of horizontal nodes

dx=L5/N5;           %grid size
dy=W5/M5;

ai=1.571;            %angle in x
aj=1.0996;           %angle in y
ak=0.471;            %angle in z

A5=ones(N5,M5);
B5=ones(N5,M5);

F5=ones(N5,M5);     %shape factor matrix

F5t=0;              %total shape factor

for i=1: 1: N5
    for j=1: 1: M5
        A5(i,j)=a5/(c0+j*dy*tan(ak));
        B5(i,j)=b5/(c0+j*dy*tan(ak));

        F5(i,j)=(1/(2*pi))*(+atan(A5(i,j))*cos(aj)+...
            ((A5(i,j)*cos(ak)-
cos(ai))/(1+A5(i,j)^2)^0.5)*...
            atan(B5(i,j)/(1+A5(i,j)^2)^0.5)+...
            ((B5(i,j)*cos(ak)-
cos(aj))/(1+B5(i,j)^2)^0.5)*atan(A5(i,j)/...
            (1+B5(i,j)^2)^0.5));
```

```
        F5t=F5t+dx*dy*F5(i,j);
    end
end

F5t=F5t/(L5*W5);

F5t
```

APPENDIX C: ADDITIONAL COMPUTATIONAL RESULTS

The following are additional results produced by computational analysis that due to space were not included in the text of chapter 4.

C.1 Longitudinal Crack

2 cm crack

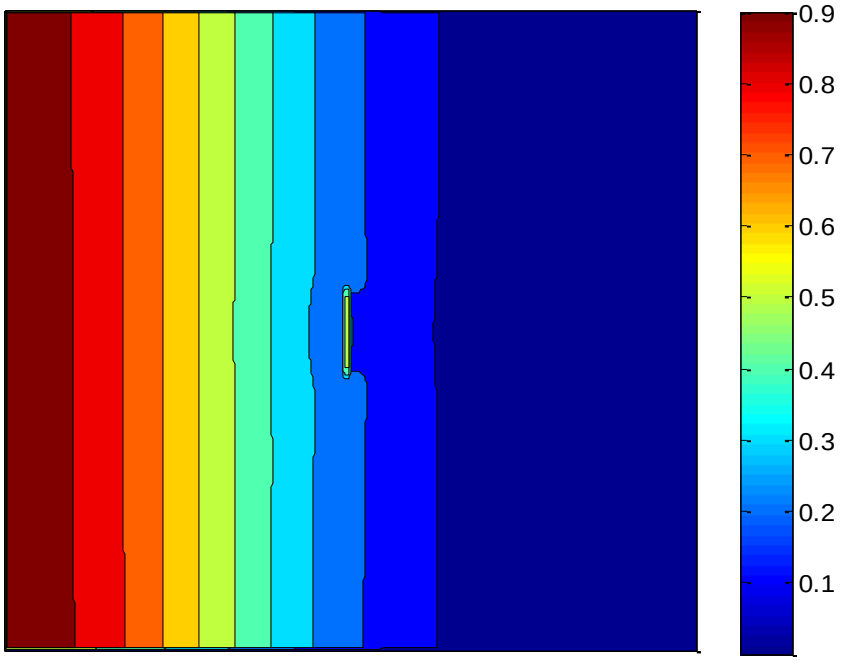

(a)

Fig. C.1 Images of Temperature Gradient for a 2-cm Longitudinal Crack, (a) at 5 seconds.

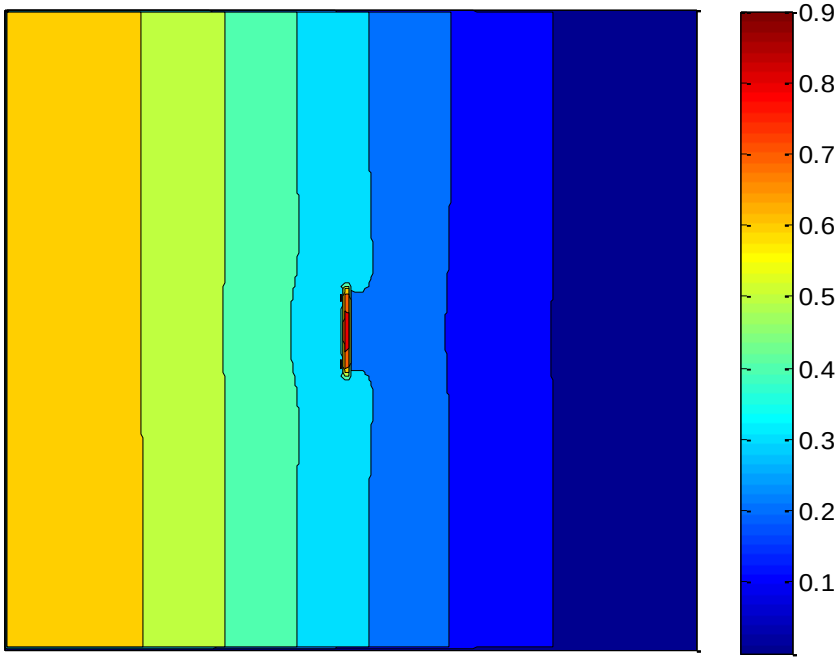

(b)

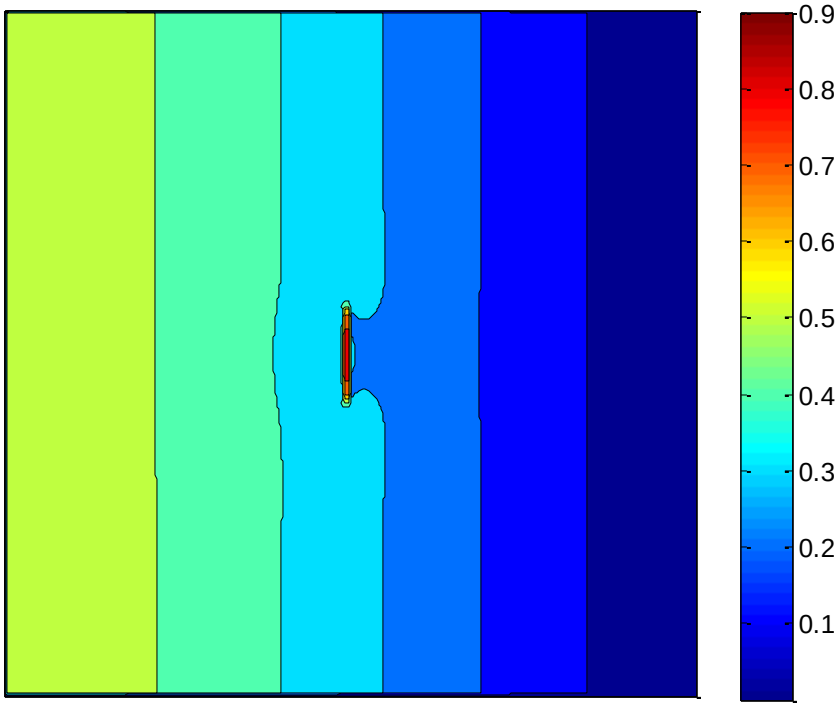

(c)

Fig. C.1 Images of Temperature Gradient for a 2-cm Longitudinal Crack (cont.), (b) at 10 seconds, (c) at 15 seconds.

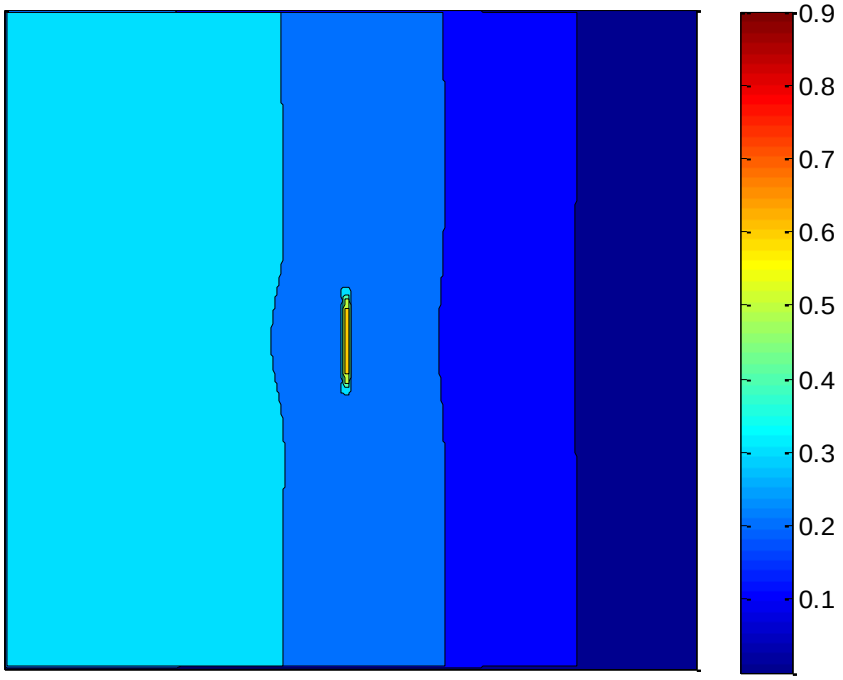

(d)

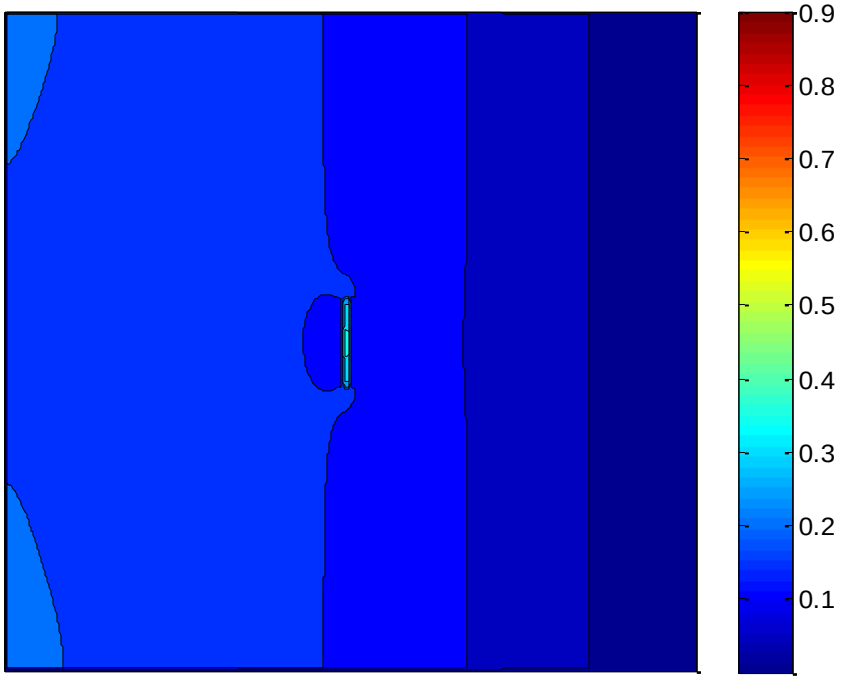

(e)

Fig. C.1 Images of Temperature Gradient for a 2-cm Longitudinal Crack (cont.), (d) at 30 seconds, (e) at 60 seconds.

0.5 cm crack

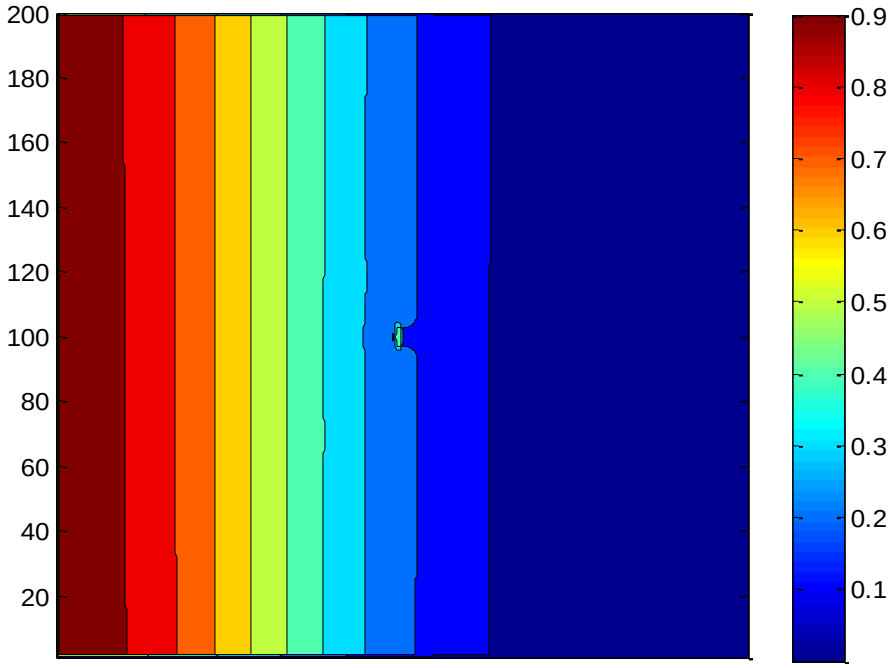

(a)

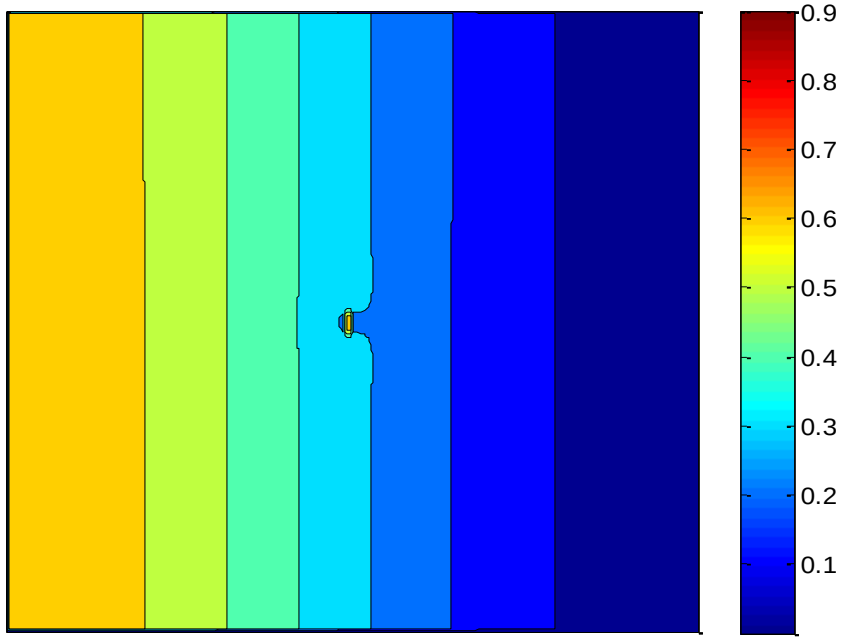

(b)

Fig. C.2 Images of Temperature Gradient for a 0.5-cm Longitudinal Crack, (a) at 5 seconds, (b) at 10 seconds.

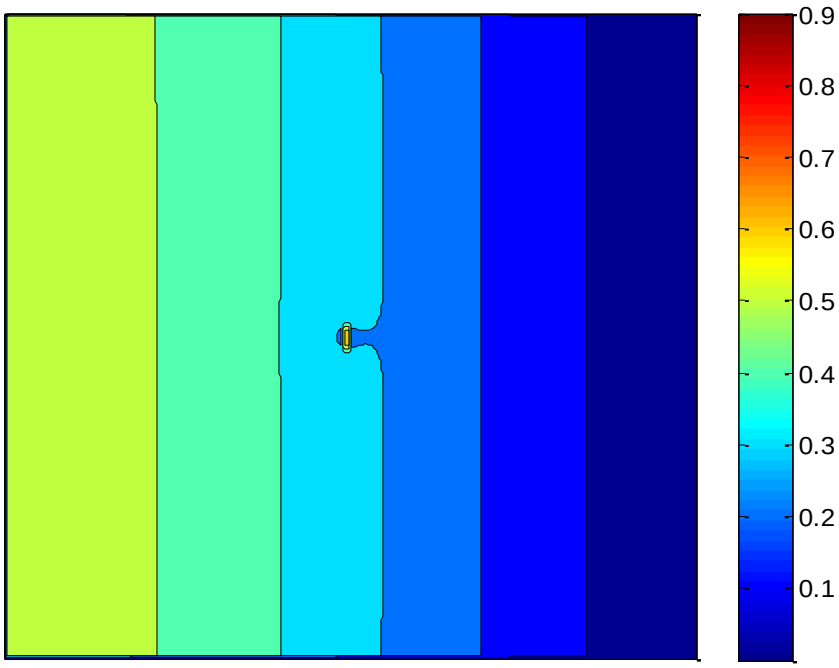

(c)

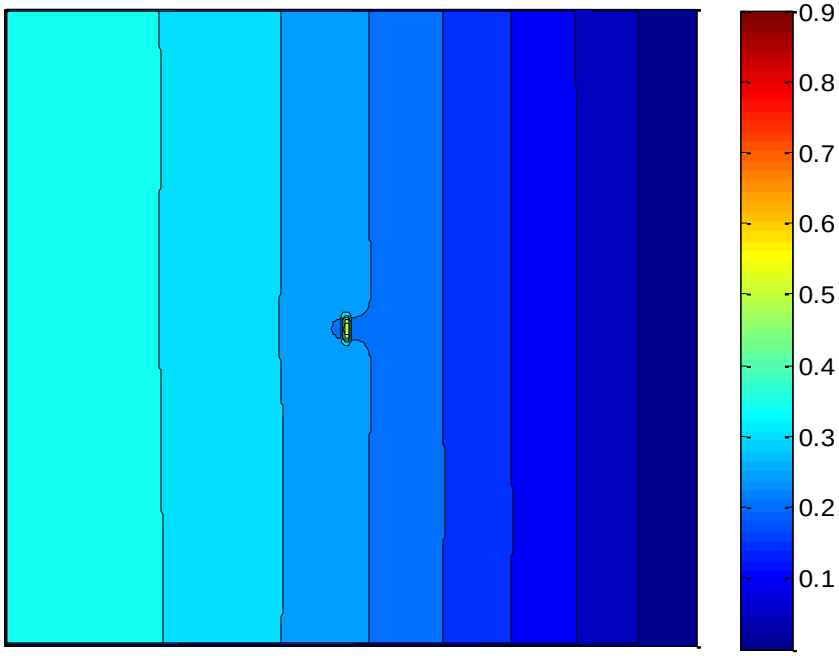

(d)

Fig. C.2 Images of Temperature Gradient for a 0.5-cm Longitudinal Crack (cont.), (c) at 15 seconds, (b) at 30 seconds.

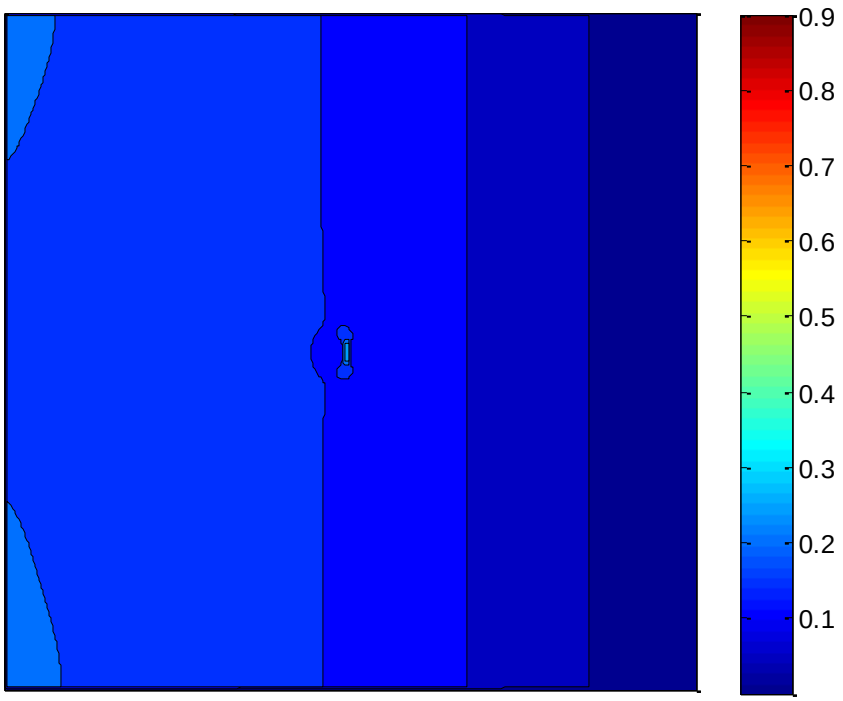

(e)

Fig. C.2 Images of Temperature Gradient for a 0.5-cm Longitudinal Crack (cont.), (e) at 60 seconds.

C.2 Angled Crack

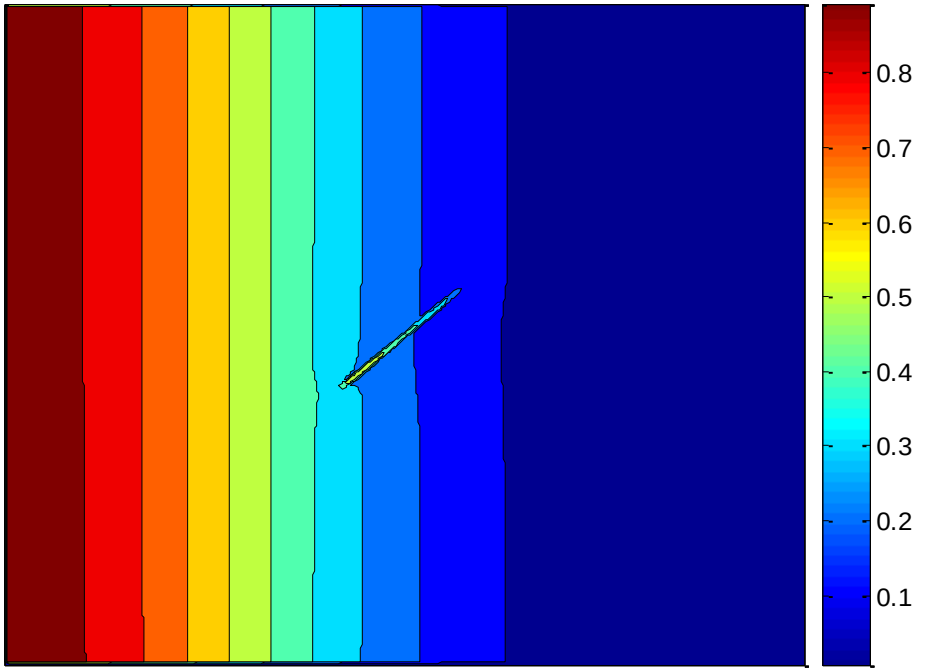

(a)

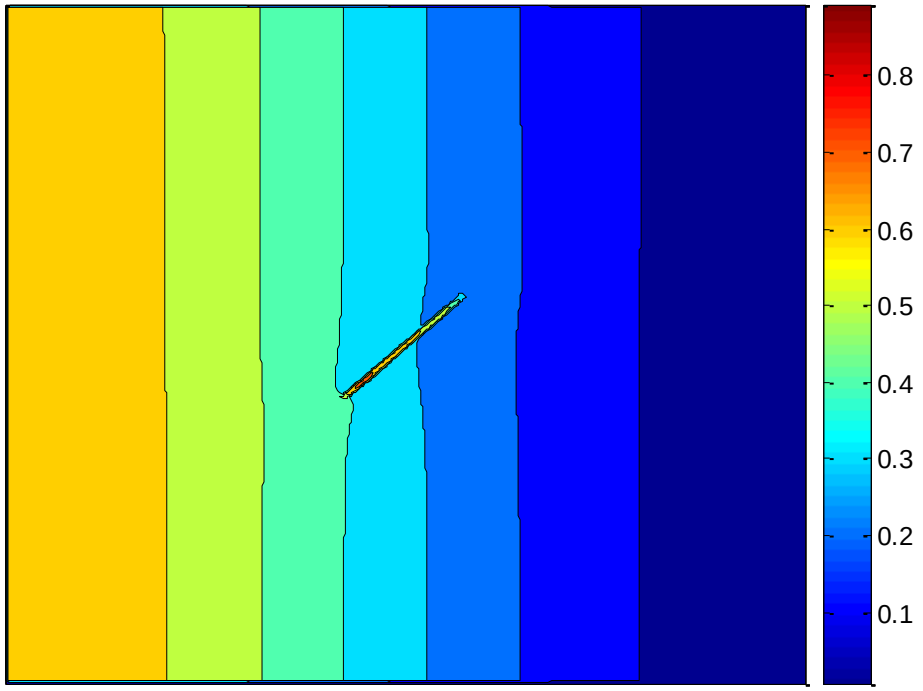

(b)

Fig. C.3 Images of Temperature Gradient for a 3-cm Angled Crack, (a) at 5 seconds, (b) at 10 seconds.

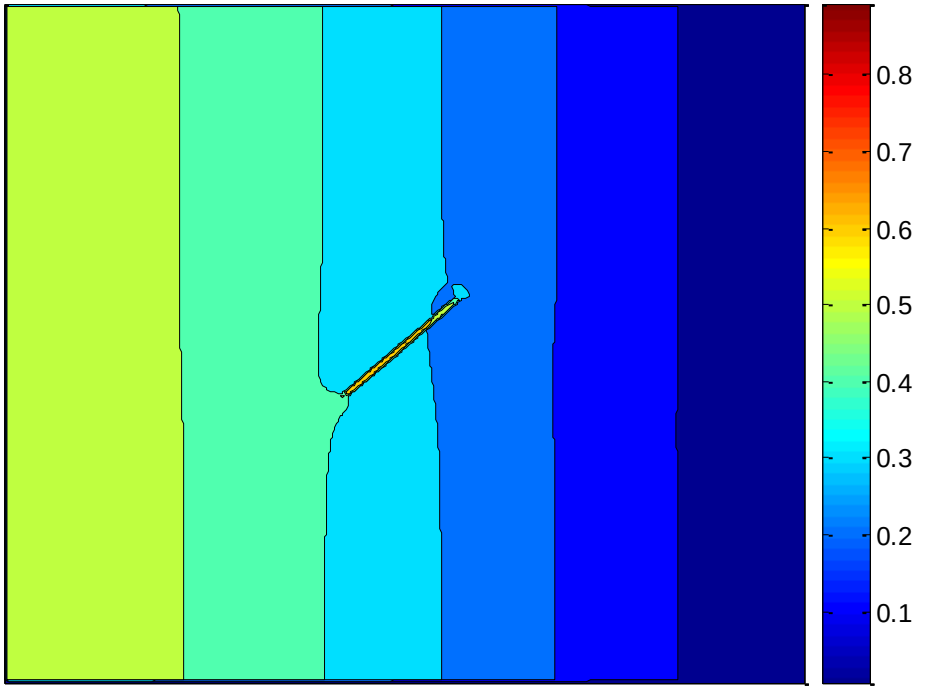

(c)

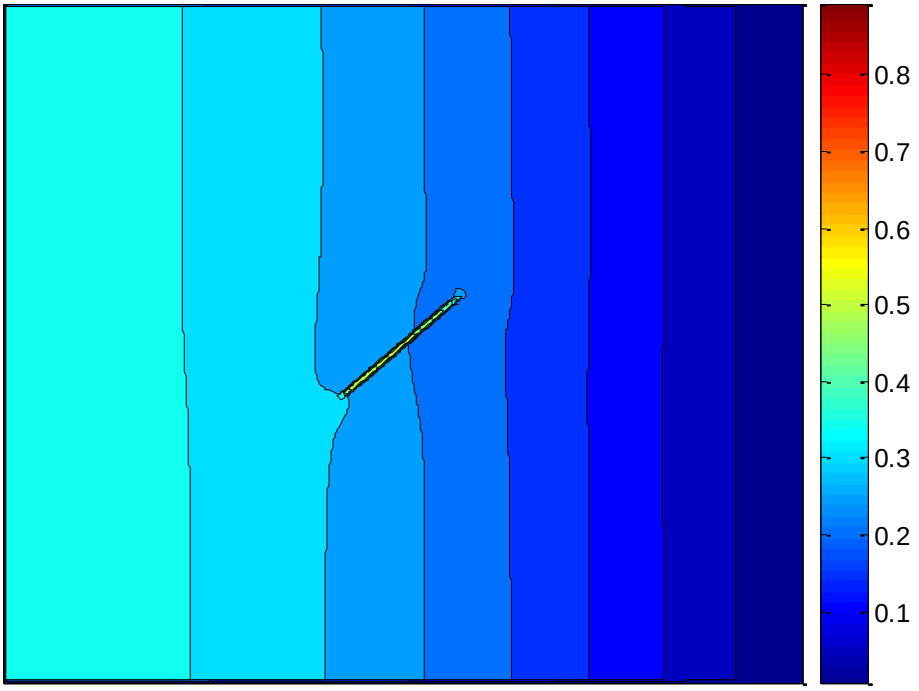

(d)

Fig. C.3 Images of Temperature Gradient for a 3-cm Angled Crack (cont.), (c) at 15 seconds, (d) at 30 seconds.

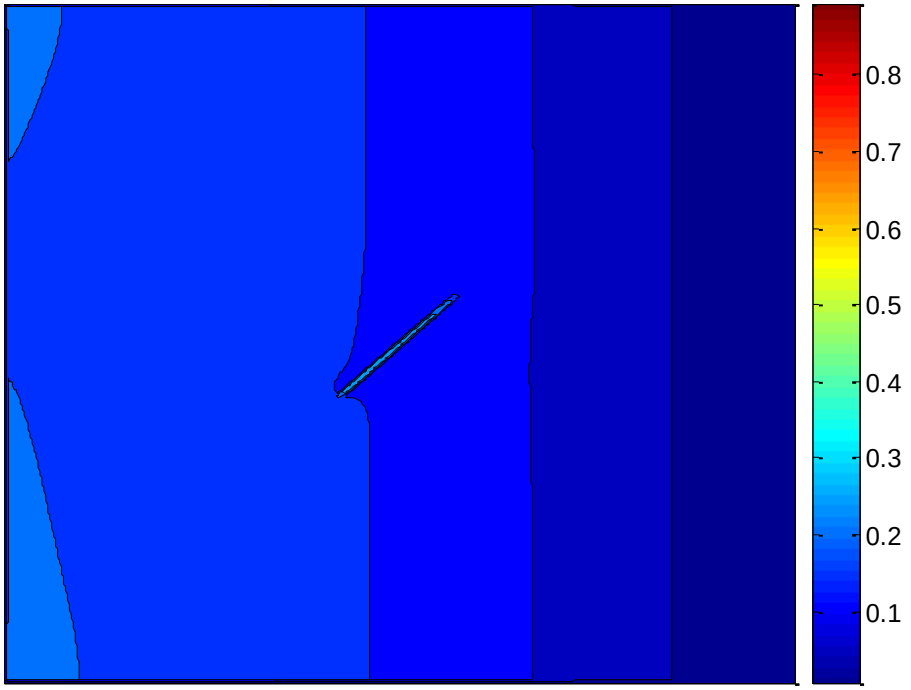

(e)

Fig. C.3 Images of Temperature Gradient for a 3-cm Angled Crack (cont.), (a) at 60 seconds.

C.3 Reduced Conductivity

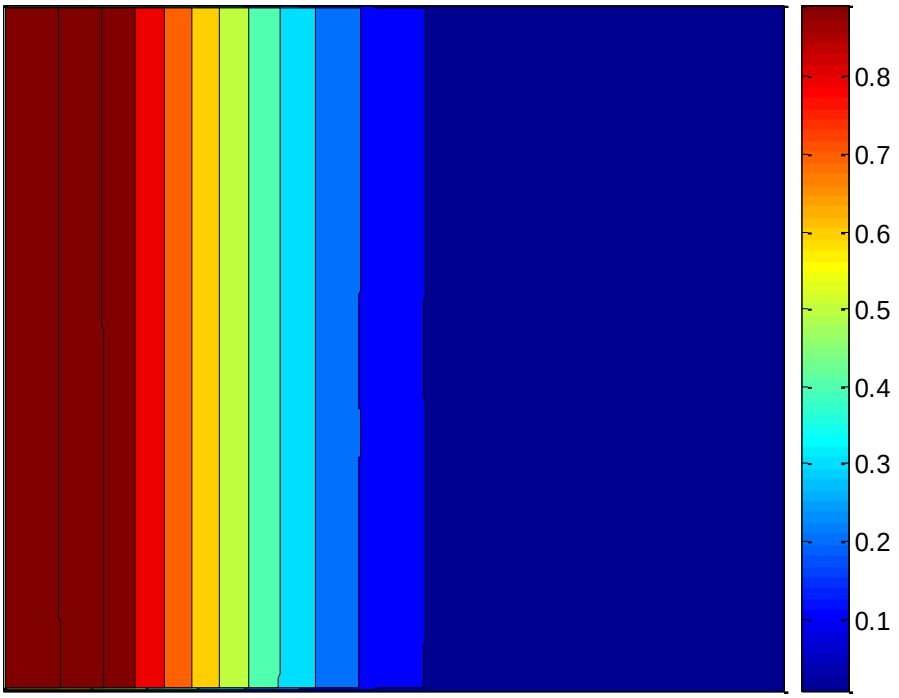

(a)

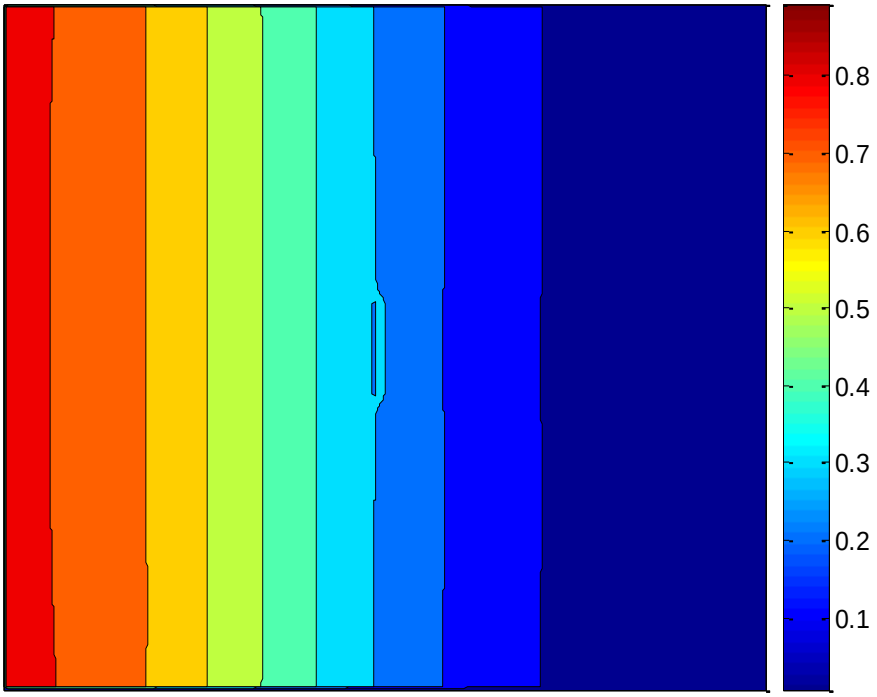

(b)

Fig. C.4 Images of Temperature Gradient for a 2-cm Crack with Lower Conductivity, (a) at 30 seconds, (b) at 60 seconds.

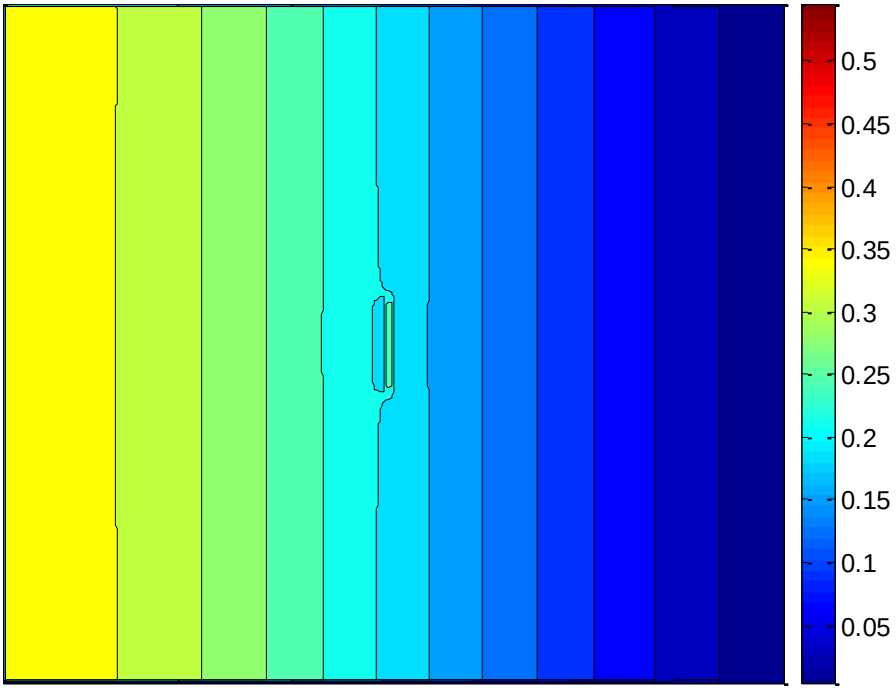

(c)

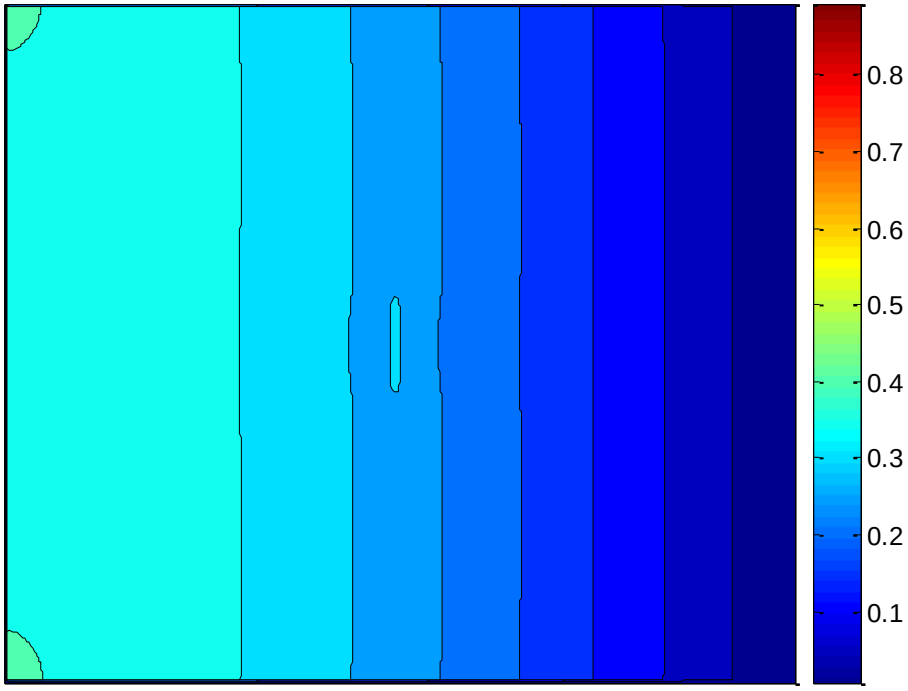

(d)

Fig. C.4 Images of Temperature Gradient for a 2-cm Crack with Lower Conductivity (cont.), (c) at 120 seconds, (d) at 240 seconds.

C.4 Voids

3 cm void

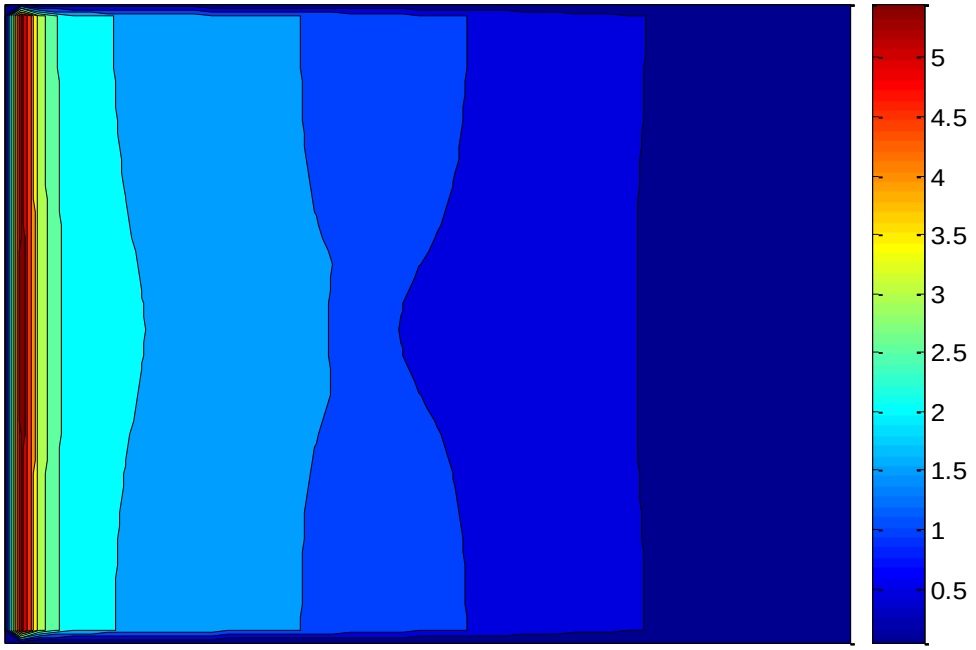

(a)

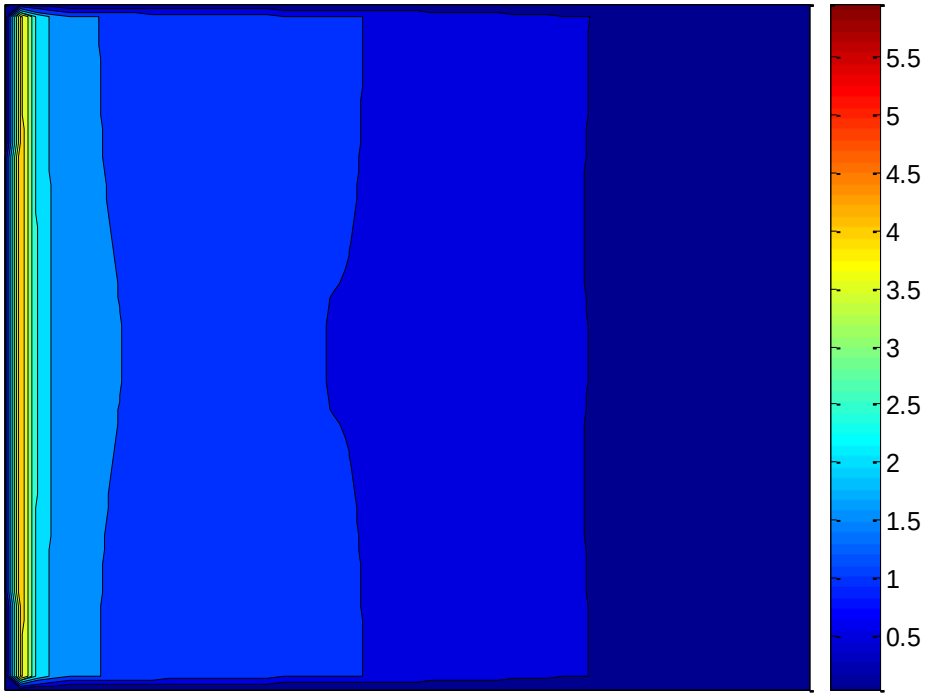

(b)

Fig. C.5 Image of Surface Temperature Gradient for a 3-cm Center Void, (a) at 30 seconds, (b) at 60 seconds.

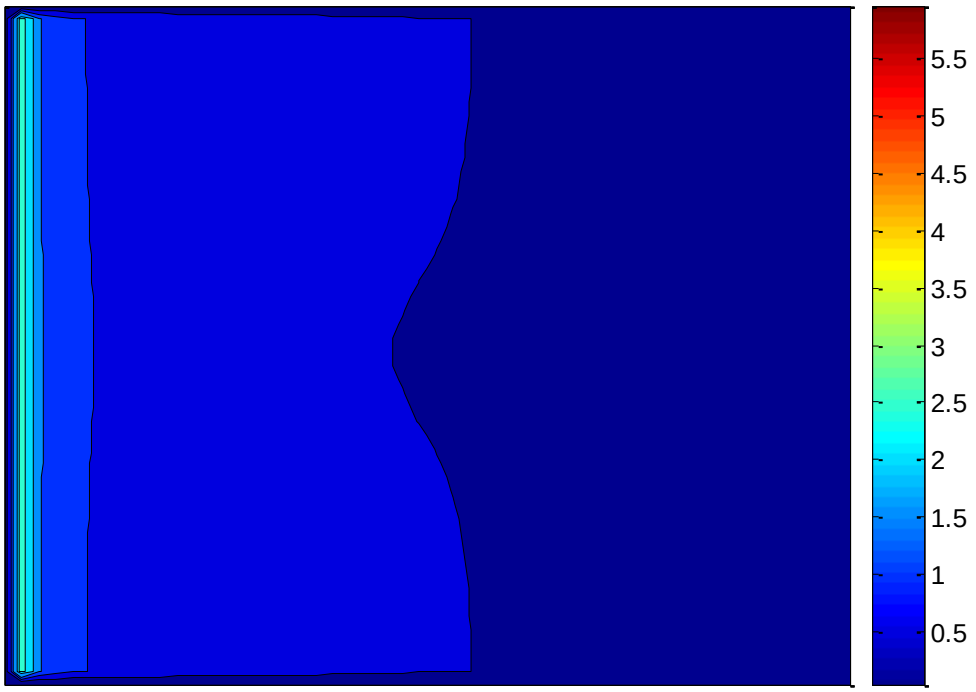

(c)

Fig. C.5 Image of Surface Temperature Gradient for a 3-cm Center Void (cont.), (c) at 120 seconds.

5 cm void

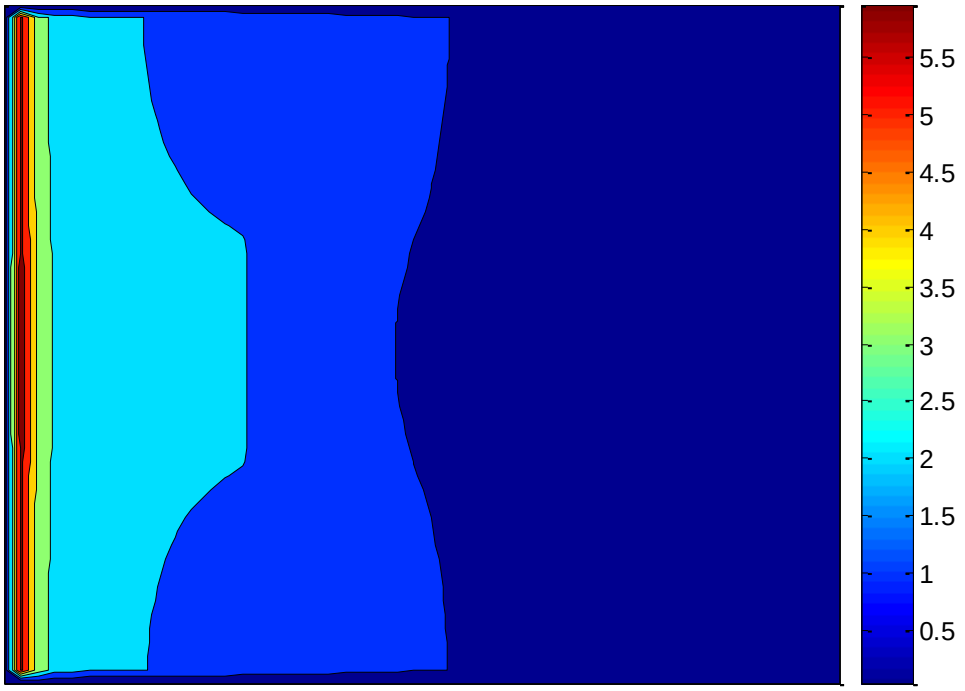

(a)

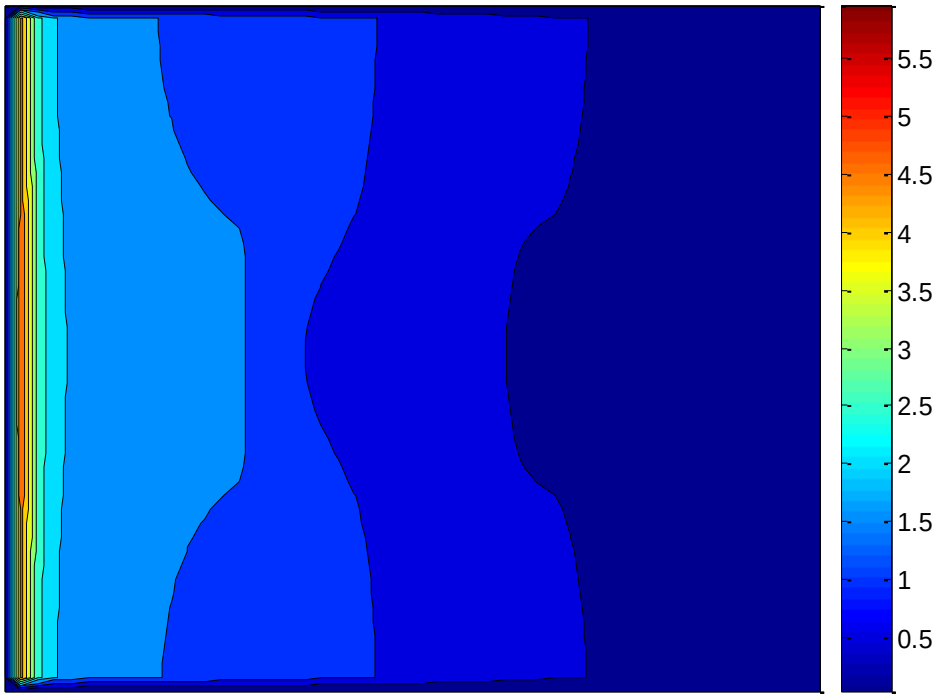

(b)

Fig. C.6 Image of Surface Temperature Gradient for a 5-cm Center Void, (a) at 30 seconds, (b) at 60 seconds.